

**Comparison of numerical
methods for modelling ocean
circulation in basins with
irregular coasts**

by

Frédéric DUPONT

Department of Atmospheric and Oceanic
Sciences
McGill University
Montreal

A thesis submitted to the
Faculty of Graduate Studies and
Research
in partial fulfillment of the requirements
for the degree of
Doctorate in Philosophy

© Frédéric DUPONT, Juin 2001

ABSTRACT

Comprehension of global oceanic currents and, ultimately, of climate variability requires the use of computer modelling. Although much effort has been spent on the accuracy of traditional finite difference (FD) models used in ocean modelling, there are still concerns, especially since these models have a crude representation of the geometry of oceanic basins. Such a crude representation may influence the accuracy of modelling boundary currents, or unrealistically represent the impinging of eddies or the propagation of Kelvin waves along the coastline. This motivated the use of alternative modelling techniques applied on completely irregular geometries such as finite element (FE) and spectral element (SE) methods. In this thesis, we want to investigate the accuracy and cost-effectiveness of these three numerical methods in irregular domains and to understand to which extent the unstructured grid FE and SE methods constitute an improvement over the more traditional FD methods. To accomplish this, we limit ourselves to modelling the shallow water equations in presence of irregular coastlines with no bottom topography.

In the first part of the thesis, we compare the performances of FD methods on Cartesian grids with FE and SE methods in various geometries for linear and nonlinear applications. We argue that the SE method is to a certain extent superior to FD methods. In a second part, we study the influence of step-like walls on vorticity budgets for wind-driven shallow water FD models. We show that vorticity budgets can be very sensitive to the FD formulation. This has certain implications for using vorticity budgets as a diagnostic tool in FD models. In the final part, we use a SE shallow water model for investigating the “inertial runaway problem” in irregular domains for the single-gyre Munk problem. Ideally, one would like the statistical equilibrium observed at large Reynolds number to be insensitive to model choices that are not well founded, e.g., the precise value of the viscous coefficient, and choice of dynamic boundary condition. Simple models of geophysical flows are indeed very sensitive to these choices. For example, flows typically converge to unrealistically strong circulations, particularly under free-slip boundary conditions, even at rather modest Reynolds

numbers. This is referred to as the “inertial runaway problem”. We show that the addition of irregular coastlines to the canonical problem helps to slow considerably the circulation, but does not prevent runaway.

RÉSUMÉ

La compréhension des courants océaniques globaux et, ultimement, de la variabilité climatique requiert l'usage de la modélisation numérique. Bien que beaucoup d'effort ait été dépensé dans l'amélioration des modèles traditionnels aux différences finies (DF) utilisés dans la modélisation océanique, il reste des interrogations concernant la précision de ces modèles, et ce d'autant plus que ces modèles ont une représentation très grossière de la géométrie des bassins océaniques. Une telle grossière représentation peut modifier la précision des courants le long des frontières, ou mal représenter le choc des tourbillons sur, ou la propagation des ondes de Kelvin le long de la frontière. Ceci a motivé l'utilisation des méthodes numériques alternatives comme les éléments finis (EF) ou les éléments spectraux (ES) qui s'appliquent à des géométries complètement irrégulières. Dans cette thèse, nous voulons étudier la précision et le coût de ces trois types de méthodes numériques dans des domaines irréguliers et comprendre jusqu'à quel point les méthodes EF et ES fonctionnant sur des grilles irrégulières constituent un progrès comparé aux méthodes DF traditionnelles. Dans ce but, nous nous limitons à modéliser les équations en eaux peu profondes en présence des côtes irrégulières sans topographie.

Dans la première partie de cette thèse, nous comparons les performances des méthodes DF sur des grilles cartésiennes avec les méthodes EF et ES dans des géométries différentes pour des problèmes linéaires et non-linéaires. Nous argumentons que la méthode ES est, dans une certaine mesure, supérieure aux méthodes DF. Dans la seconde partie, nous étudions l'influence des marches d'escalier présentes le long des murs sur les budgets de vorticité pour des modèles DF en eaux peu profondes forcés par le vent. Nous montrons que les budgets de vorticité peuvent être très sensibles à la formulation DF utilisée. Ceci a certaines implications concernant l'utilisation des budgets de vorticité comme outil de diagnostic dans les modèles DF. Dans la dernière partie, nous utilisons un modèle ES en eaux peu profondes pour étudier le problème de "fuite inertielle" dans des domaines irréguliers pour le problème de Munk non-linéaire. Idéalement, on voudrait

que l'équilibre statistique observé à grand nombre de Reynolds soit insensible au choix fait concernant des approximations mal—ou peu—fondées du modèle, comme la valeur du coefficient de viscosité turbulente ou le type de condition frontière. Les modèles simples de fluides géophysiques ont en effet tendance à être très sensibles. Par exemple, l'écoulement converge vers des circulations totalement irréalistes, particulièrement pour une condition frontière de glissement libre, et ce même pour des nombres raisonnables de Reynolds. C'est ce que l'on nomme "fuite inertielle". Nous montrons que l'inclusion de côtes irrégulières dans ce problème canonique permet de ralentir considérablement la circulation, mais n'élimine pas pour autant le problème de la fuite inertielle.

CONTRIBUTIONS

In Chapter 2, we develop our own adaptive spectral element method which is an automatic procedure for assessing local errors and increasing, accordingly, the resolution of the mesh. Test and use of this procedure are made in Chapters 3 and 5. We also develop our own curved spectral element method for better representing smoothly varying coastlines.

In Chapter 3, we develop a series of test cases in order to study the convergence with resolution of the accuracy and cost-effectiveness of each scheme in regular and irregular domains. The originality of this approach stems from the variety of numerical methods we test and compare, and the thorough study of the influence of the resolution on them. We explore the limitations of each numerical scheme.

In Chapter 4, we use vorticity budgets as a way to assess the accuracy of different numerical formulations for modelling wind driven ocean gyres in a rectangular basin. In particular, we demonstrate that, for finite difference formulations, the advective terms in the vorticity budget do not integrate to zero. This error can be exacerbated by the presence of near step-like structures along the boundary, such as those that occur when a straight coastline lies at an angle to the coordinate axes used for discretization. It is further found that this problem is minimized for certain numerical choices relating to the treatment of the advective and viscous terms.

In Chapter 5, we use a spectral element model to investigate the inertial runaway problem (i.e., that models produce unrealistically strong flows as dissipative parameters are reduced towards what are considered realistic values) in irregular domains. In particular, we show that small scale (but resolved) features in the coastlines lead to the generation of fine scale structure in the vorticity field, where the Rossby number can become of order unity, and the quasi-geostrophic approximation becomes suspect. That these occur under free-slip boundary condition contrasts the classic, rectangular basin case. We find that small scale structures in the coastline act to slow, but not to stop inertial runaway.

Contents

Abstract	i
Résumé	iii
Contributions	iv
List of Figures	viii
List of Tables	xiii
Acknowledgements	xiv
1 Introduction	1
2 Presentation of the Numerical Methods	6
2.1 The Time Discretization	8
2.2 Finite Difference Models	10
2.2.1 Introduction	10
2.2.2 The Three Staggingings Used	12
2.3 Finite Element Models	15
2.3.1 Introduction	15
2.3.2 The Galerkin Formulation	17

2.3.3	The Different Finite Element Models Tested	18
2.4	The Discontinuous Spectral Element Method	21
2.4.1	Introduction	21
2.4.2	The Model Formulation	22
2.4.3	Adaptive Mesh Refinement	24
2.4.4	Curved Spectral Element Method	25
2.5	Summary	27
3	Testing the Different Numerical Methods	28
3.1	Gravity Waves in a Square Domain	28
3.2	The Wind-driven Circulation in a Circular Domain	32
3.3	Conservative Properties of the Different Numerical Formulations for a Non-linear Problem	36
3.4	The Munk Problem in a Square Domain	37
3.5	Conclusions	43
4	Finite Difference Methods in Rotated Basins	47
4.1	Introduction	47
4.2	Vorticity Budgets in a C-grid SW Model	48
4.2.1	The General Form of the Discretized Vorticity Budget	48
4.2.2	Numerical Formulations	50
4.2.3	Results	51
4.3	Vorticity Budgets in SW B-grid Models	53
4.4	The Quasi-Geostrophic Model	55
4.4.1	Discretization	55
4.4.2	Results	56

4.5	Discussion and Conclusion	57
5	Single Gyre Circulation in Irregular Domains	64
5.1	Review of the Single Gyre Problem with Free-Slip Boundary Conditions . .	64
5.2	Model Selection and Experimental Design	67
5.3	Results	72
5.3.1	General Results for all Geometries	72
5.3.2	Role of the Transients for Geometry V at High Reynolds Number . .	74
5.4	Scale Analysis and Discussion	81
5.5	Adaptivity	85
5.6	Conclusions	87
6	Conclusions	90
A	An A-grid Energy Conserving Formulation	94
B	Model Vorticity Budget on a B-grid	96

List of Figures

2.2	Effect of a poor resolution on the geometry of a strait.	11
2.1	Effect of the rotation on the discretization of a square domain.	12
2.3	Elevation field for the Kelvin retardation problem in presence of steps along the walls at two different resolutions.	13
2.4	The three major horizontal staggerings for the primitive equations.	14
2.5	Triangulation of the domain.	17
2.6	ϕ_i , the basis function related to the node M_i	17
2.7	ϕ_2 is the basis function related to the node $x_2 = 0$	18
2.8	The discontinuous linear non conforming basis function for the $P_1^{NC} - P_1$ element of Hua and Thomasset (Hua and Thomasset, 1984).	20
2.9	The discontinuous constant basis function for pressure over the macro-element of LLS.	21
2.10	Local non-orthogonal coordinates in a given triangle	23
2.11	Example of Legendre polynomials $\Phi_i = L_2(\xi_1)L_3(\xi_2)$	23
2.12	Remeshing strategies. The triangle to be refined is in grey.	25
2.13	Transformation of one triangle into a curved triangle	26
2.14	Transformation of one triangle into a curved triangle with the coordinate system used in the computation of the integrals	26
3.1	The wave test experiment	29
3.2	Convergence with resolution of the normalized error in the u -component for second order C-grid formulation (FDM), O-FDM4 and R-FDM4 models. . .	30

3.3	CPU cost with the normalized error in u -component for the second order C-grid (FDM) and R-FDM4 models.	30
3.4	The four FE models (LW, HT, PZM, LLS) are tested against the analytical solution with increasing resolution.	31
3.5	Convergence of the normalized error in v with respect to the resolution for the LW-FE and SE models	32
3.6	Convergence of the normalized error in u with respect to the resolution for the C-grid FD, LW-FE and SE models.	32
3.7	Variation in the u -component normalized error as a function of CPU cost for five models.	33
3.8	Grids for the circular domain for the FD models.	34
3.9	Convergence with resolution of the normalized elevation error for the second order C-grid FD, O-FDM4 and R-FDM4 models in a circular domain. . . .	35
3.10	Elevation error in a circular domain for four FE models.	35
3.11	Normalized elevation error for the C-grid FD, LW-FE and SE models for a circular domain.	36
3.12	Total energy after 18 days of simulation for the C-grid FD and the lumped LW, delumped LW, PZM and LLS FE models and the SE model for the geostrophically balanced eddy.	37
3.15	Kinetic energy during a 6 year spin-up for the C-grid FD, the lumped LW, HT, PZM and LLS FE models.	38
3.13	Elevation field after a six year simulation in a non-rotated basin using O-FDM4 and R-FDM4.	39
3.14	As for Figure 3.13 but for rotated basin.	39
3.16	Elevation field after a 6 year spin-up for the C-grid FD, the lumped LW, delumped LW, HT, PZM and LLS FE models for the single gyre wind forcing problem.	40
3.17	Single gyre wind forcing experiments for the delumped LW FE model compared to the C-grid FD model.	41
3.18	Kinetic energy during spin-up for the single gyre Munk problem with $\nu = 2000 \text{ m}^2\text{s}^{-1}$ for the C-grid FD, the delumped LW FE and SE models. . . .	41
3.19	Elevation field for the SE model after 6 years from spin-up for the single gyre Munk problem with $\nu = 2000 \text{ m}^2\text{s}^{-1}$, $n_c = 5$	41

3.20	As for Fig. 3.18 but with $\nu = 700 \text{ m}^2\text{s}^{-1}$	42
3.21	As for Fig. 3.19 but with $\nu = 700 \text{ m}^2\text{s}^{-1}$	42
3.22	Convergence with resolution for the nonlinear Munk problem of the normalized kinetic energy error for the solution from the C-grid FD and the SE models.	43
3.23	As for Fig. 3.22 but for the convergence of the normalized error with CPU cost.	43
3.24	Solutions after a 6 year spin-up for the Munk problem using the adaptive SE model with $n_c = 5$	44
4.1	Locations of variables near a step for the SW C-grid model and the QG model.	59
4.2	Local advective flux along the boundary at 20 km resolution in a square basin for the enstrophy conserving formulation.	59
4.3	Northward flow past a forward step. The shaded area is the model domain.	59
4.4	Elevation fields in meters after a 6 year spin-up for 20 km and 10 km resolution. Shown are results from the A and B combination with or without a 3.44° rotation angle of the basin.	60
4.5	(a) Kinetic energy after spin-up and (b) ratio of \mathcal{F}_{adv} to \mathcal{F}_i for the four combinations.	60
4.6	Kinetic energy after spin-up for the B combination in $10^{10} \text{ m}^5/\text{s}^2$	61
4.7	Ratio of \mathcal{F}_{adv} to \mathcal{F}_i for the B combination.	61
4.8	Convergence of \mathcal{F}_{adv} with resolution for 0° , 20° , 45° rotation angle for the B combination.	61
4.9	Kinetic energy during spin-up for six runs using the J_1 Jacobian at 6 different rotation angles.	61
4.10	Kinetic energy after spin-up for (a) J_3 at 0° rotation, (b) J_7 at 0° , (c) J_3 at 30° , (d) J_7 at 30° , (e) J_3 at -30° , (f) J_7 at -30°	62
4.11	Ratio of \mathcal{F}'_{adv} to the wind input for (a) J_3 at 0° rotation, (b) J_7 at 0° , (c) J_3 at 30° , (d) J_7 at 30°	62
4.12	Ratio of \mathcal{F}_c to the wind input. (a-d) as described in Fig. 4.10.	62
4.13	Ratio of $\mathcal{F}_{adv} = \mathcal{F}'_{adv} + \mathcal{F}_c$ to the wind input. (a-d) as described in Fig. 4.10.	62

4.14	Semi-advective flux, \mathcal{F}'_{adv} , and beta contribution, \mathcal{F}_c , to the vorticity budget for the J_3 Jacobian at -30° rotation angle.	63
5.1	Notation corresponding to the curvilinear coordinates.	66
5.2	The five geometries used for our application of the SE method.	68
5.3	Elevation fields in the Geometry V for the C-grid model after 3 years of spin-up.	69
5.4	Total energy during spin-up for the A and B combinations of the FD C-grid model and for the SE model at $n_c = 5$ (SPOC 5) in Geometry V. $\nu = 100 \text{ m}^2\text{s}^{-1}$	69
5.5	Mean elevation fields for the five geometries using the SE model.	70
5.6	Mean vorticity field for the Geometries IV and V using the SE model.	73
5.7	Power input by the wind using the mean fields with respect to the boundary Reynolds number.	74
5.8	Mean standard deviation of the elevation.	75
5.9	Mean standard deviation of the elevation for frequencies with period above 200 days.	75
5.10	Mean standard deviation of the elevation for frequencies with period between 17 and 200 days.	75
5.11	Mean standard deviation of the elevation for frequencies with period between .6 and 17 days.	75
5.16	Instantaneous vorticity field in the vicinity of the recirculation.	78
5.12	Hovmöller diagram of the filtered elevation with respect to time and location along the boundary.	79
5.13	Amplitude of the Kelvin wave in meters along the boundary averaged over 6 years.	79
5.14	Time series of the amplitude of the oscillations at (x=500 km, y=0 km).	79
5.15	Total energy for the last 6 years of simulation.	80
5.17	(a) Local wind input to the vorticity in Geometry V. (b) Local divergence of the eddy transport of vorticity in Geometry V. (c) Vector plot of the eddy transport of vorticity normal to the streamlines in Geometry V.	81
5.18	The region in grey represents where the absolute vorticity is approximately conserved.	82

5.19	Maximum of the mean elevation for the three geometries. The maximum elevation is a good proxy for the strength of the recirculation.	84
5.20	Kinetic energy of the mean fields with respect to the boundary Reynolds number.	85
5.21	Mesh for the original and the refined runs.	86
5.22	Total energy for the last 6 years of simulation for the original and refined meshes.	87
5.23	Amplitude of the fast oscillations at (x=500 km, y=0 km) along the boundary for the original and refined meshes.	88
5.24	Mean elevation fields for the original mesh and the refined mesh.	88
5.25	Mean vorticity fields for the original mesh and the refined mesh.	88

List of Tables

2.1	List of variables in (2.1–2.2)	7
2.2	Refinements parameters used in the simulations unless otherwise specified. .	25
3.1	Convergence order for the different models for the linear wave experiment in a square domain. For all models, the order is fairly close to their theoretical value. Models using unstructured grids lost almost an order for the error in v compared to the error in u	33
3.2	Convergence order in elevation, for the different models for the linear wind-driven experiment in a circular domain without Coriolis terms.	36
3.3	Convergence order for the different models for the nonlinear Munk problem in a square domain.	43
4.1	The four combinations of advection formulations and stress tensor formulations.	52
4.2	Summary of the vorticity budget and kinetic energy diagnostics for the B-grid after a spin-up of 6 years.	54
A.1	Notations for the finite volume method	94

ACKNOWLEDGEMENTS

Many thanks go to my supervisors, Charles Lin and David Straub, for their support and the proof-reading of the thesis. David Straub is in particular acknowledged for his important contribution to Chapters 4 and 5.

The C2GRC group at McGill was a great place for meeting and listening to world-renowned scientists. I must thank in particular Lawrence Mysak for inviting me along on numerous occasions for after-seminar beers or suppers. Many McGill PhD students left the department in the course of my studies and I am indebted to them for engrossing scientific conversations we had around a few beers. Thanks therefore go to Rob Scott, Halldor Bjornsson, Martin Charon, Daniel Le Roux, Bruno Tremblay, Daniel Bourgault, Stephen Newbigging and three cornerstones of the department, Rick Danielson, Werner Wintels and Marco Carrera.

Deep thanks go to Catherine Mavriplis for discussion about error-estimators in adaptive spectral element methods and Julien Dompierre for the remeshing strategies. Stephen Newbigging, Ted Tedford, Drew Peterson and Jason Chaffey corrected the spelling and the English grammar. CERCA (Centre de recherche en calcul appliqué) provided me with an excellent working environment. Many thanks go to the CERCA staff, scientists and other PhD students in general for their support and discussions.

I must also thank my father for motivating me to do a PhD in North-America despite the great distance and stretched family bounds implied by doing so.

This research was supported by NSERC and CCGCR. VU (developed at CERCA) GMT, Gnuplot and Ferret are the graphical packages used in this thesis.

Chapter 1

Introduction

Modelling the ocean has become an essential component of coastal and navigational hazard prevention (beach erosion, pollutant transport, tidal or storm surge, ice drift, wave height). Moreover, the ocean being a large component of the global climate, to model its circulation is essential to obtaining a better understanding of the dramatic climatic changes which either have occurred or might occur. Finally, some theoretical studies require the use of models in order to understand fundamental physical processes which involve nonlinear dynamics and/or complex geometries, and which are beyond analytical approaches.

The first attempts to model the ocean circulation were made in the middle of the 20th century, after the work of Ekman (1905) who recognized the importance of the wind as the major source of mechanical forcing. Sverdrup (1947) derived a simple law that relates the ocean currents to the curl of the wind friction. Stommel (1948) and Munk (1950) derived analytical models of the wind induced ocean circulation in closed rectangular basins using simplified dissipative laws. Both the Stommel and Munk models afford simple explanation of the westward intensification of oceanic currents, such as observed for the Gulf Stream or the Kuroshio. An important threshold in computer performances was reached in the late sixties, and this allowed for the first full prognostic three-dimensional studies of the ocean circulation (Bryan and Cox, 1967; Bryan, 1969). These models were driven by mechanical forcing (the winds and a bottom drag) and by fluxes of salt and heat exchanged with the atmosphere. They could take into account the complexity of the geometry and the nonlinear nature of the oceanic currents. Ideally, these models should be able to fill the gaps in the data

and give reasonable estimates of the ocean circulation. However, because of their inherent complexity, the poor knowledge of numerous physical processes and problems with the definition of coastlines, straits and sea-mounts, they drift easily from any reasonable state if no restoring terms are added to the equations for temperature and salinity. Thus, prognostic three-dimensional models may sometimes look like expensive interpolators and yield no very different results than simpler inverse models do. Nonetheless, they have produced useful estimates of the role of the oceans in the thermal global budget and the importance of the so-called conveyor belt.

Our main concern is the representation of irregular domains in numerical ocean models, and their influence on the dynamics of the currents. Models, so far, have only crudely represented these irregular boundaries, either in the vertical (the topography) or in the horizontal (the coastlines). Our objective in this thesis is to evaluate the accuracy of conventional numerical methods in the presence of irregular coastlines and to introduce more accurate alternatives.

Furthermore, we suspect that irregular coastlines have important but sometimes under-estimated influences of the dynamics of the currents flowing along them. The energetics of these currents are controlled by the transfer of energy to smaller scales by nonlinear interactions. These interactions are likely to take place along the western part of the oceanic basins where the currents are the strongest. In particular, as the geostrophic balance (the main assumption governing the dynamics of the currents) in these regions breaks down, we hint at possible interactions between the geostrophic

and ageostrophic modes. We therefore focus on models which are simple enough to represent geostrophic-ageostrophic interactions on a large range of scales. A shallow water model seems appropriate for these goals. The dynamics are only two dimensional which allows for very high resolutions in the horizontal directions, as opposed to more complex three-dimensional models where the same level of resolution would be too expensive. In one particular context, we introduce a quasi-geostrophic (QG) model for comparison. This particular type of model represents only the geostrophic motions. Previous studies focusing on nonlinear interactions were usually done in very idealized and regular domains using QG models. Hence, we hope to make an interesting contribution by conducting relatively simple experiments involving idealized but still irregular coastlines and somewhat more complex dynamics compared to QG models.

The problem of accurately representing the geometry of the domain in ocean models is divided in two sub-problems: representing the bottom boundary (the topography) and representing the lateral boundaries (the coastline). Topographical features (sills or sea-mounts) are essential to the mixing of waters of different properties, origins and depths, and, therefore, their influence extends to the largest scales. Coastlines partially enclose the oceanic basins. Their presence is essential to the comprehension of the oceanic currents (such as the westward intensification of currents). It was early realized that a crude vertical representation of the topography (z - or geopotential vertical coordinate) could be detrimental to an accurate modelling of the ocean circulation. In particular, waters of different properties tend to mix over sills with dramatic consequences for the global ocean circulation if the vertical discretization is too crude. To remedy this problem, vertical terrain following coordinates were proposed, despite various known limitations. However, the horizontal discretization has not received the same level of scrutiny. Most of the modern oceanic models still crudely represent coastlines. A crude horizontal discretization has several consequences. Straits may be under-resolved and the associated exchange of water modified: The strait of Gibraltar controls the Mediterranean salt input into the Atlantic; the Bering strait controls the fresh-

water input between the Arctic and the Pacific and the Indonesian archipelago is notorious for being the location of the so-called return flow of the vast thermo-haline conveyor belt which circles the globe. A crude horizontal representation has also retardation effects for fast oceanic modes (Kelvin waves) which propagate along coastlines (Schwab and Beletsky, 1998). For the wind-driven circulation, little is known about the influence of crude horizontal representations.

In order to study the influence of the choice of the numerical method, we propose to test several of them, and investigate which one best handles irregular coastlines. We therefore propose to test different staggarings of the finite difference (FD) method and several finite element (FE) formulations against a spectral element method. The test-cases we choose are very idealized in order to focus only on the dynamical aspects of two-dimensional flows (no physical parameterizations except for constant dissipative coefficients) and range from simple linear and non-linear test-cases in square domains, to linear and non-linear test-cases in smoothly irregular domains. The finite difference models range from the conventional Arakawa C-grid (preferentially used for regional studies — e.g. Bleck and Boundra, 1981; Blumderg and Mellor, 1983), to the conventional Arakawa B-grid (preferentially used for global studies as in Bryan-Cox derived models — e.g. Bryan, 1969; Cox, 1984), to the unconventional A-grid (Dietrich et al., 1993).

We choose to use the FE method because it has the decisive characteristic of representing boundaries more efficiently than the more conventional FD method and because it presents variable resolution capabilities. Oceanographers, especially the tidal community use FE models to represent tidal interactions and resonances which occur at different scales, from ocean basin to coastal inlets (Connor and Wang, 1974; Lynch and Gray, 1979; Walters and Cheng, 1979). Some of the modern FE models are derived from the earlier models formulated by Lynch and Werner (1987) and Le Provost *et al.* (1994). Others used the QG approximation and proposed a finite element formulation of the vorticity equation for the general ocean circulation (Fix, 1975; Dumas *et al.*, 1982; Myers and Weaver, 1995); results were very encouraging. Unfortunately, no general circula-

tion model based on the primitive equations (explained below) has been proposed based on the FE method and we try to determine the reasons for this relative failure. On the other hand, the spectral element method (an extension of the finite element method) has been used with a relative success by Iskandarani et al. (1995). Their method is based on quadrangular elements; instead, we favor the use of triangular elements which offer increased geometrical flexibility. Specifically, we propose to test a spectral element model based on this discretization technique. The apparent advantage of the spectral element method lies in the accepted advantage of spectral methods (the accuracy and the fast convergence with increasing resolution for regular problems) and the flexibility of an irregular grid. However, as with the spectral method, there is always the possibility that Gibbs oscillations appear when the fields being approximated are too irregular or under-resolved (the classical example is the step-function). We try to solve this problem by use of an adaptive method which increases the resolution (the number of triangles) in regions where the largest errors in the solution are observed (to be defined later). Finally, since finite element methods are potentially more costly than conventional finite difference methods due to the need for more matrix inversions, the spectral element method may be a good alternative because its enhanced accuracy (compared to finite elements) is not severely offset by an excessive cost. In order to verify this statement, we give an accuracy-to-cost function for all models.

Modelling the ocean is very challenging due to the coexistence of many physical processes at various spatial and time scales, from the lowest scales (salt intrusion and viscous boundary layers of a few centimeters), to surface waves induced by wind or wave breakings, tides, geostrophic eddies, to the general ocean circulation. Since all these processes can interact with each other, it is virtually impossible to reproduce and isolate with a high degree of realism any of these processes. Most often, approximations and parameterizations are used to represent the small scale (or sub-grid) phenomena and limit the explicit motions of the model to the scales of interest. In this hierarchy of approximations, the barotropic QG model represents the leading largest scale and lowest frequency ap-

proximation. There is no vertical structure and no horizontal divergent motions such as gravity waves. Then, somewhat more complex is the shallow water model. The variables are the horizontal velocity, (u, v) and the elevation of the free-surface, η . It allows for divergent motions but still does not permit vertical structure. Layered models are extended versions of shallow water models and allow for crude vertical (baroclinic) variations. For more realistic vertical structures, the so-called primitive equations are used. They are based in the incompressible Navier-Stokes equations and use the Boussinesq and hydrostatic assumptions. Further improvement can be gained by using a non-hydrostatic model which can represent the small scale convection. However, the limitation imposed by computer performance fixes the length scales and the physical processes which can be explicitly resolved. Some features, such as synoptic eddies, are very difficult to resolve in global circulation models. These eddies are of the order of 10 to 100 km and are relatively small compared to the basin scale (10,000 km). Nonetheless, some authors (Holland and Lin, 1975; Treguier, 1992) stress the importance of representing explicitly the role of the eddies in the transfer of energy between the different scales and their positive influence on the (more realistic) mean fields. These processes can not be perfectly mimicked by the alternative strategy of using eddy-parameterizations and, therefore, this strategy is argued to be flawed (Lesieur, 1997). Moreover, these parameterizations use coefficients difficult to adjust to real observations when these coefficients are not simply “cosmetic”. Therefore, a good general ocean model should be eddy-resolving. However, since the required resolution for a general circulation model of the ocean is too high (10 km at mid-latitudes), models should have, at least, variable resolution capabilities, in the sense that they should have capabilities to follow and resolve isolated eddies or westward boundary currents, while the rest of the domain is discretized at a coarser resolution.

It may be important to represent other physical processes. The Topex-Poseidon satellite mission, for instance, renewed interest in the surface ocean large scale activity: tides, Kelvin and Rossby waves and synoptic eddies whose signature were measurable on the surface elevation field of the

ocean. Hence, a good general or regional ocean model should also have a moving free-surface which allows for fast barotropic gravity waves. This was also pointed out by studies of the vertical eddy-viscosity over the rough topography of the Atlantic ridge (Polzin *et al.*, 1997). The large values of the eddy-viscosity observed over the ridge, probably induced by external tides, imply that the general circulation must interact with the tides, i.e. the QG physics interacts with the large scale gravity waves (ageostrophic horizontally divergent dynamics). From a theoretical point of view, it seems also more and more necessary to include ageostrophic motions in numerical models, even in the extra-tropics. The difficulty comes from explaining the cascade of energy down to the molecular viscosity scale where the energy can be dissipated. Indeed, the two dimensional (and QG) dynamics tend to cascade the energy up to the Rhines arrest scale (50 to 200 km) in typical basins and not down. Therefore, there is no clear mechanism that cascades down and dissipates the energy in QG dynamics. This mechanism may come from the non-linear interactions between the geostrophic and ageostrophic modes. This may be visible from spectral analysis (Stammer, 1997) which show no particular cut-off frequencies or wave-numbers separating geostrophic and ageostrophic modes ¹.

The presence of irregular coastlines may also be important for the interactions of the geostrophic and ageostrophic modes. First, because it provides a forcing source at various wave numbers and, moreover, because the westward side of ocean basins is the location where the geostrophic approximation is most likely to break down, i.e., where the transfer of energy is most likely to occur. These preceding arguments imply that general circulation models should allow for the interactions between the geostrophic and ageostrophic motions. The simplest system that allows for such interactions is the shallow water equation system.

¹To be precise, the elevation slope (related to the velocity) peaks at a wave-number which ranges depending on latitude between the Rhines scale and the first baroclinic Rossby radius of deformation. It is yet unclear how to interpret these results in terms of separation of geostrophic and ageostrophic modes, as the Rossby radius lies at the observational limit of the instrument.

Also for physical reasons, even eddy-resolving models need an explicit parameterization of dissipation. Although very crude, this is usually done through an explicit eddy-viscosity (Laplacian operator) parameterization. Such a parameterization requires an arbitrary choice for the dynamical boundary condition at the walls (a problem which is exacerbated when higher order dissipations are employed). We consider herein only two boundary conditions. One is the free-slip boundary condition and corresponds to fluids being free to slip along lateral boundaries. There is some ambiguity as to the precise definition of free-slip. Pedlosky (1987, p. 183) takes the point of view that it corresponds to there being no viscous flux of tangential momentum across the boundary (i.e., $\nu[\partial v/\partial x + \partial u/\partial y] = 0$ at the wall). We take a less stringent definition by simply forcing the normal derivative of the tangential velocity to be zero (for instance, $\partial v/\partial x = 0$ on a meridionally oriented wall). The latter choice is the one generally found in the literature. On straight walls, the two definitions are equivalent, and correspond to vertical vorticity vanishing at the wall. On curved boundaries, either definition mentioned above results in non-zero relative vorticity ². This bears some dynamical consequences that we discuss below. The second boundary condition is the so-called no-slip boundary condition which corresponds to fluids that do not slip along walls (the tangential velocity is zero), and leads to strong shear along walls. This boundary condition is considered to be the “real” one because it is the one observed in laboratory experiments at microscales. However, at the resolution used in modern ocean models (1 to 100 km), it is not clear which, if either, boundary condition is appropriate. The present trend in ocean modelling is to go towards higher Reynolds number (smaller lateral viscosity) and higher resolution along with no-slip boundary conditions. But the level of resolution is still very far from sufficient to represent realistic viscous boundary layers, although inertial boundary layers are definitely becoming more realistic. On the other hand, authors experienced problems with the free-slip boundary condition. In an idealized square basin and barotropic ocean, it is observed that under single-gyre wind forcing and decreasing eddy-viscosity,

²Pedlosky’s definition can lead to larger values of the relative vorticity.

the oceanic currents tend to jump to unrealistically high values with no signs of transient eddies, whatever the resolution of the model is. Hence, the free-slip boundary condition prevents the transient activity which usually allows for reasonable mean currents by transporting the excess of negative vorticity from the interior, through the inertial layer to the walls, where it is dissipated (Pedlosky, 1996). Using a barotropic QG approximation, Dengg (1992) showed that free-slip flows tend not to separate from a cape compared to the clear separation observed with no-slip flows, whatever the value of the wind forcing. For all of these reasons, it seems safer to use the no-slip boundary condition, even if it requires unrealistically large viscosity values in order to resolve the boundary viscous sub-layer. Nonetheless, these studies fail to realize some important issues. The absence of transients and separation, under the free-slip boundary condition, is connected to the fact that most of those models fail to produce relative vorticity at the walls. This is because the relative vorticity at the boundary is specified to be zero for reasons of simplicity. Therefore, those studies fail to note that, even under free-slip, flows can produce relative vorticity simply because of the coastline curvature. Hence, absence of transients in a square basin is due to the idealized straight walls. If the walls were curved (or, in more general sense, irregular, as they are in nature), there is a chance that transients would appear and play the important role of transporting excess of negative vorticity from the interior to the walls. For the same reason, separation of the oceanic currents around a cape can occur because the cape is round and can produce the necessary vorticity required for separation. Of course, due to their fractal nature, the curvature of the coastline depends on the sampling resolution chosen to represent the coastline. Therefore, the knowledge about coastline curvature is subjective. This, in itself, would be a good reason for not considering the free-slip boundary condition for practical ocean modelling. Nonetheless, we would like to revisit the debate between free-slip and no-slip and investigate if, at least from a theoretical point of view (when the curvature is known), use of free-slip is permissible. For this reason, we discard all baroclinic processes and only consider an idealized model of the ocean, the so-called shallow water model, in presence of irregular boundaries and driven solely by wind

friction. The description of both geostrophic and ageostrophic motions in this model allows for observations of the interactions between the two kinds of motions which may be important, especially in presence of irregular boundaries. In terms of physics and geometrical representations, our study contrasts with and should be an improvement over earlier theoretical studies based on the QG approximation and rectangular basins.

The thesis is organized as follows. In Chapter 2, we present the different numerical methods and, in Chapter 3, we test them for simple test-cases in order to understand the effective truncation order and cost of these methods in presence of irregular domains. In Chapter 4, we further analyze the issue of discretization in FD models and, in particular, how it relates to vorticity budgets of the whole basin. In Chapter 5, we investigate the inertial run-away problem under free-slip boundary conditions in irregular domains. Conclusions are presented in Chapter 6.

Chapter 2

Presentation of the Numerical Methods

In this chapter, we review the three numerical methods and the different models we will use in this thesis. In particular, we stress the limitations of each as it relates to the discretization of irregular domains. In the case of the spectral element method, we contribute to the development of the method by proposing our own adaptive technique. Furthermore, we present our own implementation of curved spectral elements. Although curved elements are quite natural to the spectral element method, we found very little information in the literature with respect to their implementation.

The idealized equations we propose to solve are the shallow water (SW) equations. These equations are grossly simplified compared to the primitive equations. Nonetheless, the dynamical processes involved in the formation of wind-driven circulations and the interactions with irregular coastlines are similar enough that we can restrict ourselves to these equations as an introductory study. The equations are

$$\partial_t \mathbf{u} + \mathbf{u} \cdot \nabla \mathbf{u} + f \mathbf{k} \times \mathbf{u} + g \nabla \eta = \frac{\tau}{h} + \nu \nabla^2 \mathbf{u} \quad (2.1)$$

$$\partial_t \eta + \nabla \cdot (\mathbf{u} h) = 0 \quad , \quad (2.2)$$

where symbols are defined in Table 1. These equations correspond to a Boussinesq, hydrostatic, homogeneous ocean in which we assume that there is no vertical structure, reducing the real three-dimensional (3D) problem to a simple two-dimensional (2D) problem. One remark concerns the treatment of the gravity waves in these equations. The natural speed of barotropic gravity waves is

\sqrt{gH} where $g = 9.81 \text{ m s}^{-2}$ is the acceleration due to gravity and H is the typical oceanic depth. Since a reasonable value for H is about 4000 m, the phase speed for barotropic gravity waves is about 200 m/s. In order to use reasonable time-steps and be able to perform long time simulations, these modes have to be slowed down by using a “reduced” gravity. This approach is not inconsistent with the actual physics of the ocean. In fact, in the presence of a thermocline and a deep layer at rest below the thermocline, the SW equations with reduced gravity represent, in some sense, the first baroclinic mode dynamics, i.e., the dynamics of the upper layer. Indeed, this upper layer happens to be the location of the most intense dynamical events. The reduced gravity is defined as $g' = g \Delta \rho / \rho_0$ where $\Delta \rho$ is the jump in density through the pycnocline and ρ_0 the average value for the density of the ocean. For example, the Kelvin waves observed in the equatorial Pacific and along the western American coast have phase speed of 2-3 m/s (Boulanger and Fu, 1996; Ramp *et al.*, 1997), close to the phase speed of 3.16 m/s obtained in a SW reduced gravity model where the reduced gravity is fixed at 10^{-2} m s^{-2} and the depth above the thermocline is taken to be 1000 m. Hence, these equations are consistent with a first order approximation of the physical processes involved in the layer above the thermocline.

(x, y, z)	the coordinate system (east-north-upward)
$\mathbf{u} = (u, v, 0)$	horizontal velocity vertically averaged
η	elevation of the water surface taken from rest
h_b	height of the water column above the oceanic floor at rest
$\mathbf{k} = (0, 0, 1)$	unit vector normal to the horizontal plane pointing upward
∇	gradient operator
$h = \eta + h_b$	fluid layer thickness
$\mathbf{U} = h\mathbf{u}$	vertically averaged horizontal flux of mass
$q = (\zeta + f)/h$	potential vorticity
$\zeta = \mathbf{k} \cdot (\nabla \times \mathbf{u})$	relative vorticity
$f = f_0 + \beta y$	Coriolis parameter varying with latitude
$B = g\eta + \frac{1}{2}\mathbf{u} \cdot \mathbf{u}$	Bernoulli function
ν	dynamic eddy viscosity
$g' = 0.01 \text{ m.s}^{-2}$	reduced gravity acceleration
$f_0 = 1.0285 \cdot 10^{-4} \text{ s}^{-1}$	defined at 45° N deg.
$\beta = 1.607 \cdot 10^{-11} \text{ m}^{-1}\text{s}^{-1}$	defined at 45° N deg.
$L_{Rossby} = 31.22 \text{ km}$	the Rossby radius
L_x, L_y	the lengths of the basin (=1000 km when unspecified)
$\boldsymbol{\tau} = (\tau_x, \tau_y)$	wind stress in m^2s^{-2} . For the single gyre wind forcing, $\tau_x = -10^{-4} \sin(\pi y/L_y)$ and $\tau_y = 0$.
Ω	basin domain
$\delta\Omega$	boundary of the basin domain
\mathbf{n}	normal vector oriented outward the domain
$\mathbf{C} = \mathbf{u} \cdot \nabla \mathbf{u} + f \mathbf{k} \times \mathbf{u}$	Advection-Coriolis terms

Table 2.1: List of variables in (2.1–2.2)

2.1 The Time Discretization

Several time-stepping schemes are considered and used in conjunction with one of the spatial discretization techniques proposed in the following sections. For clarity, we review the time-stepping techniques separately in this section. Let us consider the equation

$$\frac{\partial u}{\partial t} = F(u) . \quad (2.3)$$

The time-operator can be finite-differenced using a Taylor's series expansion truncated after the first term:

$$\frac{\partial u}{\partial t}(t_n) = \frac{u^{n+1} - u^n}{\Delta t} + O(\Delta t) . \quad (2.4)$$

The simplest time discretization consists then of integrating (2.3) given the previous time-step fields. This formulation corresponds to the so-called explicit forward Euler scheme and is only first order accurate

$$u^{n+1} = u^n + \Delta t F(u^n) . \quad (2.5)$$

This formulation is usually recommended for the integration of the dissipative or friction terms, because no large precision is required in time, as long as the small scale numerical noise are damped (and the scheme is stable). For ensuring stability, a condition on the magnitude of the time step, Δt , applies. For instance, when $F(u) = \nu \nabla^2 u$ (a viscous dissipation term), this condition is

$$\frac{2\nu\Delta t}{\Delta x^2} < 1 . \quad (2.6)$$

Unfortunately, the forward Euler scheme is not neutral for various problems, in the sense that some quantities such as mass, momentum or energy are not conserved but may decay or grow as the simulation is advanced in time. When these quantities grow with time, the model is of course unstable. This happens, for instance, when $F(u)$ represents the Coriolis terms. In order to better conserve certain quantities, a better scheme is the explicit leapfrog scheme

$$u^{n+1} = u^{n-1} + 2\Delta t F(u^n) , \quad (2.7)$$

based on a second order truncation

$$\frac{\partial u}{\partial t}(t_n) = \frac{u^{n+1} - u^{n-1}}{\Delta t} + O(\Delta t^2) . \quad (2.8)$$

The leapfrog scheme is thus centered in time. As the Euler scheme, this scheme is restricted to certain conditions for stability. For instance, if $F(u)$ represents an advection or a wave propagation problem and using the definition that the Courant number is given by

$$C = \frac{c\Delta t}{\Delta x} \quad (2.9)$$

where c is a phase speed or an advection velocity, the CFL (Courant-Friedrich-Levy) condition implies that

$$C < 1 \quad (2.10)$$

for stability. The Leapfrog scheme is neutral and conditionally stable for problems involving, for instance, Coriolis or nonlinear advection terms, and is unstable for dissipative terms. Moreover, the leapfrog scheme requires a time-filtering, because the non-linearities and round-off errors lead to a decoupling of the solution between even and odd time steps. In order to avoid restriction of time-step magnitude, other time-integrations techniques were introduced. They include implicit and semi-implicit schemes. Nonetheless, these schemes have to respect a certain condition on the Courant number for ensuring a good accuracy. The semi-implicit¹ scheme consists of

$$u^{n+1} = u^n + \Delta t F(u^{n+1/2}) , \quad (2.11)$$

where $F(u^{n+1/2}) = 1/2(F(u^{n+1}) + F(u^n))$ and the fully-implicit scheme (also called the backward Euler scheme) is implemented as

$$u^{n+1} = u^n + \Delta t F(u^{n+1}) . \quad (2.12)$$

The advantage of the semi-implicit treatment is that the time-operator is centered and second-order. For the Coriolis terms, the fully-implicit is dissipative, and the semi-implicit (centered in time) is neutral. For the treatment of the fast linear gravity waves present in the shallow water equations, the advantage of using a semi-implicit or fully-implicit technique is that there is no restriction on time-steps (the domain of stability of the models is extended) but at the expense of

¹As termed in the atmospheric community in opposition to the full implicit formulation but also called the trapezoidal rule or the Crank-Nicolson scheme in other fields.

solving a matrix problem due to the coupling of the variables through partial derivatives. The disadvantage of these two techniques is that some physical processes, such as gravity waves, are slowed down if a too large time-step is used (i.e., $C > 1$). This may have consequences for the interactions of important dynamical processes (the geostrophic and ageostrophic modes) and, therefore, this may lead to a less accurate representation of the cascade of energy (as mentioned in Bartello and Thomas, 1996).

The non-linear advective terms, $\mathbf{u} \cdot \nabla \mathbf{u}$, require a special treatment. When we consider the computation of \mathbf{u}^{n+1} , they can be computed using the previous time step as $\mathbf{u}^n \cdot \nabla \mathbf{u}^n$. Then, if the time-operator is centered and leapfrog, the non-linear terms are neutrally treated, otherwise, they are off-centered for the other time-integration schemes and may be unstable or dissipative depending on the time integration techniques. The non-linear terms can be treated implicitly as $\mathbf{u}^n \cdot \nabla \mathbf{u}^{n+1}$ or fully implicit using an iterative procedure. Another way is to use an explicit 4th order Adams-Bashforth formulation

$$u^{n+1} = u^n + \frac{\Delta t}{12} [23 F(u^n) - 16 F(u^{n-1}) + 5 F(u^{n-2})] . \quad (2.13)$$

The scheme is off-centered. It requires saving fields from several previous time-steps and the time-step is limited by a CFL condition. Use of Runge-Kutta techniques is also possible, the fourth order one having the advantage of good quadratic conserving properties, such as for the energy. But Runge-Kutta techniques require sub-step time integrations as in this 4th order example:

$$\begin{cases} h_1 = F(u^n, t^n) \\ h_2 = F(u^n + \Delta t h_1/2, t^n + \Delta t/2) \\ h_3 = F(u^n + \Delta t h_2/2, t^n + \Delta t/2) \\ h_4 = F(u^n + \Delta t h_3, t^n + \Delta t) \\ u^{n+1} = u^n + \Delta t(h_1 + 2h_2 + 2h_3 + h_4)/6 . \end{cases} \quad (2.14)$$

The Runge-Kutta formulations are neutral for all phenomena, very accurate, and require a CFL condition. Adams-Bashforth formulations are usually recommended for non-linear

integrations, but have the practical disadvantage of requiring smaller time-steps than equivalent order Runge-Kutta integrations, to the point that there is no definite advantage of one technique over the other². Hereafter, we tend to use the 4th order Runge Kutta integration because of its accuracy and because it does not require any time filtering.

A completely different time-stepping approach consists of using the Lagrangian framework (the grid follows the particles) instead of the Eulerian framework implicitly assumed previously (the grid is fixed in time). The Lagrangian time-integration takes advantage of the fact that the dynamical equations are simplified when written in a Lagrangian form

$$D_t \mathbf{u} + f \mathbf{k} \times \mathbf{u} + g \nabla \eta = \frac{\tau}{h} + \nu \nabla^2 \mathbf{u} \quad (2.15)$$

$$D_t \ln h + \nabla \cdot \mathbf{u} = 0 , \quad (2.16)$$

where D_t is the Lagrangian or total time derivative. This is another way of saying that the particle trajectory is the characteristic line for the advective-only problem. Hence, the problematic non-linear terms appearing in the equations do not appear explicitly (except for the term in the mass balance). The main difficulty is in following the particles that form the flow, and especially expressing the right-hand-side terms. In order to avoid this problem, the so-called semi-Lagrangian formulation was developed which takes advantage of both the Lagrangian and Eulerian frameworks (see Staniforth and Côté, 1991, for a review). The right-hand-side terms are discretized on the Eulerian framework (in which derivatives are easy to express) and the time-derivative is treated on the Lagrangian framework. The advantage is in keeping a fixed grid or domain in time. An interpolation procedure is used in order to transfer information from the Eulerian grid to the Lagrangian grid (the particle trajectories). As the equations are time-stepped along the advective characteristic lines (the particle trajectories), there are no limitations imposed by numerical stability on the magnitude of the time-step

²This was observed for a single gyre wind-driven experiment in a square domain (the one used in Section 3.4) using the second order C-grid FD model given in Section 2.2.2.

due to the advective terms. Therefore, the method is effective in advection dominated flows. To be precise, according to Bartello and Thomas (1996), the method is effective only if the spectrum of energy is very steep (not too much energy at the smallest scales). Moreover, a semi-implicit or fully-implicit method can be added to the semi-Lagrangian treatment of the equations (Robert, 1981). Thus the model has virtually no limitations due to stability regarding time-step magnitude with respect to any physical process described by the momentum equations. However, the presence of orography is troublesome in semi-Lagrangian methods, effectively reducing the allowable time-step (Ritchie and Tanguay, 1996). The advantage of using semi-Lagrangian methods in an ocean where the topography is steep is, hence, unclear.

Since the equations are iterated in time, the interpolation can be very damaging to the conservation properties of the flow (mass or energy). That is why modelers have to use high order interpolation schemes (cubic or more). Nonetheless, the interpolation technique is usually responsible for a large numerical dissipation, difficult to minimize. On the other hand, these models can run without explicit eddy-viscosity or diffusivity. Proponents of the semi-Lagrangian method never fail to mention that their models run without explicit numerical viscosity, whereas opponents note that semi-Lagrangian models offer no control over this implicit viscosity. Another disadvantage of the semi-Lagrangian technique when coupled to the semi-implicit or implicit method is related to the same argument against the semi-implicit and implicit methods. Namely, that too large a time-step distorts the physical processes and misrepresents the real cascade of energy.

2.2 Finite Difference Models

2.2.1 Introduction

The order of a finite-difference (FD) model is given by a Taylor series expansion of the numerical formulation. For instance, the first

derivative of ϕ given by a three point (equally spaced) formula

$$\frac{\partial \phi}{\partial x}(x_i) = \frac{\phi_{i+1} - \phi_{i-1}}{2\Delta x} + O(\Delta x^2) \quad (2.17)$$

ensures a second order accuracy. This means that if resolution is doubled, accuracy increases by a factor of 4. Higher order formulations are possible (Dietrich *et al.*, 1993), but most FD ocean models use second order schemes. In more than one dimensional problems, the best accuracy is obtained by using Cartesian-like grids (this includes curvilinear grids). And if there is any stretching of the grid, a change of less than 5% to 10% in size is usually recommended between two neighboring computational cells.

When finite difference models make use of Cartesian-like grids, a complex coastline is represented by a series of artificial “steps”. More precisely, where the orientation of the boundary does not correspond to that of the grid, discretization of the boundary introduces a series of artificial “steps” along the coast (see Fig.2.1). Curvilinear models exist that tend to follow the coastline, but they usually fail as soon as the complexity of the coastline is too large (too many capes and bays). A dramatic example is the description of straits when only few points are available (Fig.2.2). In that situation, the strait width must take values in a set of discrete numbers at the price of misrepresenting the width and therefore the exchange of water masses. We are concerned with the issue of coastline representation in FD models and, particularly, we want to investigate the accuracy of FD models in presence of step-like lateral walls. These steps can be viewed as singularities (tips of land) around which the oceanic currents flow. A question therefore arises concerning the influence of resolution versus the influence of steps; the smaller the grid cell, the larger the number of steps along a coastline. It is then not clear whether the solution becomes more accurate (due to higher precision in the interior) or less accurate (due to an increased number of singularities or steps along the boundaries). If the model solution is less accurate with increasing resolution in presence of steps means that the model formulation becomes inconsistent in presence of steps. This may occur because FD models are made to be consistent in open or closed

rectangular domains but are not necessarily in the more general case of irregular domains. In particular, we raise the problem of the computation of the advective and viscous terms in presence of steps. On the other hand, consistency should apply to the linear inviscid SW models.

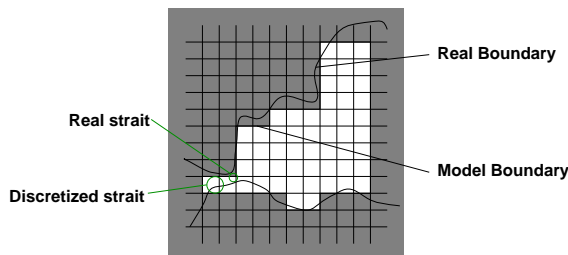


Figure 2.2: Effect of a poor resolution on the geometry of a strait. This one is widened by about 100%. Straits are of great importance because they control the exchange of water between two ocean basins.

The same problem arises in the vertical discretization of the topography in three-dimensional FD models of the ocean. In models of Bryan-Cox type (Bryan, 1969) based on the primitive equations, the vertical axis is discretized at various constant depths. They are called leveled or z -coordinate models. In these models, the topography follows a step-like representation and therefore they are prone to problems similar to the ones mentioned above. For instance, the equivalent difficulty in z -coordinate models to the description of straits is the description of sills. The depth of sills or other important topographical features has to be taken from a set of discrete depths. It was early realized that this step-like representation had detrimental effects on the overall circulation. For instance, z -coordinate models have meridional circulations which are known to be sensitive to the details of how the bottom boundary is represented. The issue is that they do not accurately advect denser waters along slopes and overestimate diapycnal mixing (Gerdes, 1993; Roberts *et al.*, 1996; Roberts and Wood, 1997). Different strategies were proposed to circumvent the problem. The first strategy was to change the vertical coordinate, z , to a following terrain coordinate, σ (Phillips, 1957; Blumberg and Mellor, 1983). But σ -coordinate models encounter other known limitations, such

as pressure gradient errors and artificial diapycnal mixing. A second strategy is to use a layered (or ρ -coordinate) model (Bleck, 1978; Bleck and Boudra, 1981). Roberts *et al.* (1996) compared the behavior of the simulated North Atlantic in a z -model and in an isopycnal model (ρ -model). In particular, they noted that the z -model has more trouble in representing a realistic outflow from the Greenland basin (GIN). Roberts and Wood (1997) extended the study by systematically studying the effect of modifying the topography of the sill at the outflow of GIN and noted the high sensitivity of the model. The same observation was made by Winton (1997) in a more idealized geometry of the North Atlantic. Winton *et al.* (1998) finally demonstrated that it is a resolution problem. When the resolution was high enough to resolve the bottom boundary layer and to resolve the slope, the flow is realistic enough. However, the required resolution is unrealistic even for modern z -models; therefore, they recommended the use of explicit bottom boundary layer models or the use of isopycnal models (although those ones have also their own limitations, namely related to the isopycnal layers intersecting the topography or the surface.) From a different perspective, Hirst and McDougall (1996) noted that, in coarse resolution z -models, the Gent and McWilliams (1990) turbulence scheme remarkably enhances the conservation of water properties along topographical slopes. Another approach was proposed by Adcroft *et al.* (1997). They showed interesting use of “shaved” cells in z -models. The topography is then piecewise linear, instead of being piecewise constant as in usual z -models.

All these difficulties in representing flows along sloping topography should warn us of possible problems for the horizontal circulation in the presence of step-like coastlines. Using a shallow water model, Schwab and Beletsky (1998) found that a Kelvin wave moving along a coastline is sensitive to the presence of steps. The steps have mainly a retardation effect on the wave, the effect diminishing with higher resolution. These results are reproduced in Figure 2.3 using the C-grid model of Section 2.2.2. Four grids in total were used: two grids with no rotation of the basin showing no step along the boundaries at 10 and 5 km resolution and two grids with a 30° rotation of the basin

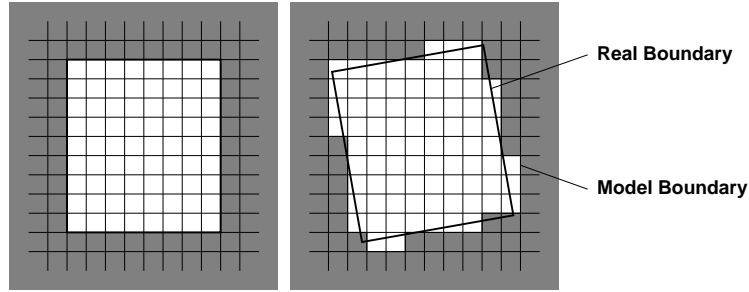


Figure 2.1: Effect of the rotation on the discretization of a square domain. When the sides are no more aligned with the discretization axis, step-like features occur along the walls.

relative to the discretization axes showing steps along the walls at also 10 and 5 km resolution. That higher resolution decreases the retardation effect is consistent with the idea that Kelvin waves should not be sensitive to coastline details, at scales small compared to the Rossby radius of deformation. In Figure 2.3, for the highest resolution runs (5 km), the retardation effect is still noticeable but it is much weaker compared to the runs at 10 km resolution. Since the radius of deformation is 31 km in these runs, these results imply that we should resolve the Rossby radius with about ten points for a second order formulation. This retardation effect was also noted in circular lakes by Beletsky *et al.* (1997) for different kinds of staggering of the grid and vertical representations. One consequence for modelling the ocean is that the fast modes of an ocean basin (the Kelvin modes) will be misrepresented, especially if the model resolution is coarse. Therefore, transient responses of the ocean, such as the El-Niño Kelvin wave along the Western America may be retarded, which may have consequences on the period of occurrences of El-Niño events according to the delayed oscillator theory (Schopf and Suarez, 1988). For instance, in the study of Soraes *et al.* (1999), there are only two points to represent the Rossby radius of deformation at 20° North. This means that their results are questionable concerning the flux and the timing of Kelvin waves leaving the equator and going poleward.

2.2.2 The Three Staggingings Used

To ensure stability in primitive variable or shallow water models, the variables are usually staggered in space, in the sense that the discrete location of the different variables may differ. Several standard staggering techniques are used in ocean modelling: the non-staggered A-grid (Dietrich *et al.*, 1993), the B-grid (Bryan, 1969; Cox, 1984) or the C-grid (Bleck and Boudra, 1981; Blumberg and Mellor, 1983), as illustrated in Fig. 2.4. The A-grid leads to spurious modes of oscillation, fed by non-linear interactions and round-off errors. These spurious modes are ultimately unstable, but the A-grid can be stabilized if higher order formulations are used. The B-grid has better dispersion errors at coarse resolution for propagating planetary or Rossby waves than C-grid, and does worse for pure gravity waves (Batteen and Han, 1981).

FD models can be formulated to conserve energy and/or enstrophy (Arakawa, 1966; Sadourny, 1975; Abramopoulos, 1988; Arakawa and Hsu, 1990; Hólín, 1996). For instance, it is relatively easy to formulate an A-grid energy conserving model, from the point of view of the finite volume (FV) method. But conserving the energy exactly only retards the occurrence of spurious numerical noise (this model is detailed in Appendix A). If the model was also enstrophy conserving (which, according to Abramopoulos, 1988, is achievable but very expensive), the occurrence of spurious numerical noise would be even more difficult and hence, the model would be stabilized.

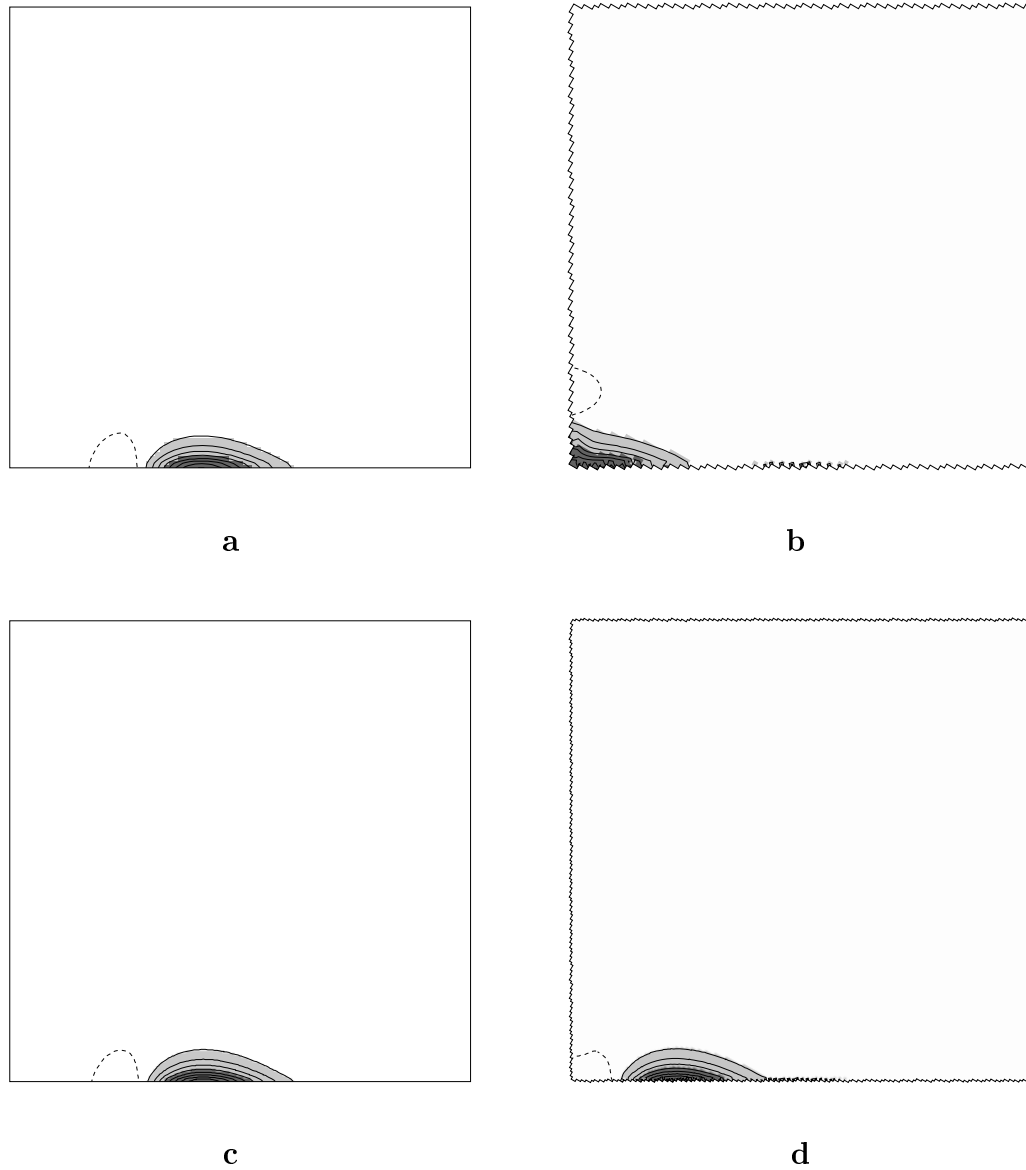


Figure 2.3: Elevation field for the Kelvin retardation problem in presence of steps along the walls at two different resolutions. α represents the rotation angle of the grid relative to the discretization axes. **a**, 10 km, $\alpha = 0$; **b**, 10 km, $\alpha = 30^\circ$; **c**, 5 km, $\alpha = 0$; **d**, 5 km, $\alpha = 30^\circ$. The dashed line is the -0.01 m contour, the solid lines are contours from 0.1 to 1.0 m with an increment of 0.1 m.

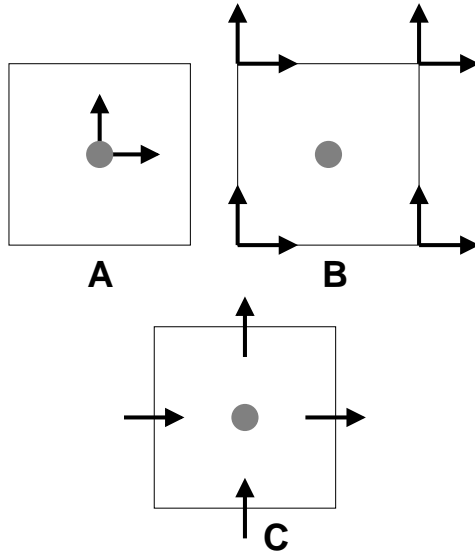


Figure 2.4: The three major horizontal staggerings for the primitive equations. Left the A-grid, center the B-grid, right the C-grid. Velocities components are located by the arrows, the pressure or elevation point is located by a grey disk.

The C-grid Formulation

The C-grid derived models, such as the popular POM family of models developed from Blumberg and Mellor (1983), tend to be used preferentially for high-resolution regional studies. The C-grid FD model used in this thesis is the one formulated by Sadourny (1975). This model is enstrophy conserving. The nonlinear terms are split into a gradient term and a rotational term. To simplify the following discussion, we leave the time derivative being continuous. Using standart notation, the discretized shallow water equations are

$$\partial_t u - \bar{q}^y \bar{V}^{xy} + D_x^- B = \frac{\tau_x}{\bar{h}^x} + F_x \quad (2.18)$$

$$\partial_t v + \bar{q}^x \bar{U}^{xy} + D_y^- B = \frac{\tau_y}{\bar{h}^y} + F_y \quad (2.19)$$

$$\partial_t \eta + D_x^+ U + D_y^+ V = 0 \quad (2.20)$$

The discretized potential vorticity is given by $q = (f + \zeta)/\bar{h}^{xy}$ where $\zeta = D_x^- v - D_y^- u$ is the relative vorticity. The discretized mass fluxes are given by $U = u\bar{h}^x$, $V = v\bar{h}^y$, the discretized Bernoulli function is given by

$B = g\eta + \frac{1}{2}(\bar{u}^{2x} + \bar{v}^{2y})$ and F_x and F_y are the viscous forces. The off-centered differencing operators in the x direction are defined by

$$D_x^- \phi = \frac{\phi_{ij} - \phi_{i-1,j}}{\Delta x}, D_x^+ \phi = \frac{\phi_{i+1,j} - \phi_{ij}}{\Delta x};$$

and the averaging operator defined by $\bar{\phi}^x$ is a double point average $= \frac{1}{2}(\phi_{ij} + \phi_{i-1,j})$. Similar definitions apply along the y direction. (2.18), (2.19) and (2.20) ensure a second order accuracy to the computation of the velocity and elevation fields. The kinematic boundary condition is no normal flow and the dynamic boundary condition is free-slip, unless otherwise specified. The C-grid model, in which the non-linear terms have been split into a rotational part and a gradient part, requires that vorticity be specified at boundary points. We set the relative vorticity to zero along the model boundary, which is consistent with the free-slip boundary condition along straight walls.

The B-grid

The B-grid is employed in the popular MOM family of ocean models. The MOM model is a z -model and was developed from Bryan and Cox (1967) and Bryan (1969) and following investigators. The B-staggering suits more naturally the no-slip boundary condition, since the velocity points are located at the corners of the computational cell. Unlike the C-grid, there are no ambiguities in the way the dynamical boundary condition is imposed at tips of the continents. The B-grid is also well known for having a better dispersion relationship for Rossby waves at very coarse resolution than does the C-grid (Battteen and Han, 1981). This makes this staggering technique more suitable for coarsely-resolved global climate studies. However, we are interested in how this configuration behaves in the presence of steps along the walls. From Cox (1979), it appears that the B-grid model under the no-slip boundary condition, just as the C-grid (Adcroft and Marshall, 1998), is not very sensitive to the presence of lateral steps, therefore, we prefer to focus on the behavior of the B-grid model with a free-slip boundary condition.

On the B-grid, the discretized shallow wa-

ter equations become

$$\begin{aligned} \partial_t u + u D_x^o u + v D_y^o u \\ - f v + g D_x^- \bar{\eta}^y = \frac{\tau_x}{\bar{h}^y} + F_x \end{aligned} \quad (2.21)$$

$$\begin{aligned} \partial_t v + u D_x^o v + v D_y^o v \\ + f u + g D_y^- \bar{\eta}^x = \frac{\tau_y}{\bar{h}^x} + F_y \end{aligned} \quad (2.22)$$

$$\partial_t \eta + D_x^+ \bar{U}^y + D_y^+ \bar{V}^x = 0 \quad (2.23)$$

where $U = u \bar{h}^x$, $V = v \bar{h}^y$. The differencing operator D_x^o (and D_y^o in the similar way) are defined by

$$D_x^o \phi = \frac{\phi_{i+1,j} - \phi_{i-1,j}}{2\Delta x}.$$

Eq. (2.21) and (2.23) ensure a second order accuracy to the numerical solution. The difficulty when applying the free-slip boundary condition to a B-grid model is that it requires a prognostic equation for the velocity component tangential to the wall (in the more general situation of a irregular geometry, the B-grid would require equations for velocity nodes at tips of land-cells). Therefore we use,

$$\partial_t u_s + u_s D_s^o u_s + g D_s^- \eta^* = \frac{\tau_x}{h^*} + F_s \quad (2.24)$$

where s represents the tangential direction, and η^* , the elevation point along the wall at half a point from the considered velocity node.

The A-grid

The argument behind using an A-grid configuration is that the C-grid presents the disadvantage of separate locations for u and v -components of the velocity. This means that, at coarse resolution, the truncation errors in the computation of the Coriolis terms can be fairly large. According to Adcroft *et al.* (1998), these errors trigger numerical noise when the Rossby radius is not well resolved. From a programming point of view, having all the variables located at the same points makes everything easier (physical parameterizations, conservative FV formulation, graphic output, ...). The A-grid arrangement of the variables is known to be an

unstable second order formulation. Nonetheless, it is possible to run an A-grid model if all the terms are accurate at fourth order. A high-order method is cost effective in terms of accuracy (Sanderson, 1998), as long as the physical processes are resolved and the spectrum of the resolved fields is steep enough. Dietrich *et al.* (1993), hereafter D93, developed such a model. The model is three-dimensional and uses a no-slip boundary condition. We modify the model to represent the shallow water equations, keeping the fourth order formulation for all the terms (except the diffusion), and we incorporate the free-slip boundary condition. All the equations are prognostic and integrated explicitly in time using a 4th order Runge-Kutta scheme. On an A-grid and using the same notation, the shallow water equations lead to

$$\begin{aligned} \partial_t u + u D_{4,x} u + v D_{4,y} u \\ - f v + g D_{4,x} \eta = \frac{\tau_x}{h} + F_x \end{aligned} \quad (2.25)$$

$$\begin{aligned} \partial_t v + u D_{4,x} v + v D_{4,y} v \\ + f u + g D_{4,y} \eta = \frac{\tau_y}{h} + F_y \end{aligned} \quad (2.26)$$

$$\partial_t \eta + D_{4,x}(uh) + D_{4,y}(vh) = 0 \quad (2.27)$$

The differencing operators, $D_{4,x}$ and $D_{4,y}$, are fourth order operators. Equations 2.25–2.27 ensure a fourth order accuracy to the numerical solution, except for the viscous terms F_x and F_y , which remain second order. The difficulty with the A-grid at fourth order is to retain the fourth order right to the wall. This is possible only if off-centered differentiation formulae and interpolation are used. If this is not done, the model tends to be unstable with free-slip boundary conditions (as demonstrated in the next chapter.)

2.3 Finite Element Models

2.3.1 Introduction

In this section, we present several finite element (FE) models, all based on triangular elements. The development of the FE method was contiguous to the development of computers in the early 60s and 70s. By the end of 70s, they were well established. They became particularly popular in engineering for

the computation of stresses over structures, and somewhat popular in fluid mechanics and electricity. In all cases, they were and are still used because of the great flexibility they offer in term of geometrical representation, sometimes despite the cost or the lack of stability of the method. In structural mechanics, they have the decisive advantage of being able to follow the deformation of the mesh due to stress (Lagrangian time formulation), making the methods quite “natural” to this field. In electricity, the absence of non-linear terms in most applications render the method reasonably successful. But in fluid mechanics, the method has always suffered from a lack of overall stability, from a lack of accuracy in the computation of the advective terms and from a very large cost, to the point that most commercial models used for engineering applications preferentially use the finite volume (FV) method along with near regular meshes (c.f., IDEAS, Star-CD, ...). The disadvantage of the FV methods is that they are usually of low order and that they require near regular meshes to ensure good performances. This means that they are not very suitable to model the ocean.

The problem of stability in FE methods in fluid mechanics was early analyzed by Ladyzhenskaya (1969), Babouska (1971) and Brezzi (1974), who gave their names to the so-called Ladyzhenskaya, Babouska and Brezzi (LBB) stability condition. Their work focuses on the Stokes equations and they demonstrated the need, in fluid mechanics FE methods, for using different basis functions for the velocity and pressure. This was equivalent to staggering the grid in space, as was done for the FD methods. Furthermore, not any combination of basis functions satisfies the LBB condition (Fortin and Fortin, 1985; Pierre, 1988; Idelsohn *et al.*, 1995; Le Roux *et al.*, 1998). Arnold *et al.* (1984) and Fortin and Fortin (1985) emphasized that one simple way to stabilize equal-order schemes is to add the so-called bubble function, and that this method does not lead necessarily to an additional cost, thanks to static condensation techniques (some easy manual Gaussian elimination before solving numerically the matrix problem). But, since, according to Pierre (1988), these methods are equivalent to adding a penalty term in the fluid equations, they may be over-dissipative in the context of unsteady flows and the more general Navier-Stokes equations.

Mainly, the LBB condition comes down to increasing the order (or the number of degrees of freedom) of the basis functions for the velocity compared to the basis function for the pressure. However, one unresolved issue related to the LBB condition is its relevance for the shallow water equations. The three shallow water equations are similar enough that they can be generalized to one vector equation:

$$\frac{\partial V}{\partial t} + \frac{\partial F}{\partial x} + \frac{\partial G}{\partial y} = H \quad (2.28)$$

where $V = (uh, vh, h)^t$, $F = (uuh + gh^2/2, uvh, uh)^t$, $G = (vvh + gh^2/2, vhh)^t$ and H includes the Coriolis, dissipation and forcing terms. Therefore, there is no intuitive reason for lowering the order for one variable compared to the others. The only loss of similarity between these equations comes from the boundary conditions which only apply to the velocity. This is however a slight loss of similarity which only applies to the elements sharing a face or a vertex with the boundary. Hence, the need for lowering the order for pressure may not apply to all elements of the mesh. There is evidence, however, that it is better to use a combination of basis functions that fulfills the LBB condition, even in the broader context of the shallow water equations (Le Roux *et al.*, 1998). Our own experience pinpoints that the behavior of the solution depends on the application. We are definitely missing a general theory of stability for the FE approximation in the broader context of the shallow water equations.

The fact that the pressure basis functions have to be of lower order compared to the velocity basis functions means that the overall truncation order of the stabilized FE methods for the shallow water equations is probably lower than the one permitted by the velocity basis functions. And, since the other disadvantage of these stable FE methods is the cumbersome and time consuming solving of a large matrix problem (especially when all the variables are coupled), it is doubtful that these methods can compete with today's FD ocean models in terms of cost and accuracy.

We focus herein on four different FE models: the Lynch and Werner model (1987; 1991) (also called the Quoddy model and the

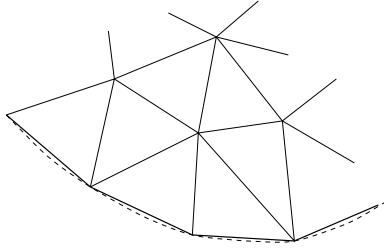
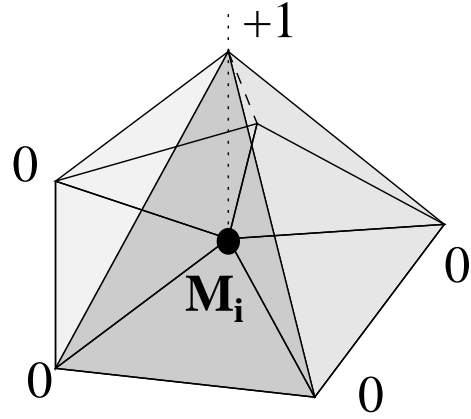


Figure 2.5: Triangulation of the domain.

only one of the four used for coastal oceanography), the Le Roux *et al.* (2000; hereafter LLS) model, the Hua and Thomasset (1984) model and the Peraire *et al.* (1986; hereafter PZM) model. Only one model, the LLS model, among the four satisfies the LBB condition of stability. The Quoddy and the PZM models use a non-staggered (i.e., equal order) formulation of the variables and therefore require some kind of stabilizing “trick” which we will present and discuss. Due to their equal-order formulation, these two models are the simplest, in some sense, of the four for the same reason that the A-grid FD formulation is simpler than the other staggering techniques. In the context of the finite elements, there are some additional technical advantages to using non-staggering formulations which stems from a lower number of matrices to define and to inverse. Also, it unifies the use of gradient or divergence operators. In general, equal-order models are fairly easy to implement from scratch. Hence, they can be more appealing than more complex LBB complying formulations.

2.3.2 The Galerkin Formulation

Most FE methods are based on the Galerkin formulation. In these models, the domain, Ω , is broken up into a set of conformal elements (conformal in the sense that all elements connect to neighboring elements through common vertices). The form of the elements is rather unspecified but triangles or quadrangles are usually recommended. We favor the use of triangles (Fig. 2.5) because complex domains are more easily divided into triangles than quadrangles. For each vertex of the mesh, M_i , and in the context of linear finite elements, there is an associated basis func-

Figure 2.6: ϕ_i , the basis function related to the node M_i .

tion, ϕ_i . This basis function is piecewise linear in each triangle to which M_i belongs and forms a “hat” on top of M_i (Fig. 2.6). Over the rest of the domain, the basis function is zero. Let us consider the equation

$$\frac{\partial u}{\partial t} = -\frac{\partial u}{\partial x} . \quad (2.29)$$

u can be approximated by $\hat{u} = \sum_j \hat{u}_j \phi_j$. The finite element approximation of this equation consists on multiplying 2.29 by a test function and then integrating the resulting equation over the whole domain. There is a certain freedom upon the choice for the test-function, though. In the collocation method, the test-function is defined as the $\delta(\mathbf{x} - \mathbf{x}_i)$ (the Dirac-delta function). Then, the formulation bares similarities to the FD method. If both the basis functions and the test-functions are piecewise constant, the formulation is similar to the FV method. The Galerkin approximation is to take for the test-function, ϕ_i , which is used to approximate u . Thus, the discretized version of (2.29) is

$$\sum_j \frac{\partial \hat{u}_j}{\partial t} \langle \phi_j, \phi_i \rangle = - \sum_j \hat{u}_j \langle \frac{\partial \phi_j}{\partial x}, \phi_i \rangle . \quad (2.30)$$

where $\langle \cdot, \cdot \rangle$ is the inner product defined as $\langle f, g \rangle = \int_{\Omega} f g ds$. This is equivalent to say that the errors generated when discretizing (2.29) are projected onto another subspace of the function space (supposedly, a higher

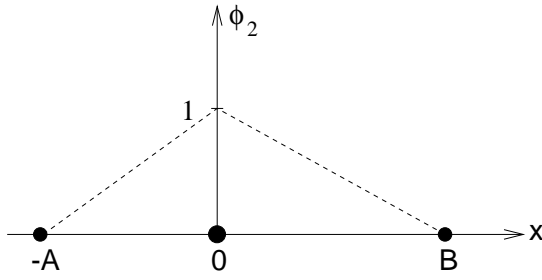


Figure 2.7: ϕ_2 is the basis function related to the node $x_2 = 0$.

degree polynomial subspace). This formulation is said to be “weak” and is also referred to as the weighted residual approach. In some particular cases, it can be shown that the model equations can be described by a functional. This leads to the so-called variational principle. In such a case, the Galerkin approximation minimizes the approximation errors. Since the piecewise linear basis functions, ϕ_i , are not orthogonal, the terms $\langle \phi_j, \phi_i \rangle$ lead to a matrix that has to be solved at each iteration in order to advance the solution in time. This matrix is usually referred to as the mass matrix and noted \mathbf{M} . \mathbf{M} is usually non-diagonal, but sparse. In order to gain computational efficiency, \mathbf{M} is sometimes “lumped”; that is, all non-diagonal terms are summed onto the diagonal to form an artificial diagonal mass matrix. This method bears similarities with the collocation method, as opposed to the Galerkin method, and can lead to a loss in accuracy.

We now consider the issue of using irregularly spaced grid points in FD and FE methods. In the FD method, an irregular spacing of the nodes leads to a loss of order. Let us consider the equation

$$u = \frac{df}{dx} \quad (2.31)$$

Imagine three nodes located along one axis. The length between Node 1 and node 2 is A , and node 2 and node 3 are distanced by B . Without loss of generality, we can impose $x_1 = -A$, $x_2 = 0$ and $x_3 = B$ (Fig. 2.7). The usual centered FD discretization of (2.31) at x_2 gives

$$u_2 = \frac{f_3 - f_1}{A + B} \quad (2.32)$$

As $f_1 = f_2 - A \frac{df}{dx}(x_2) + A^2 \frac{d^2f}{dx^2}(x_2) + O(A^3)$ and $f_3 = f_2 + B \frac{df}{dx}(x_2) + B^2 \frac{d^2f}{dx^2}(x_2) + O(B^3)$,

$$u_2 = \frac{f_3 - f_1}{A + B} = \frac{df}{dx}(x_2) + (B - A) \frac{d^2f}{dx^2}(x_2) + O(A^2 + B^2) \quad (2.33)$$

This formulation is second order if $A = B$ but only first order if $A \neq B$.

The same occurs for the FE method. Using linear “hat” functions to discretize this axis, the Galerkin discretization of (2.31) with the basis functions at node 2 as the test function

$$\langle u, \phi_2 \rangle = \langle \frac{df}{dx}, \phi_2 \rangle \quad (2.34)$$

leads to

$$A(u_1/6 + u_2/3) + B(u_3/6 + u_2/3) = 1/2(f_3 - f_1) \quad (2.35)$$

where u and f are now approximated by $\hat{u} = \sum_{i=1..3} u_i \phi_i$ and $\hat{f} = \sum_{i=1..3} f_i \phi_i$. To demonstrate the problem of using irregular spacing, we use a different approach which consists of using polynomials of increasing order that satisfy (2.31). The maximum order for which (2.35) is consistent gives the truncation order of the scheme. If we take $f(x) = 1$ and $u(x) = 0$, (2.35) is exactly satisfied. If we take $f(x) = x$ and $u(x) = 1$, the same applies. But if we take $f(x) = x^2$ and $u(x) = x$, the equality is no longer true for the general case of $A \neq B$, which means that the numerical method is only first order when the spacing is not constant. Therefore, we expect the order of any FE and FD method to be reduced in the presence of unstructured meshes.

2.3.3 The Different Finite Element Models Tested

The Quoddy Model

The Quoddy model of Lynch and Werner (1987; 1991) is a full 3D baroclinic finite ele-

ment model. This model was successfully applied for coastal and tidal studies on the Scotian Shelf (Hannah *et al.*, 2000) and the Vancouver Island area (Foreman *et al.*, 2000). It was modified to model the shallow water equations, retaining the main characteristic of the Quoddy model, which are: equal order of approximation for velocity and elevation, the divergence of the vertically integrated momentum equations can be recast by using the mass balance equation and eliminating the divergence of the vertically integrated mass flux. This yields a prognostic equation for the elevation of second order in time (a wave equation). Solving numerically for the three equations (two momentum equations and one wave equation) is easy and leads to a stable model, but, does not balance mass locally. To guaranty a better local conservation of mass, a weighted mass equation is added to the wave equation (the mass equation can also be viewed as a penalty term).

$$\begin{aligned} \frac{\partial^2 \eta}{\partial t^2} - \nabla \cdot [\nabla \cdot (H \mathbf{u} \mathbf{u}) + gH \nabla \eta + \mathbf{f} \times H \mathbf{u} \\ - F_w - \nu \nabla^2 \mathbf{u}] + \tau_0 \left[\frac{\partial \eta}{\partial t} + \nabla \cdot (H \mathbf{u}) \right] = 0 \end{aligned} \quad (2.36)$$

The rational for mixing two equations that should be satisfied independently is that equal-order FE methods are usually unstable, the same way that the non-staggered A-grid is usually unstable for FD methods. Hence, the model is stabilized using physical principles (the divergence of the momentum equations) at the price that the local mass balance is not necessarily satisfied. This may have some influence on the dynamics of oceanic flows.

The Peraire *et al.* (1986) Model

PZM developed an interesting model using equal-order interpolation and a two step explicit time-integration. First, mean values are computed for each triangle centroid from fluxes at vertices and then values at vertices are computed from flux computed at triangle centroids. This model is part of a broader family of Taylor-Galerkin formulations. We reproduce the demonstration about the Taylor-Galerkin formulation

of Priestley (1992). Starting from the following prognostic equation in a conservation form

$$\frac{\partial u}{\partial t} + \nabla \cdot \mathbf{F} = 0, \quad (2.37)$$

the idea is to increase the accuracy of the finite differencing of the time operator by use of a Taylor's series:

$$u^{n+1} = u^n + \Delta t \frac{\partial u^n}{\partial t} + \frac{1}{2} \Delta t^2 \frac{\partial^2 u^n}{\partial t^2} + \dots \quad (2.38)$$

By substituting the original equation (2.37) in the Taylor's series and truncating the series after the second order term yields

$$u^{n+1} = u^n - \Delta t \nabla \cdot \mathbf{F}^n + \frac{1}{2} \Delta t^2 \nabla \cdot \left[\frac{\partial \mathbf{F}^n}{\partial u} \nabla \cdot \mathbf{F}^n \right]. \quad (2.39)$$

The Galerkin formulation of this equation in a weak form is

$$\begin{aligned} \langle u^{n+1} - u^n, \phi_i \rangle = -\Delta t \langle \nabla \cdot \mathbf{F}^n, \phi_i \rangle \\ - \frac{\Delta t^2}{2} \left[\left\langle \frac{\partial \mathbf{F}^n}{\partial u} \nabla \cdot \mathbf{F}^n, \nabla \phi_i \right\rangle \right. \\ \left. + \int_{bd} \nabla \cdot \mathbf{F}^n \frac{\partial \mathbf{F}^n}{\partial u} \cdot \mathbf{n} \phi_i dl \right] \end{aligned} \quad (2.40)$$

where u and F are discretized using the piecewise linear basis functions. The difficulty at this stage is to express $\partial F / \partial u$. One way found by PZM was to approximate $\partial F / \partial u$ by a piecewise constant function and to express the one-step time integration as a two step time integration. Thus, if we first integrate forward in time over half a time step

$$\langle u_e^{n+1/2}, \phi_e \rangle = \langle u^n, \phi_e \rangle - \frac{\Delta t}{2} \langle \nabla \cdot \mathbf{F}^n, \phi_e \rangle, \quad (2.41)$$

where ϕ_e is the piecewise constant basis function (one over one triangle and zero over the rest of the domain; the variables with the underscript e are approximated using these basis functions). The Taylor development of $\mathbf{F}^{n+1/2}$ at first order

$$\mathbf{F}^{n+1/2} \sim \mathbf{F}^n - \frac{1}{2} \Delta t \left(\frac{\partial \mathbf{F}}{\partial u} \nabla \cdot \mathbf{F} \right)^n \quad (2.42)$$

leads to the approximation

$$\left(\frac{\partial \mathbf{F}}{\partial u} \nabla \cdot \mathbf{F} \right)^n = \frac{-(\mathbf{F}^{n+1/2} - \mathbf{F}^n)}{\frac{\Delta t}{2}}. \quad (2.43)$$

Since the term on the left hand side is approximated using piecewise constant basis functions, (2.41) becomes

$$\begin{aligned} \langle u^{n+1} - u^n, \phi_i \rangle &= \Delta t \\ &\left[\langle -\nabla \cdot \mathbf{F}^n, \phi_i \rangle + \langle \mathbf{F}_e^{n+1/2} - \mathbf{F}_e^n, \nabla \phi_i \rangle \right. \\ &\quad \left. - \int_{bd} (\mathbf{F}_e^{n+1/2} - \mathbf{F}_e^n) \cdot \mathbf{n} \phi_i dl \right]. \end{aligned} \quad (2.44)$$

In fact, we can integrate by part the first term on the right hand side in order to further simplify the equation

$$\begin{aligned} \langle u^{n+1} - u^n, \phi_i \rangle &= \Delta t \\ &\left[\langle \mathbf{F}_e^{n+1/2} - \mathbf{F}_e^n + \mathbf{F}^n, \nabla \phi_i \rangle \right. \\ &\quad \left. - \int_{bd} (\mathbf{F}_e^{n+1/2} - \mathbf{F}_e^n + \mathbf{F}^n) \cdot \mathbf{n} \phi_i dl \right]. \end{aligned} \quad (2.45)$$

Because of the use of linear basis function the first product in this equation can be further simplified to

$$\begin{aligned} \langle u^{n+1} - u^n, \phi_i \rangle &= \Delta t \\ &\left[\langle \mathbf{F}_e^{n+1/2}, \nabla \phi_i \rangle \right. \\ &\quad \left. - \int_{bd} (\mathbf{F}_e^{n+1/2} - \mathbf{F}_e^n + \mathbf{F}^n) \cdot \mathbf{n} \phi_i dl \right]. \end{aligned} \quad (2.46)$$

This method presents some similarities with the Lax-Wendroff scheme. It is second order for smooth problems but might be over-dissipative at shocks. For purely advective problems, PZM found that this formulation behaves very well and we found that it outperforms the Quoddy model (not shown).

The Hua and Thomasset (1984) Model

Hua and Thomasset (1984) developed a finite element model staggered in space, using discontinuous linear non conforming (P_1^{NC}) basis functions for the velocity (Fig. 2.8) and the usual linear basis functions (P_1) for the pressure. This formulation leads to a diagonal mass matrix for velocity, which leads

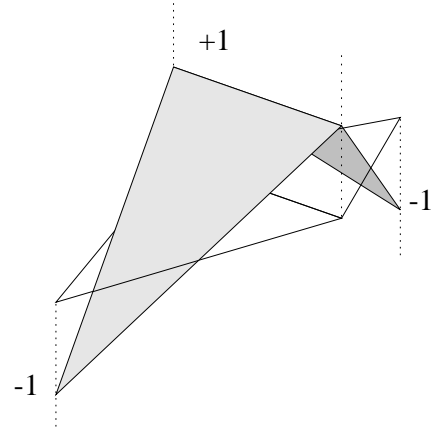


Figure 2.8: The discontinuous linear non conforming basis function for the $P_1^{NC} - P_1$ element of Hua and Thomasset (1984) associated with each face. The basis function takes the value of 1 over the face and -1 at the opposite vertices.

to a simplified matrix problem to solve for the elevation when semi-implicitly discretizing in time. They claim the model to be oscillation-free, although LLS demonstrated that the Hua and Thomasset model does not satisfy the LBB condition of stability for the Stokes flow problem. In the shallow water context, it shows some signs of instability (not shown). After some tests, we chose to integrate the equations explicitly in time using a Runge-Kutta integration technique instead of the semi-implicit technique proposed by Hua and Thomasset because the instability problem was then less severe.

The Le Roux *et al.* (2000) Model

LLS proposed to use a semi-implicit semi-Lagrangian time integration along with a spatial FE discretization that satisfies the LBB stability condition. The particularity of their choice for the basis functions resides in using macro-elements. Each macro-elements is cut into four sub-triangular elements. The basis functions for the velocity are linear inside each sub-triangle and the basis functions for the pressure (or elevation) are constant (see Fig. 2.9). The equation for the elevation

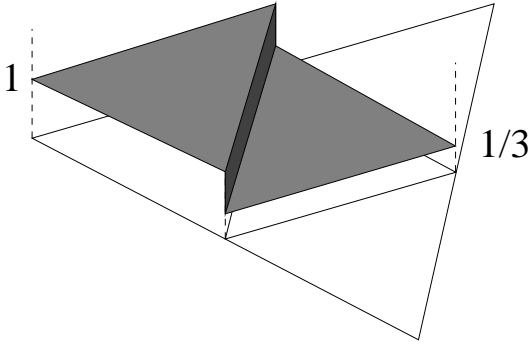


Figure 2.9: The discontinuous constant basis function for pressure over the macro-element of LLS. The macro-element is cut into four sub-triangular elements. There are three pressure basis functions over one macro-element, one for each exterior sub-triangle. They take the value of one over the exterior sub-triangle and $1/3$ over the interior triangle.

can be inverted locally. Hence, the solution of the coupled system of shallow water equations can be reduced to solving Helmholtz-like coupled equations for the velocity components. In order to interpolate the variables at the previous time step on an unstructured mesh, they also proposed a high order kriging method (see Trochu, 1993, for a review). Using this interpolation technique, they found that the model was performing very well for the purely advective problem. However, the application to a finite element shallow water model was somewhat disappointing. The high order method destabilizes the model (personal com.). Therefore, a low order kriging method had to be used, leading to potentially high artificial viscosity. The mass was not conserved, forcing LLS to add a mass corrector. Another disadvantage of the LLS formulation is the fact that the elevation basis functions are piecewise constant. This means that the truncation order of the model for the elevation is lower than that for the velocity and might lower the order of the velocity as well, since the equations for velocities and elevation are coupled in the shallow water equations.

2.4 The Discontinuous Spectral Element Method

2.4.1 Introduction

The first development of the spectral element (SE) method occurred in the early eighties (Patera, 1984). The SE method allows for irregular geometries and high accuracy because of varying order polynomials inside quadrangles or triangles that form the mesh. The main distinction between the FE and SE methods stems from the type of basis functions used to approximate the model equations. In FE methods, the basis functions are usually constructed for one specific order of the scheme (they are derived from Lagrange interpolators on regular grids inside each element). They need to be recomputed as the order of the FE method is modified. In SE methods, the basis functions are hierarchical and follow easier rules of construction (for instance, they can be derived from Chebyshev or Legendre polynomials). As the order is augmented, the former set of basis functions is simply augmented by a new set of polynomials constructed from the previous set. Therefore, in SE methods, the order of approximation is user-dependent and can even vary from element to element. There seem to be numerical advantages in terms of matrix inversion in using the Chebyshev or Legendre polynomials instead of regularly spaced Lagrange interpolators. The latter lead to poorer conditioned matrices as the order of the scheme is augmented (Le Provost and Vincent, 1986). As with the spectral method, the accuracy of SE method is exponential with increasing polynomial order. However, the SE method offers much higher flexibility in terms of geometrical representation. And, contrary to the spectral method for which Gibbs oscillations are prone to occur in under-resolved regions, in the SE method, one can easily increase the polynomial order (p -refinement) or the number of elements (h -refinement) in the underresolved regions. Using a polynomial order greater than two, we can also expect that SE methods are more accurate than conventional FD or FE methods, and that the convergence of the solution with increasing resolution is much faster.

We noted two applications in ocean modelling using quadrangular SE. The first by Ma (1993) and the second and more successful by Iskandarani and Haidvogel (1995). Using quadrangles, it is relatively easy to construct an orthogonal basis of cardinal functions which greatly facilitates the computation of nonlinear terms and renders trivial the matrix problem to be solved, provided the equations are prognostic and solved explicitly in time (leapfrog, Adams-Bashforth, Runge-Kutta). One limitation, however, of using continuous basis functions for the primitive (or shallow water) variables is that for stability the maximum polynomial order for approximating pressure (or elevation) has to be lowered, compared to velocity (Iskandarani and Haidvogel, 1995). Lowering the maximum polynomial order of one variable is similar to staggering the variables in space in finite difference methods and is also similar to satisfying the LBB condition for finite element methods (see previous section). On the other hand, the method leads to a large but sparse matrix problem if the equations are solved implicitly in time, or if a Helmholtz or Poisson-type of system has to be solved. The only disadvantage of using quadrangles compared to triangles comes from the difficulty of discretizing an irregular domain into quadrangles, the triangles offering more flexibility. Using triangles (Sherwin and Karniadakis, 1996), there is no orthogonal basis of cardinal functions. Therefore, a large matrix problem has to be solved at each time-step, even when the equations are discretized explicitly in time. Moreover, the computation of nonlinear terms requires a tedious transfer from the spectral coefficients to values at Gauss-like points, and back to the spectral space. However, in restricted applications, recent developments led to simpler and cheaper algorithms. Lomtev and Karniadakis (1999) (hereafter referred as LK) avoid the difficult problem of defining a set of continuous high order polynomials over triangles by reverting to a discontinuous formulation which leads to a local matrix problem in each element-triangle. This is only possible if all the equations are prognostic (as they are for shallow water models) and treated explicitly in time. Luckily, a hydrostatic Boussinesq ocean with a free-surface can be modeled using this simplified spectral element method. Furthermore, their model appears to be stable although the same set of basis functions is used for the velocity and pressure. Thus, their

method does not comply to the LBB condition. Finally, this method allows for an easy implementation of a time-variable mesh that we introduce in Section 2.4.3.

2.4.2 The Model Formulation

The matrix problem to be solved in each element is rather small for the order of the spectral element we choose to test (between 3 to 7). Therefore, the constraint of orthogonality over the set of polynomials for a cost-effective model is made less stringent. Thus, we introduced an even simpler set of basis functions compared to LK by simply using a set of products of Legendre polynomials with a triangular truncation.

$$\phi_i(\xi_1, \xi_2, t) = L_l(\xi_1)L_k(\xi_2), \quad l + k \leq n_c, \quad (2.47)$$

where n_c is the maximum order of the polynomials and i is indexed as l runs from 0 to n_c and k runs from 0 to $n_c - l$. The solution can be expressed inside the element j by

$$f(\xi_1, \xi_2, t)^j = \sum_i a_{ij}(t) \phi_i(\xi_1, \xi_2, t). \quad (2.48)$$

For the elements sharing a side with the boundary, the projection of the basis functions onto another set of basis functions which are always zero right at the boundary ensures the different possible boundary conditions (no-normal flow, free-slip, no-slip or inviscid)

$$\phi'_i = L_l(\xi_1)(L_k(\xi_2) \pm 1). \quad (2.49)$$

The projection method consists of computing coefficients in the new basis using the relation

$$\langle f', \phi' \rangle = \langle f, \phi \rangle \quad (2.50)$$

which satisfies a least square fit and where $f' = \sum_i a'_i \phi'_i$. Since the equations are expressed in terms of ϕ_i , the a'_i coefficients of ϕ'_i have to be expressed in terms a_i of ϕ_i . This is straightforward using (2.49). The different boundary conditions can also be implemented for elements sharing only one vertex with the wall. In a square domain, the convergence of the accuracy with resolution was seemingly good with the condition implemented for only elements sharing one side with the wall. Therefore, we only impose the

boundary conditions on elements sharing a face with the boundary although some tests were done to investigate this point. Furthermore, in opposition to the continuous spectral element formulations, we stress that the same polynomial order is used for all the variables. From our experience, we never encounter a problem related to the stability, except for trivial CFL problems.

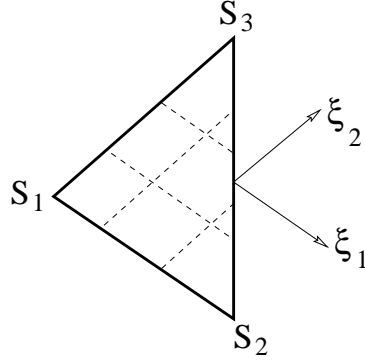


Figure 2.10: Local non-orthogonal coordinates in a given triangle

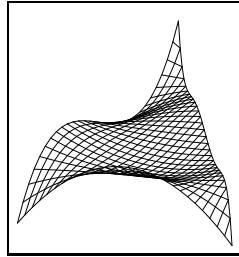


Figure 2.11: Example of Legendre polynomials $\Phi_i = L_2(\xi_1)L_3(\xi_2)$

We apply the discontinuous spectral element method to the discretization of the shallow water equations. Using a weak formulation and the traditional notation of Galerkin methods, inside each element-triangle the system of equations reads:

$$\begin{aligned} \left\langle \frac{\partial u}{\partial t}, \phi_i \right\rangle &= \left\langle \frac{\tau_x}{h}, \phi_i \right\rangle \\ &- \left\langle u \frac{\partial u}{\partial x} + v \frac{\partial u}{\partial y} - f v, \phi_i \right\rangle \\ &+ \left\langle g \eta, \frac{\partial \phi_i}{\partial x} \right\rangle - \oint g \eta_{bd} \phi_i n_x ds \\ &- \nu \left[\left\langle \nabla u, \nabla \phi_i \right\rangle - \oint \nabla u_{bd} \cdot \mathbf{n} \phi_i ds \right] \end{aligned} \quad (2.51)$$

$$\begin{aligned} \left\langle \frac{\partial v}{\partial t}, \phi_i \right\rangle &= \left\langle \frac{\tau_y}{h}, \phi_i \right\rangle \\ &- \left\langle u \frac{\partial v}{\partial x} + v \frac{\partial v}{\partial y} + f u, \phi_i \right\rangle \\ &+ \left\langle g \eta, \frac{\partial \phi_i}{\partial y} \right\rangle - \oint g \eta_{bd} \phi_i n_y ds \\ &- \nu \left[\left\langle \nabla v, \nabla \phi_i \right\rangle - \oint \nabla v_{bd} \cdot \mathbf{n} \phi_i ds \right] \end{aligned} \quad (2.52)$$

$$\begin{aligned} \left\langle \frac{\partial \eta}{\partial t}, \phi_i \right\rangle &= \left\langle \mathbf{u} h, \nabla \phi_i \right\rangle \\ &- \oint h_{bd} (\mathbf{u}_{bd} \cdot \mathbf{n}) \phi_i ds \end{aligned} \quad (2.53)$$

where variables and parameters are given in Table 2.1. The line-integrals are very important because they alone transfer information in and out of each element. LK chose to solve a local Riemann problem to compute the boundary value but this technique, being similar to an upwind method, leads to a loss of accuracy. We favored the simple choice of the mean value of both sides of a face which does not affect accuracy. The nonlinear terms are rather expensive to compute (30% of the cost at $n_c = 5$). They require a transformation of the local spectral coefficients to a local set of Gaussian points used afterwards to transfer back to the spectral space. The choice of the right Gaussian points is obviously important. After a few trials, we favor the use of irregular points on the triangle (Lyness and Jespersen, 1975; Dunavant, 1985), which are unfortunately only given for polynomials of degree up to 20 (the mass matrix can be exactly computed for $n_c \leq 10$). For higher degrees, it is always possible to use a regular set of Legendre-Gauss or Legendre-Lobatto points (but at a higher cost since these sets of points are not optimal on the triangle). For $n_c = 0$, we note that the discontinuous SE formulation is equivalent to a FV method.

The time integration is done using a 4th order Runge-Kutta method. Thus, using polynomials of degree $n_c = 5$ for instance, gives a certain equivalence between spatial and time truncation errors. The spectral element model is hereafter referred to as SPOC.

A constant eddy viscosity coefficient is used to allow for easy comparisons between models. In a discontinuous spectral element

model, the Laplacian operator of the velocity components cannot be computed directly (see LK for details). The computation has to be done in two steps. First, the gradient tensor of the velocity is computed using a weak formulation and an integration by parts. The mass matrix is then inverted:

$$\left\langle \frac{\partial u}{\partial x}, \phi_i \right\rangle = -\left\langle u, \frac{\partial \phi_i}{\partial x} \right\rangle + \oint u_{bd} \phi_i n_x ds. \quad (2.54)$$

Second, the gradient of gradient terms is computed in the momentum equations again using an integration by parts. This ensures that the gradient terms are (weakly) continuous between elements. Since the computation of the gradient tensor is necessary for the computation of the nonlinear terms, this treatment of the diffusion terms does not hamper the computational cost. In 2D, it involves the computation of 4 extra-terms, and in 3D, 9 terms. For the free-slip boundary condition (the one used hereafter), the normal velocity component and the normal derivative of the tangential velocity must vanish at the wall ($\xi_2 = -1$). This requires a rotation of the velocity components and of the gradient tensor and a projection onto the special basis function defined in (2.49).

2.4.3 Adaptive Mesh Refinement

Given the two to three orders of magnitude difference between the scale of eddies and the basin scale, today's global ocean eddy resolving models require a variable in time and space resolution. To fulfill this constraint, not only do we need a variable in space resolution model (which the FE and SE models already offer), but we also need some flexibility of the mesh in time, since eddies and fronts are unsteady phenomena. By adaptive mesh refinement, we mean that the mesh is refined automatically as the simulation goes on in regions where estimated errors are the largest. The difficulty is in computing an error estimator that determines where to put more resolution. For FE methods using linear basis functions, it is usually recommended to estimate the local second order derivatives of the fields and put more resolution where these derivatives are the largest (Zienkiewicz and Taylor, 1991, p.571). Because the solution is piecewise linear, it is difficult to estimate its second order

derivatives. This usually requires the reconstruction of the solution by a higher order method (Zhu and Zienkiewicz, 1990). For continuous SE methods, adaptive strategies require to estimate the slope of the spectral coefficients with wave number. If there is too much energy in the high wave numbers, the elements have to be refined (Mavriplis, 1994). This is a less complex procedure than that for FE methods. Adaptive strategies are difficult to implement in FD models because the Cartesian grids lack the flexibility of irregular meshes of FE and SE methods. Some adaptive mesh strategies have been proposed, though, in the form of nested grids. The coarse grid follows the overall circulation while the finer grid focuses on a particular region of interest. Both interacting in a one-way or two-way fashion depending on the models (Blayo and Debreu, 1999; Wadley and Bigg, 1999).

From the point of view of defining an error estimator, the discontinuous SE method is slightly more effective. Since the proposed SE formulation allows the solution to be discontinuous between elements, a straightforward estimator is to compute the maximum jump between elements for each field. Though very simple, this estimator has not yet been found in the literature. This is therefore our own development. Once the error estimator has been defined, the refinement or derefinement of the mesh is fairly conventional and can be found in many textbooks, for instance in Zienkiewicz and Taylor (1991) at p.574. We finally end up with four parameters that control the refinement in time (see Table 2.2). The refinement is hierarchical. When a triangle is to be refined, it is cut into four children-triangles and if the neighboring triangles are not to be refined, they are cut into two children-triangles in order to have a conformal connectivity. But if one of the two children-triangles is to be later refined, their parent-triangle will be cut into four, as the cutting into two children-triangles is only needed to complete the connectivity (Fig.2.12). All the refinements of the mesh will be kept in memory, easing the backward process of derefinement. The CFL condition is updated every time the mesh is modified. The model requires a certain adjustment time in order to smooth the jump between elements after each refinement of the mesh. Therefore there is a minimum value for n_{check} (Table 2.2) depending on

Parameters	Relative value	Function
λ_1	0.01-0.03	value of the jump above which the element is refined
λ_2	0.001	value of the jump below which the element is to be derefined
λ_3	0.05-0.15	value of the jump above which the simulation is restarted using older fields
n_{check}	1000	number of time step between two checks of the jumps between the elements

Table 2.2: Refinements parameters used in the simulations unless otherwise specified.

the time-step and the physical parameters. Hence, for a time stepping simulation, the model stops regularly to check the level of errors, refines the resolution accordingly, interpolates the fields onto the new mesh and then restarts with the new mesh and fields. In contrast to steady flows for which the solution is unique (if the initial guess is close enough), the transient simulations present the disadvantage that the solution accuracy might degrade because the errors are still present in the new fields, although the resolution has been improved. This justifies the use of λ_3 , the relative jump value above which the errors have reached an unacceptable level. If so, the model should not restart from the present time-step but from a previously saved time-step at which the level of errors was acceptable. The question of accuracy of adaptive time-stepping solutions also arises from the issue of interpolating the variable fields, since the interpolation does not conserve mass or energy.

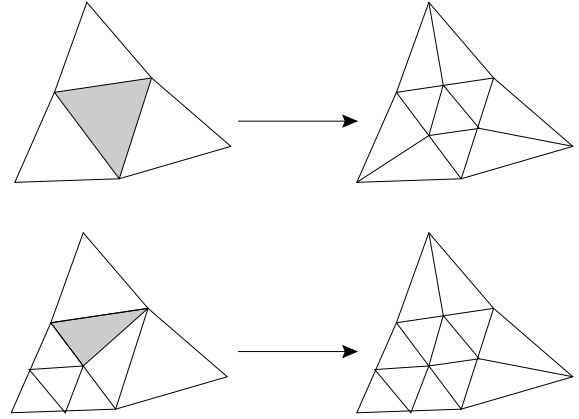


Figure 2.12: Remeshing strategies. The triangle to be refined is in grey.

2.4.4 Curved Spectral Element Method

As we stressed in Section 2.2, the representation of the irregular geometry is the weakest point of FD methods. They represent the coastline as step-like walls. This would be equivalent to say that the boundary is piecewise constant, i.e, discontinuous. In contrast, FE methods usually represent a complex boundary by piecewise linear segments. Thus, the model boundary is C^0 continuous. In order to represent accurately a complex boundary in SE formulations, it is better to stretch or curve the element boundaries than to increase the number of elements in a region of strong curvature (and keep the model boundary piecewise linear) as done in FE methods. Doing otherwise results in an increase in the number of elements and an increase in the resolution to the point that the cost of using higher order polynomials becomes prohibitive. It makes more sense to take advantage of the high order to get a boundary as smooth as possible (and try to get rid of discontinuities between piecewise segments along the boundary). This allows for faster convergence rates when the numerical solution is compared to analytical solutions found in continuously varying curvature domains. Furthermore, high order methods tend to behave badly in the presence of singularities along the boundaries (Gibbs oscillations). This is particularly true for this discontinuous SE method. In fact, we

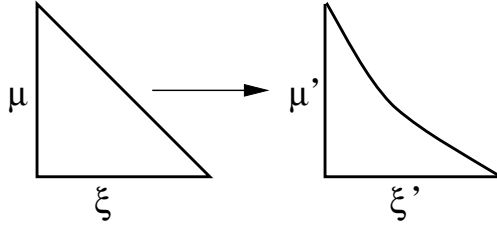


Figure 2.13: Transformation of one triangle into a curved triangle

observe in one test-experiment these oscillations localized around the tip of one rectangular continent. Hence, a clear limitation of this SE formulation lies in the presence of singularities along the coastline. It is not so much a surprise that the high order methods tends to behave badly in the presence of singularities compared with low order methods. Singularities excite the highest modes of the high order methods and so, lead to strong oscillations. In particular, the adaptive method developed in the previous chapter fails to convergence in the presence of singularities (not shown). Therefore, the solution may come from smoothing out the geometry by using curved elements. In practice, the additional cost associated with the implementation of curved elements in triangular spectral elements limits the order of continuity of the model boundary. This section is devoted to the development of a curved spectral element model. Although curved spectral elements may appear natural, few details are available in the literature about their implementation. We therefore develop our own methodology.

For a triangle with local coordinates varying in $0 < \xi < 1$, $0 < \mu, 1 - \xi$, there is a local analytical transformation that transforms one of the faces into a parabolic segment (Fig. 2.13):

$$\begin{cases} \xi' = \xi + a\xi\mu \\ \mu' = \mu + b\xi\mu \end{cases} \quad (2.55)$$

The segment is parabolic in the sense that it can be represented by an equation which is quadratic in term of ξ' and μ' . Hence, we can represent curved coastlines as piecewise parabolic segments. Since the coordinate system we choose for integration over

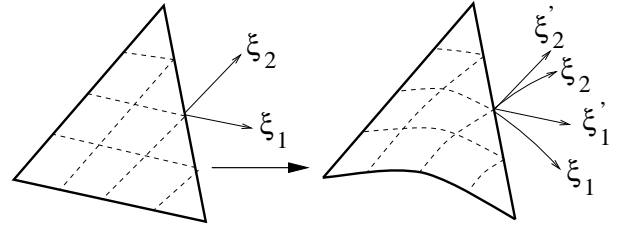


Figure 2.14: Transformation of one triangle into a curved triangle with the coordinate system used in the computation of the integrals

the triangle (Fig. 2.14) is (ξ_1, ξ_2) , the exact transformation is

$$\begin{cases} \xi_1' = \xi_1 - \frac{b}{2}(\xi_1^2 + \xi_1 + \xi_1\xi_2 + \xi_2) \\ \xi_2' = \xi_2 + \frac{a+b}{2}(\xi_1^2 + \xi_1 + \xi_1\xi_2 + \xi_2) \end{cases} \quad (2.56)$$

The Jacobian matrix \mathbf{J} of this transformation is needed for computing the integrals

$$\mathbf{J} = \begin{pmatrix} J_{11} & J_{12} \\ J_{21} & J_{22} \end{pmatrix}$$

with

$$\begin{cases} J_{11} = 1 - b(\xi_1 + 1/2 + 1/2 \xi_2) \\ J_{12} = -b/2(\xi_1 + 1) \\ J_{21} = (b+a)(\xi_1 + 1/2 + 1/2 \xi_2) \\ J_{22} = 1 + (b+a)/2(\xi_1 + 1) \end{cases} \quad (2.57)$$

For instance the computation of the mass matrix \mathbf{M} becomes

$$\begin{aligned} M_{ij} &= \int_T \phi_i(\xi_1, \xi_2) \phi_j(\xi_1, \xi_2) d\xi_1' d\xi_2' \\ &= \int_T \phi_i(\xi_1, \xi_2) \phi_j(\xi_1, \xi_2) \det(\mathbf{J}) d\xi_1 d\xi_2 \end{aligned} \quad (2.58)$$

The obvious inconvenience is that the Gaussian rules we use to compute the integrals and, more specifically, the nonlinear terms, need to be augmented by two degrees, since $\det(\mathbf{J})$ is a polynomial expression of degree 2. Therefore, a set of polynomials of degree 5 require a Gaussian rule of degree 12 instead of 10. Keeping the old set of Gaussian rule is not impossible but leads to large errors

since the integrals are not exactly evaluated. From that point of view, the spectral quadrangle is more efficient. Since it exists a set of cardinal-orthogonal polynomials on a rectangle, it is more effective to keep the old set of Gauss-Lobatto points even if the integrals are no more exact in a curved quadrangle. In fact, the errors in the computation of the integrals are, in this case, roughly of the order of the maximum polynomial order (Ronquist, 1980). However, for triangular spectral elements, the inconvenience of increasing the number of Gaussian points applies only for the curved elements along the boundary. Therefore, the problem of additional cost is not so serious since it concerns a small set of elements.

2.5 Summary

In summary, all numerical methods have their advantages and drawbacks. Traditional FD methods are of low order (usually, second order) and very easy to implement but may lack accuracy due to the presence of steps in irregular domains. FE methods discretize easily complex domains but are generally of low order and require the solution of a matrix problem. Moreover, they may lose one order in truncation errors if the mesh is too irregular (which often occurs for triangular meshes). By contrast, traditional implementations of FD methods in ocean models make use of regular grids. SE methods offer high accuracy in complex domains but at an unknown cost and seem to lose accuracy in presence of steps. Therefore, they require the smoothly curved boundaries that we introduce in Section 2.4.4. We also introduce a simple adaptive mesh strategy for the SE method. The mesh is refined or derefined when the local error is too large. The local error is estimated based on the jump in the solution between two adjacent elements. Hence, the SE model should be able to automatically increase the resolution in regions where the solution is under-resolved. This might be essential in order to resolve and follow local eddies or moving fronts. The next step is to investigate the effective truncation order and the cost function for all the models presented in this chapter.

Chapter 3

Testing the Different Numerical Methods

In this chapter we investigate the accuracy of the different models presented in Chapter 2, in straight wall and circular geometries. The test cases are idealized in the sense that they are based on the linearized shallow water equations and therefore, an analytical solution exists. We are interested in the effective truncation order and the computational cost for all schemes. These considerations are important for the choice of a numerical method to use in ocean modelling. Although this approach is very basic, we stress the fact that these comparative studies are rarely done and that little is known about the relative effectiveness and cost of each scheme. For the finite difference (FD) models in a circular geometry, we are particularly interested in the influence of the steps for a wind-driven circulation that occurs along the walls when the discretization axes do not coincide with the orientation of the walls. These steps may have a detrimental effect on the overall effective truncation order. In contrast, finite element (FE) and spectral element (SE) models have much less difficulty in discretizing complex boundaries. However, the use of irregular grids may decrease the effective truncation order of these models. We perform a convergence-with-resolution study for a non-linear problem in a square domain. In this case, the reference solution is given by the high-order spectral element (SE) method at a high resolution. For this problem, we also present results using the simple adaptive strategy introduced in the previous chapter for the discontinuous SE method. When a dynamical boundary condition has to be found, we tend to focus on slip boundary conditions. Otherwise, the fluid is assumed to be inviscid.

For circular or smooth geometries it is possible to use curvilinear grids for FD methods and, hence, avoid the occurrence of steps along the boundaries. Curvilinear grids can better fit irregular coastlines and can provide some variable resolution capabilities, such as implemented in the POM (Blumberg and Herring, 1987) and SPEM (Song and Haidvogel, 1994) models. However, some smoothing of the geometry is needed, since curvilinear grids cannot accommodate all bays and capes. This method is therefore of limited use, since it accommodates only the large scale features of the coastline. For a realistic representation of lateral boundaries, step-like features would still appear, although the total number of steps is reduced when compared to Cartesian grids. We do not consider the use of curvilinear grids in our discussion of FD methods due to its lack of generality, although this method might be adequate for smoothly varying boundaries.

3.1 Gravity Waves in a Square Domain

In this section, we present results for the linearized SW gravity wave propagation problem in a square domain. An elevation perturbation is imposed at the beginning of the simulation, in the form of a sine wave with phase lines parallel to the y -axis:

$$\eta(x, y, t = 0) = h_0 \cos(2\pi x/L_x) . \quad (3.1)$$

The initial velocity is zero. The wave propagates along the x -axis. Since there is no dis-

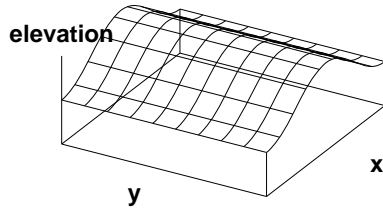


Figure 3.1: The wave test experiment

persion in the y -direction, the problem simplifies to a one-dimensional problem and a simple analytical solution can be found. An equation for η only can be found by substituting the u -equation in the η -equation

$$\partial_{tt}\eta - gH \partial_{xx}\eta = 0. \quad (3.2)$$

With no normal flow boundary conditions, the solution is

$$\eta(x, y, t) = h_0 \cos\left(\frac{2\pi x}{L_x}\right) \cos(\omega t) \quad (3.3)$$

where $\omega = \sqrt{gH} 2\pi/L_x$. Therefore, the wave is a free mode of oscillation for the square basin. It bounces back and forth between the walls at the period of $2\pi/\omega$. The velocities are given by

$$\begin{cases} u(x, y, t) = u_0 \sin\left(\frac{2\pi x}{L_x}\right) \sin(\omega t) \\ v(x, y, t) = 0 \end{cases} \quad (3.4)$$

where $u_0 = gh_0/\sqrt{gH}$.

For all models, the numerical simulation is performed up to a tenth of the characteristic period of the wave. This duration is long enough that the estimation of the effective truncation order for the different models is possible and yet not too long so that the contamination by other factors such as time discretization errors is limited. The Courant number is kept constant and is the same for all models. By increasing the resolution of the models and comparing the numerical solution to the analytical solution, we can compute the errors and the effective truncation order of each scheme. For the FD models, the grid is oriented along the walls of the square which coincide with the direction of the wave propagation, also the x -axis. Hence, there

are no dispersion errors in the y -direction. However, the FE and SE methods use irregular meshes made of triangles that are randomly oriented. Therefore, these methods show a dispersion error along the y -axis which can be quantified as a function of resolution. The errors are computed and normalized as

$$E(\mu_{mod}) = \frac{\int \int |\mu_{mod} - \mu| dx dy}{\int \int dx dy} \cdot \sqrt{\frac{\int \int dx dy}{\int \int \mu^2 dx dy}} \quad (3.5)$$

where μ and μ_{mod} represent respectively the analytical and model solution of any variable. The term $\int \int \mu^2 dx dy$ is computed analytically and is therefore the same for all models. For FD models, $\int \int |\mu_{mod} - \mu| dx dy / \int \int dx dy$ is approximated by $\sum_{ij} |\mu_{mod} - \mu| / (n_x n_y)$. For the FE and SE models, this integral is computed by interpolating $|\mu_{mod} - \mu|$ onto a regular grid, summing the values and dividing by the number of sampling points. We increase the number of sampling points until a convergence criterion is satisfied. The normalized error for u is obtained from (3.5) by direct replacement of μ by u . For v , this is not possible as its analytical value is zero. We have thus used the analytical value of u for $\int \int \mu^2 dx dy$. The choice of norms in (3.5) in determining the normalized error is somewhat arbitrary and other norms can be used. However the results would not be substantially different.

We first compare the accuracy of the linearized version of the 4th order A-grid model to that of the second order C-grid formulation (Figure 3.2). On this log-log plot, the slope of the curve is directly related to the order of the convergence. The C-grid scheme is very close to second order and the original A-grid model (as proposed by D93 and referred as O-FDM4) has a convergence order of close to 4. However, the errors can be reduced by a factor of six if the 4th order accuracy is extended up to the boundary (R-FDM4 version). The gradient and interpolation operators then need to be off-centered for points located less than two points away from the walls. In terms of cost, the A-grid model is very advantageous (see Fig 3.3 where only results from R-FDM4 is plotted). The extra points in the computation of the gradi-

ent operators needed for 4th order accuracy slow the model only slightly. Therefore the 4th order A-grid is cost-effective compared to the C-grid for this problem.

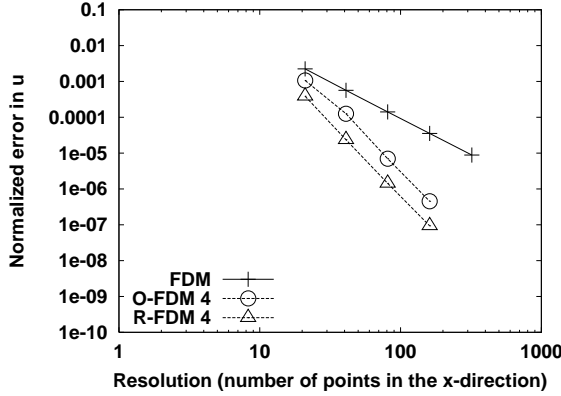


Figure 3.2: Convergence with resolution of the normalized error in the u -component for second order C-grid formulation (FDM), O-FDM 4 and R-FDM 4 models. The R-FDM4 is an A-grid formulation with off-centered operators to incorporate the 4th order accuracy up to the boundary

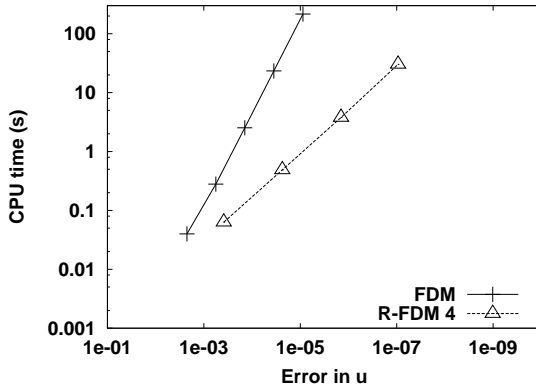


Figure 3.3: CPU cost with the normalized error in u -component for the second order C-grid (FDM) and R-FDM4 models.

For FE models, the use of irregular grids cause errors in the v -component, perpendicular to the propagation direction. These errors can also be viewed as a dispersion error. One way to minimize this error would be to design meshes for which the nodes or vertices are aligned with the propagation axis (i.e. characteristic meth-

ods). Such a mesh would therefore be application dependent. We focus instead on the use of irregular meshes in which the triangles are randomly oriented since, in general ocean modelling, there are no preferential directions of propagation. We examine the four FE models introduced in Section 2.3: the Lynch and Werner (1987; 1991) model, the Hua and Thomasset (1984) model, the Peraire *et al.* (1986) model and the Le Roux *et al.* (2000) model. The respective abbreviations are: LW, HT, PZM and LLS. In our comparison study, we multiply by two the actual resolution of the mesh for the LLS model to take into account the fact that this model implicitly doubles the resolution by dividing each triangle into four sub-triangles. Figure 3.4 shows the convergence with resolution of the errors for the v - and u -components for a linearized version of all FE models. In such a case, the LLS model is plainly Eulerian instead of semi-Lagrangian. The errors are generally larger for the FE models compared to the C-grid FD model, except for the LLS model where the errors are comparable. This is notably due to the use of unstructured grids in FE models.

Table 3.1 gives the value of the convergence order for both components of the velocities for all models. The order is usually lower for the v -component (closer to first order) than that of the u -component (closer to second order) for all FE models. This is however an artefact due to studying the two components of the velocity separately. The error in v is usually smaller than the error in u . This allows for some noise contamination to lower the convergence order for v compared to that for u . The convergence order for the velocity vector tends to be in between but closer to the convergence order for u since the errors are largest for this component.

The equal-order FE models (LW and PZM) present the best convergence order for u (about 2) and also the poorest order for v (about 1). The LLS model presents the largest order for v . The order for the HT model is closer to first than second order for both components of velocity. Theoretically, the best achievable convergence order for the FE models under consideration is second order. The fact that the convergence order for most models is less than but close to 2 for u is due to the use of irregular meshes. The change, though, is not as dramatic as

predicted in Section 2.3.2 where we predict first order convergence in presence of irregular meshes for second order accurate FE formulations.

Since the LLS model is the best FE model in terms of the magnitude of the errors — to the point that the magnitude compares favorably to that of the C-grid errors— it is worth considering some of the reasons behind this result. First, the method uses macro elements sub-divided into four elements and this may “regularize” the mesh since the four sub-triangles are identical in shape and area. Second, it is also possible that the fact that the coupled shallow water equations are reduced to coupled Helmholtz equations for the velocity improves the solution for the velocity. The fact that the order for this model is somewhat smaller compared to that of the LW and the PZM models for the u -component might be a sign that the truncation order for the pressure slightly affects the truncation order for the velocity. This will be more evident in the next test-case. For the HT model, the smaller convergence order is probably related to the use of discontinuous basis functions for the velocities, in contrast to continuous basis functions used in the other FE models. In conclusion, for this linear problem, all FE models perform relatively well —except for the HT model.

We now compare the results of one FD model (C-grid) and one FE model (LW) to the discontinuous SE model (Fig 3.5 and 3.6). To make results comparable, the SE resolution (the inverse of the mean length of triangle sides) is multiplied by the maximum polynomial order. The LW-FE errors are generally larger than those of the FD and SE models. The SE model has a convergence order that varies between n_c and $n_c - 1$ depending on the velocity components. If the basis functions were continuous, the best achievable convergence order would be $n_c + 1$. The loss of more than one order is probably related to the use of unstructured meshes and the fact that the basis functions are discontinuous between elements. At $n_c = 3$, the accuracy of the SE model is slightly better than the FD model. At the same resolution, the higher-order method is always more accurate ($n_c = 5$ and 7). Finally we noted that as for the FE models, the SE model shows a difference (Table 3.1) in the convergence order for v and u , with the order for v being

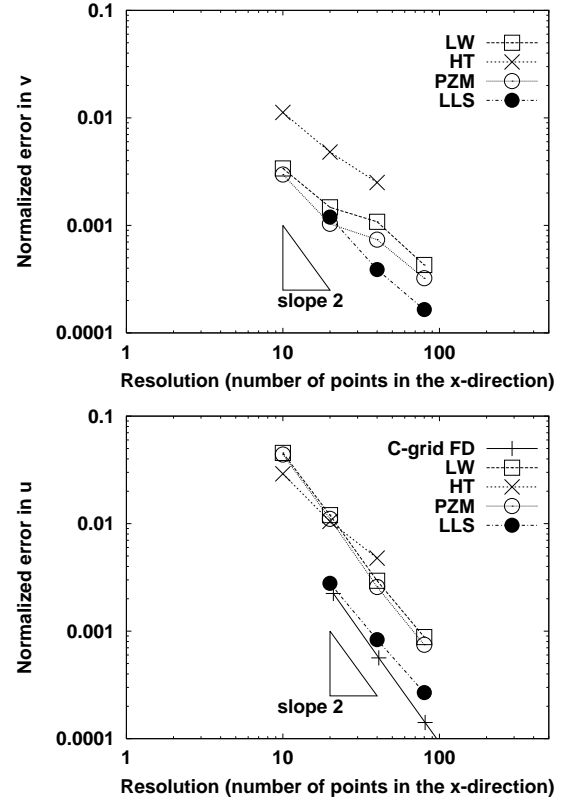


Figure 3.4: The four FE models (LW, HT, PZM, LLS) are tested against the analytical solution with increasing resolution. On top is the normalized error for the v -component; at the bottom is the normalized error for the u -component. The error for the u -component of the C-grid FD model is plotted for comparison.

smaller than that for u . This is related to the use of irregular grids and noise contamination problems.

Figure 3.7 shows the variation of the CPU cost with respect to the accuracy for the C-grid FD model and one A-grid FD (R-FDM4) model, the LW and LLS FE models and the discontinuous SE model. The curve is usually a straight line. The less the slope of the curve, the more accurate for the same cost one model is. The model whose curves lies on the right (left) of the others is the most (less) economic model. There is of course the possibility that some models perform better than the others depending on the range of the required accuracy due to the existence of cross-over points between the different curves. The LW model is always less accurate for the same cost with the slope being equivalent to that of the finite difference model. The LLS model enhanced accuracy compared to the other FE models (Fig. 3.4) is traded off by a large increase of the CPU cost, to the point that the LLS model is only marginally better than the LW model. The SE model with $n_c = 5$ behaves similarly to the 4th order A-grid model. However, the A-grid model is slightly more accurate for the same cost. Nonetheless, the SE model with $n_c = 7$ give better results than this 4th order FD model. From this linear test case, we conclude that it is more effective to use higher order methods (the SE and R-FDM4 models).

3.2 The Wind-driven Circulation in a Circular Domain

A linear analytical solution can be found for the wind-driven problem in a circular domain with Coriolis forces and damped by a linear bottom friction. No viscosity is included. The boundary condition is simply the no-normal flow condition at the model boundary. The steady state linearized shallow water equations in cylindrical coordinates for

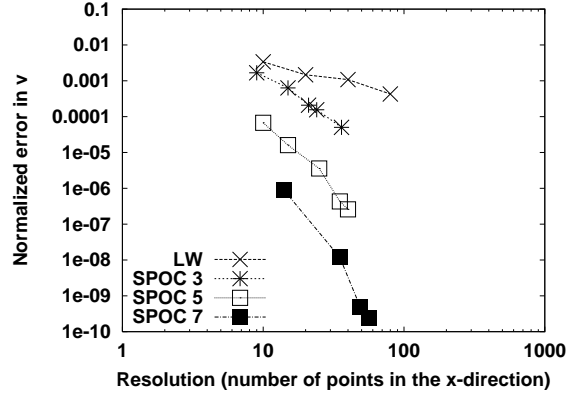


Figure 3.5: Convergence of the normalized error in v with respect to the resolution for the LW-FE and SE models. SPOC3,5,7 corresponds to the SE model with $nc = 3, 5, 7$

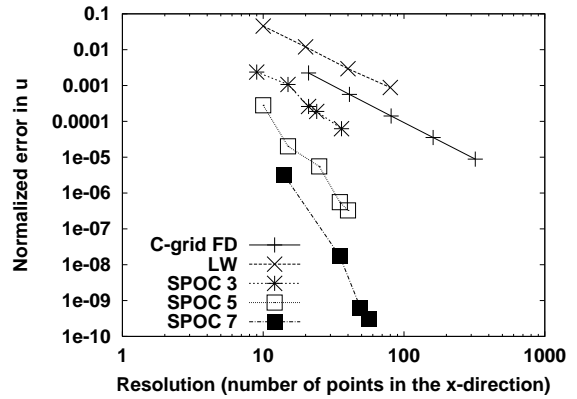


Figure 3.6: Convergence of the normalized error in u with respect to the resolution for the C-grid FD, LW-FE and SE models. SPOC3,5,7 corresponds to the SE model with $nc = 3, 5, 7$

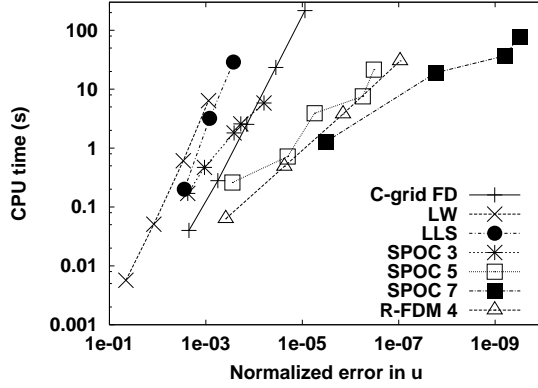


Figure 3.7: Variation in the u -component normalized error as a function of CPU cost. The former is measured by the area integrated absolute value difference between the numerical and analytical model results for the C-grid FD, R-FDM4, LW, LLS and SE models. SPOC3,5,7 corresponds to the SE model with $nc = 3, 5, 7$

Model	convergence order for the error in v	convergence order for the error in u
C-grid FD	—	2.03
O-FDM 4	—	3.85
R-FDM 4	—	4.09
LW	0.94	1.91
HT	1.08	1.30
LLS	1.43	1.69
PZM	1.01	1.97
SPOC 3	2.57	2.73
SPOC 5	4.00	4.68
SPOC 7	5.96	6.72

Table 3.1: Convergence order for the different models for the linear wave experiment in a square domain. For all models, the order is fairly close to their theoretical value. Models using unstructured grids lost almost an order for the error in v compared to the error in u .

this problem are

$$g \frac{\partial \eta}{\partial r} = -\kappa v_r + \tau_x / H \cos \theta + f v_\theta \quad (3.6)$$

$$\frac{g}{r} \frac{\partial \eta}{\partial \theta} = -\kappa v_\theta - \tau_x / H \sin \theta - f v_r \quad (3.7)$$

$$\frac{\partial(r v_r)}{\partial r} + \frac{\partial(v_\theta)}{\partial \theta} = 0 \quad (3.8)$$

where the wind forcing is given in cylindrical coordinates by the relationship

$$\tau_x = \frac{W y}{R} = \frac{W r \sin \theta}{R} . \quad (3.9)$$

where R is the radius of the circular domain. From (3.6-3.8), we derive an equation for η

$$r \frac{\partial^2 \eta}{\partial r^2} + \frac{\partial \eta}{\partial r} + \frac{1}{r} \frac{\partial^2 \eta}{\partial \theta^2} = -r \frac{W f}{R g H \kappa} \quad (3.10)$$

with the boundary condition of no-normal flow

$$\kappa \frac{\partial \eta}{\partial r} + \frac{f}{r} \frac{\partial \eta}{\partial \theta} = \frac{\tau_x f}{g H} (\kappa \cos \theta - f \sin \theta) \text{ at } r = R . \quad (3.11)$$

This leads to the solution without Coriolis force,

$$\eta = \frac{W r^2}{4 g H R} \sin 2\theta \quad (3.12)$$

and with Coriolis force

$$\eta = \frac{W f}{R g H \kappa} \left[\frac{R^2}{8} + \frac{r^2}{4} \left(\frac{\kappa}{f} \sin 2\theta - 1 \right) \right] . \quad (3.13)$$

With or without the Coriolis terms, the velocity components take the simple form of

$$\begin{cases} v_r = 0 \\ v_\theta = -\frac{W r}{2 R \kappa} \end{cases} \quad (3.14)$$

which translate in the Cartesian coordinate system to

$$\begin{cases} u = \frac{W}{2 R \kappa} y \\ v = -\frac{W}{2 R \kappa} x . \end{cases} \quad (3.15)$$

We perform a one year spin-up for all models with $W = 10^{-4} \text{m}^2 \text{s}^{-2}$, $f = 10^{-4} \text{s}^{-1}$ or zero

and $\kappa = 10^{-3}\text{s}^{-1}$. This is enough to converge to a steady state accurate at six digits for the kinetic energy. The normalized error is computed in the same manner as in (3.5) but using the elevation field. We focus on the elevation this time because, for the HT and LLS FE models, the pressure basis functions are different from the basis functions used to represent the velocity. Furthermore, the previous test case does not allow for an interesting comparison of the elevation fields (the elevation is imposed at initial time), whereas this one does.

We first analyze the results from the C-grid model. Because of the presence of steps (Fig. 3.8), it is not clear which opposing effect is dominant when the resolution is increased: an increased accuracy in the interior and a more accurate representation of the boundary, or a lower accuracy because of the increased number of steps. For brevity, we only show the results for one case, at $f = 0$, since convergence properties are not significantly different than those at $f \neq 0$. Figure 3.9 shows the convergence of the normalized error in η with increasing resolution. It appears that the convergence order of the C-grid FD model is closer to one (1.1 when $f = 0$ and 1.3 when $f = 10^{-4}\text{s}^{-1}$) than two, the maximum for this second order FD formulation. Therefore, the steps have a direct influence on the order of the FD model. The order is reduced compared to the previous test-case with straight walls. The perturbation due to the singular steps on the flow does degrade the accuracy, although not to the point that the errors increases with increasing resolution.

We now compare the solution from the C-grid FD model with the O-FDM4 and R-FDM4 models. Figure 3.9 shows that the order of the A-grid model is actually less than two in presence of step-like walls. Furthermore, there is no longer a difference, in term of truncation order, between the second order C-grid and the 4th order A-grid models —unlike the case with straight walls. Therefore, the presence of steps along irregular boundaries has a detrimental effect on the accuracy of high order FD formulations if the flow is allowed to slip along the walls.

We now compare the FE models to the C-grid model. In this circular geometry, all FE

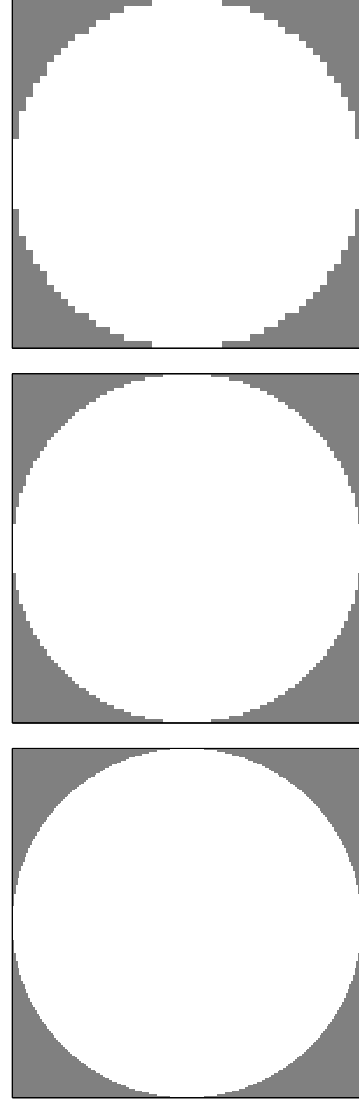


Figure 3.8: Grids for the circular domain for the FD models. 51×51 , 101×101 and 201×201 points for domain on the left, center and right respectively.

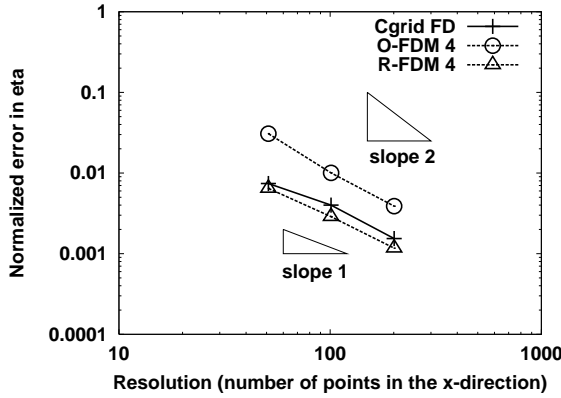


Figure 3.9: Convergence with resolution of the normalized elevation error for the second order C-grid FD, O-FDM4 and R-FDM4 models in a circular domain.

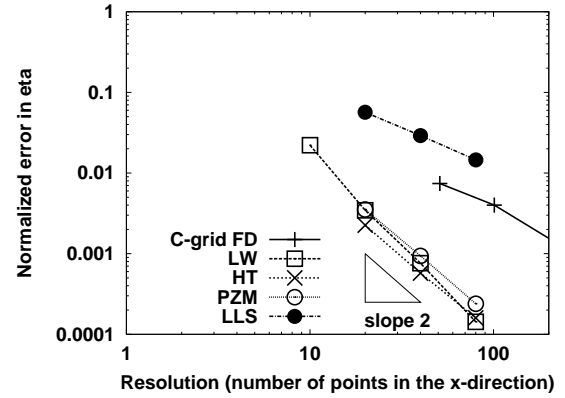


Figure 3.10: Normalized elevation error in a circular domain for an inviscid linear solution. The four FE models (LW, HT, PZM, LLS) are tested against the analytical solution with increasing resolution. The error for the FD model (FDM) is given for comparison.

models have the advantage that the representation of the boundary is improving as the resolution is increased. Therefore, it should be possible to observe convergence order close or even exceeding two. Figure 3.10 and Table 3.2 show that all FE models have a convergence rate close to second order except for the LLS model. The LLS model also shows the largest errors. The reasons for the poor performance of this model are as follows. Firstly, the geometry is resolved by the macro-elements. Thus the representation of the boundary suffers from being half sampled compared to the permitted resolution. Second, we focus here on the elevation errors which are always larger for the LLS model because the piecewise constant basis functions are not as accurate as those of the other models. For the HT model, the improvement in the error compared to the previous test-case is probably due to the basis function for η being continuous. In fact, all FE models used this basis function for the elevation except for the LLS model. Hence in terms of accuracy, all FE models appear to perform better than FD models in non-rectangular geometries for linear problems, except for the LLS model. In terms of cost, the equal-order FE models are the most effective. However, we still need to demonstrate the efficiency of FE models for nonlinear problems before concluding on the general effectiveness of FE models in irregular domains.

For the SE model, the results are given in Fig. 3.11 where we compare the solutions from the C-grid FD, LW FE and SE models. The results for the SE model shows a surprising feature. The 3rd order SE model has a better accuracy than the FE model but the errors for the 5th and 7th order SE are larger than expected. The convergence order is also affected (see Table 3.2). In this particular example, the main source of errors comes from the discretization of the circular geometry by piecewise parabolas. A quadratic spline description of the circular boundary allows for (at least) a 3rd convergence order. This explains why the convergence order for the 3rd order SE model appears optimal but less optimal for the 5th and 7th order SE model. The order of the solution improves in the interior but the error along the boundary being larger leads and causes a overall loss in the convergence order. One solution would be to implement more complex curved elements along the boundary (using cubic or more splines), but as explained in Section 2.4.4, increasing the order of the piecewise curves along the curved elements is not always practical.

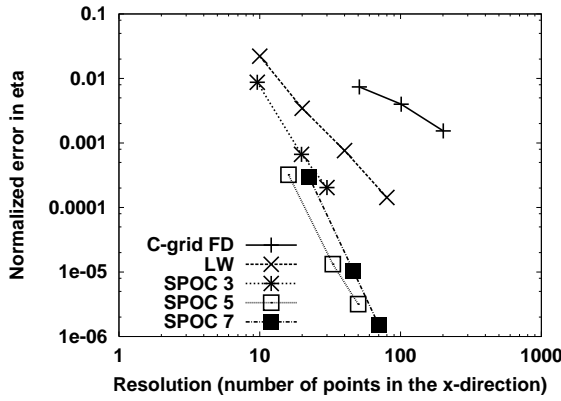


Figure 3.11: Normalized elevation error for the C-grid FD, LW-FE and SE models for a circular domain. The curve for the SE model at $n_c = 7$ (SPOC 7) is on the right of that for $n_c = 5$ (SPOC 5) presenting some kind of “saturation” effect.

Model	convergence order for the error in η
C-grid FD	1.15
O-FDM 4	1.51
R-FDM 4	1.24
LW	2.40
HT	1.91
LLS	0.98
PZM	1.94
SPOC 3	3.33
SPOC 5	4.09
SPOC 7	4.64

Table 3.2: Convergence order in elevation, for the different models for the linear wind-driven experiment in a circular domain without Coriolis terms.

3.3 Conservative Properties of the Different Numerical Formulations for a Nonlinear Problem

We compare the FE models and the discontinuous SE model to the solution given by the C-grid FD model in a test-case for which the total energy (kinetic and potential) is conserved during the time of the simulation. A geostrophically balanced eddy is initialized at the beginning of the simulation in a square domain on a beta plane approximation for all models. The shallow water equations are fully nonlinear. The fluid is inviscid, that is no eddy viscosity is applied and therefore no dynamical boundary condition is required. We introduce two versions of the LW model. The first one is the original model in which the mass matrix is lumped (see Section 2.3 for explanation) and is referred as lumped LW. The second version uses the delumped mass matrix (the full —sparse but not diagonal— mass matrix) and is referred as delumped LW. The SE model is run on a 132 triangle mesh at $n_c = 5$. The geostrophic eddy moves slowly westward due to the sphericity of the earth and slightly southward due to the nonlinear terms ($f_0 = 1.0285 \times 10^{-4} \text{ s}^{-1}$ and $\beta = 1.607 \times 10^{-11} \text{ m}^{-1}\text{s}^{-1}$). The initial height is 580 m and corresponds to a velocity maximum of 1 m/s currents for a reduced gravity of $g' = 0.01 \text{ m/s}^2$. There is no forcing and no dissipation, therefore the total energy should be conserved. Figure 3.12 shows the results. The FD and SE models do indeed conserve energy, but all the FE models tend to lose energy. The FE models that dissipate energy moderately are the delumped LW model, closely followed by the LLS model. The HT model becomes unstable after a few days of integration and results for this model are therefore not shown. This illustrates the severe stability problem suffered by this model. The results for the lumped and delumped LW model are shown for $\tau_0 = 2 \times 10^{-3} \text{ s}^{-1}$ (see Section 2.3 for details on τ_0). The lumped LW model appear to be more dissipative than the delumped version. We tested other values of τ_0 for the lumped and delumped LW models (the results are not shown). For smaller τ_0 both

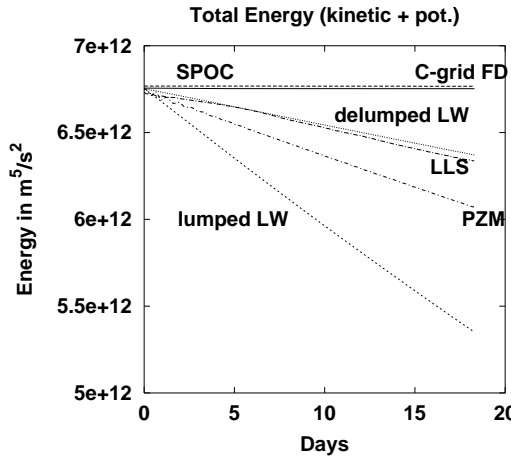


Figure 3.12: Total energy after 18 days of simulation for the C-grid FD and the lumped LW, delumped LW, PZM and LLS FE models and the SE model for the geostrophically balanced eddy with no dissipation and no forcing. All the FE models tend to be over-dissipative.

versions of the model tend to be even more dissipative and the lumped version is unstable when τ_0 is too large ($> 10^{-1} \text{ s}^{-1}$) or too small ($< 5 \times 10^{-5} \text{ s}^{-1}$). The influence of τ_0 on the dynamics will be further investigated in the next test case.

3.4 The Munk Problem in a Square Domain

In this section, we compare the models using a second nonlinear problem, namely the single gyre Munk problem. With a constant wind, the sphericity and rotation of the earth yield a strong return flow along the western wall. The wind forcing is given by the stress $\tau_x = -10^{-4} \sin(\pi y/L_y) \text{ m}^2\text{s}^{-2}$ and $\tau_y = 0$. The remaining model parameters are identical to those of the previous section. The energy put in the ocean by the winds is dissipated mainly in a viscous layer along the boundary because of the strong return flow there. The eddy-viscosity, $\nu = 700 \text{ m}^2\text{s}^{-1}$, is constant over the whole domain. We use the

free-slip boundary condition. A strong recirculation forms in the northwestern part of the domain, evidence of the nonlinear effects in the solution. Under free-slip, the solution is very sensitive to the shape of the boundaries and to the value of ν . We hope to shed some light on the sensitivity of the FD models to steps occurring along the boundaries, as FD models generally do not work well in irregular geometries. Furthermore, because of the sensitivity of the solution to ν , we expect to better observe the dissipative nature of FE models.

For the C-grid FD model, Adcroft and Marshall (1998), hereafter AM, performed the same test-case for somewhat different model parameters. An important finding in this study is that the C-grid model is very sensitive to the presence of steps, to the point that simulations run in a rotated square basin with respect to the grid yield very different results compared to the non-rotated simulation. This sensitivity could greatly be reduced if the conventional five-point Laplacian in the viscous tensor is replaced by a discretized vorticity-divergence form. The two tensor formulations are equivalent in a non-rotated basin, but are different in presence of steps. Around steps, the vorticity-divergence formulation tends to accelerate the fluid parcels compared to the conventional stress formulation. Their findings suggest that free-slip circulations can be made independent of the way the coastline is discretized. We shall return to this issue in the next chapter.

We consider the solution from the 4th order A-grid model. When running the nonlinear version of this model with free-slip boundary conditions, we noted that having 4th order accuracy extended up to the boundaries has some positive influence on the stability of the overall model. Figure 3.13 shows that large spurious numerical modes are present for O-FDM4, whereas there are no visible spurious modes for R-FDM4. We also consider the same experiment in a rotated basin with respect to the grid, following AM. Strong numerical noise again occurs for O-FDM4 (Fig. 3.14). The model remains however stable and relatively noise-free when the 4th order extends up to the walls, although the total kinetic energy is less than that for the non-rotated basin experiment. Moreover, the overall circulation looks very

similar to that observed by AM with the C-grid and conventional viscous stress tensor in rotated basins. The C-grid solutions tend to be less noisy, though. These two observations (numerical noise and lower energetic level) demonstrate that the 4th order formulation is very sensitive to the presence of steps when the free-slip boundary condition is used. We did not test whether the vorticity-divergence form of the stress tensor has the same positive influence for R-FDM4, as it does in the case of the C-grid. Chapter 4 will be specifically dedicated to a thorough study of the issue of FD discretizations and advective and stress tensor formulations in rotated basins.

We compare now the FE models to the solution given by the C-grid FD model for a non-rotated basin. All FE models tend to show a kinetic energy value well below the FD model during spin-up (Fig. 3.15). The circulation also proves to be weaker in magnitude for the FE models when compared to the FD model circulation (Fig. 3.16), showing the dissipative nature of FE models. We discuss some of the reason for this behavior. For the HT model, increasing the resolution did not improve the solution (not shown). There is therefore some sort of zero truncation order error in this model. This may arise from the discretization error of the nonlinear terms in the momentum equations due to the discontinuous linear form of the velocity basis functions. The PZM model may be dissipative because of the use of averaged values at triangle centroids in the computation of fluxes. The LLS is dissipative because of the dissipative nature of the low order Kriging method used in the time semi-Lagrangian discretization (see Section 2.3 for more details). We do not expect to see any improvement with increased resolution for this model because higher resolution means smaller time-steps, and therefore, a larger number of interpolation operations.

For the LW model, the mass equation is not solved independently for the elevation but is mixed with a wave equation (Eq. 2.36). In theory, both equations should be satisfied independently. However, since both equations are mixed together, neither is solved exactly and this may influence the overall oceanic circulation. The wave equation tends to transfer η , equivalent to the mass, through the whole domain by means of gravity waves.

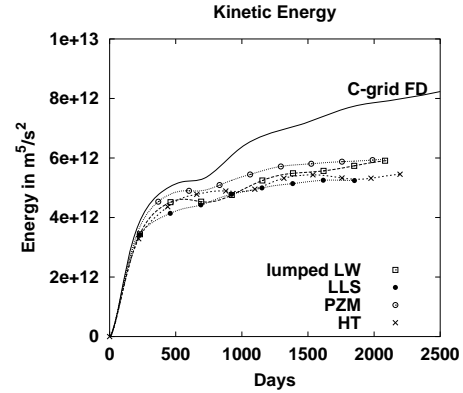


Figure 3.15: Kinetic energy during a 6 year spin-up for the C-grid FD, the lumped LW, HT, PZM and LLS FE models.

This process may upset the local geostrophic balance by transferring the mass through the streamlines. This process is equivalent to having a dissipation term in the mass equation. To illustrate this, we vary the value for τ_0 , the free parameter appearing in the wave-mass equation for the wind-driven single gyre Munk problem. Figure 3.17 shows that the kinetic energy for a single gyre wind forcing at the end of the simulation varies significantly with the value of τ_0 (not to be confused with the wind stress; see Section 2.3 for details). In the limit $\tau_0 \rightarrow \infty$, which corresponds to satisfying the local mass balance, the results are very similar to the ones obtained using the FD method. However, as we noted earlier the model can be unstable for large values of τ_0 for certain applications (Section 3.3). A good compromise is found by experimenting with different values of τ_0 and is therefore very application dependent.

For the discontinuous SE model, we consider the Munk problem for two values of the eddy-viscosity. We retained for comparison the C-grid FD model and the delumped LW FE model at $\tau_0 = 2 \times 10^{-3} \text{ s}^{-1}$, which gives better results than the lumped version. The SE model is run at $n_c = 5$ on a 56 triangle mesh. We compared results from the FD, SE and FE models for two values of the viscosity coefficient. For the high viscosity case ($\nu = 2000 \text{ m}^2 \text{ s}^{-1}$, Fig. 3.18) the models perform similarly, with the FE model showing smaller undershoots. The SE and FD

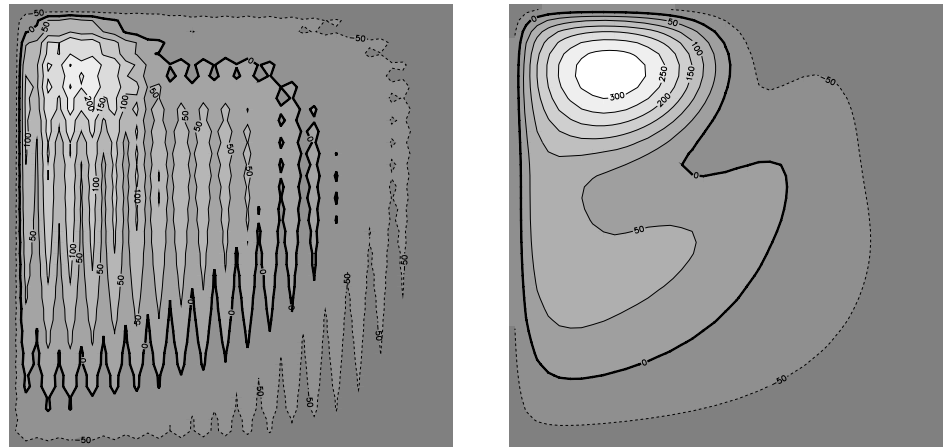


Figure 3.13: Elevation field after a six year simulation in a non-rotated basin using O-FDM4 (left panel) and R-FDM4 (right panel). The conventional Laplacian is used.

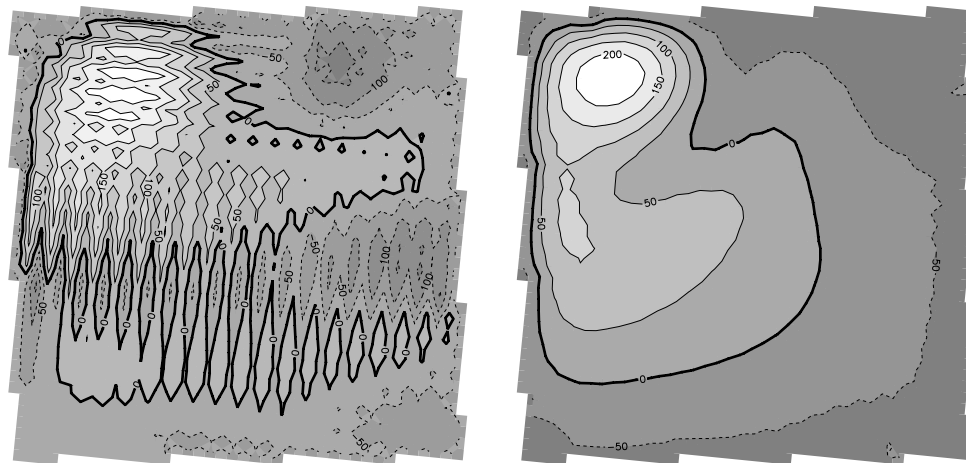


Figure 3.14: As for Figure 3.13 but for rotated basin.

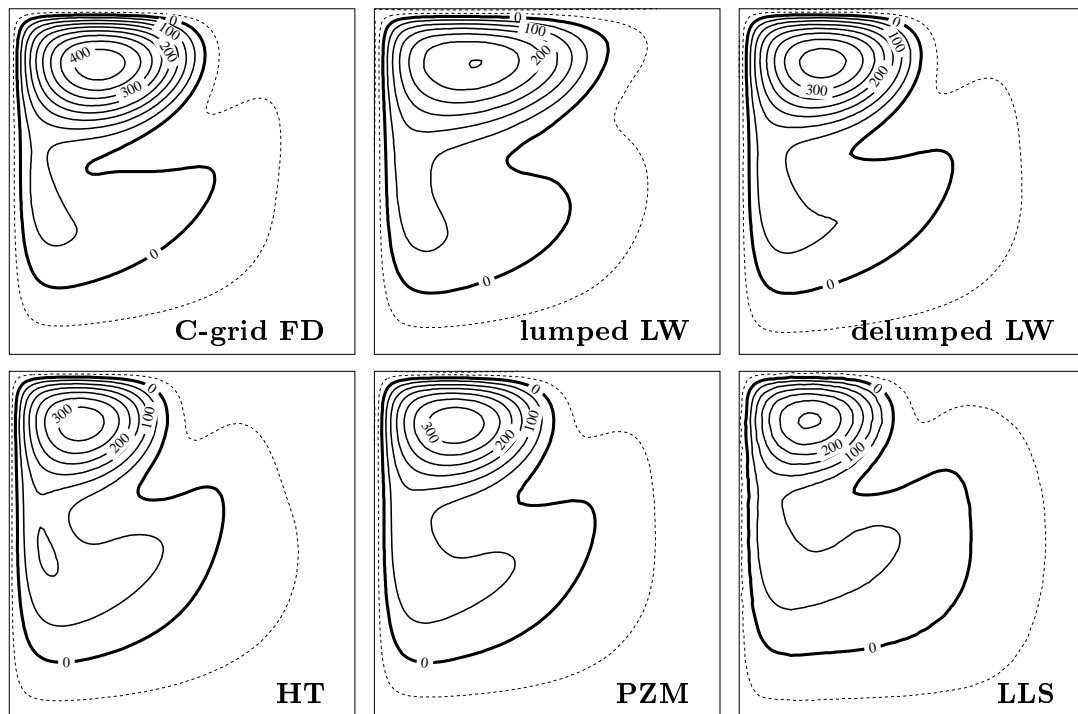


Figure 3.16: Elevation field after a 6 year spin-up for the C-grid FD, the lumped LW, delumped LW, HT, PZM and LLS FE models for the single gyre wind forcing problem.

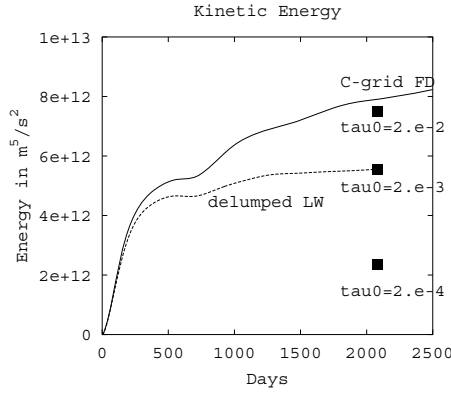


Figure 3.17: Single gyre wind forcing experiments for the delumped LW FE model compared to the C-grid FD model. As τ_0 increases the weight is more on the mass equation than on the wave equation in the LW model. This influences the value of the kinetic energy at the end of the 6 year runs (black squares). For reference, the FD curve and, LW curves for $\nu = 700 \text{ m}^2\text{s}^{-1}$ at $\tau_0 = 2 \cdot 10^{-3} \text{ s}^{-1}$.

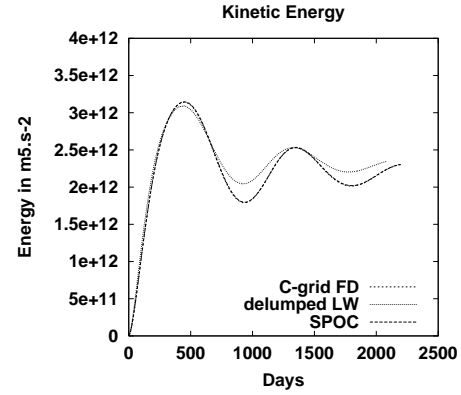


Figure 3.18: Kinetic energy during spin-up for the single gyre Munk problem with $\nu = 2000 \text{ m}^2\text{s}^{-1}$ for the C-grid FD, the delumped LW FE and SE models. The FD and SE curves are indistinguishable. For the SE model (SPOC), $n_c = 5$ and the mesh has 56 triangles.

kinetic energy curves are indistinguishable. For the SE model, Figure 3.19 gives the contours of the elevation at the end of the simulation. No discontinuities are visible, despite the fact that the solution is discontinuous by definition. A larger discrepancy is observable for a lower viscosity case ($\nu = 700 \text{ m}^2\text{s}^{-1}$, Fig.3.20) between the FE model and the FD and SE models, due to the dissipative nature of the LW model. At the end of the 6 year simulation, there is a 5% difference between the kinetic energy for the FD and SE models. This is an evidence that the SE model lacks resolution in certain parts of the domain, as some discontinuities are now visible in the elevation field (Fig.3.21).

We now examine the accuracy and cost of the FD and SE models. We have discarded the solutions obtained by all FE models because of their over-dissipative behavior. As an indicator of the accuracy, we use the kinetic energy of the basin. Since the solution of this test problem is nonlinear, a reference solution is obtained by running the spectral model for 6 years from rest with $n_c = 7$ and a mesh of 132 nodes. The er-

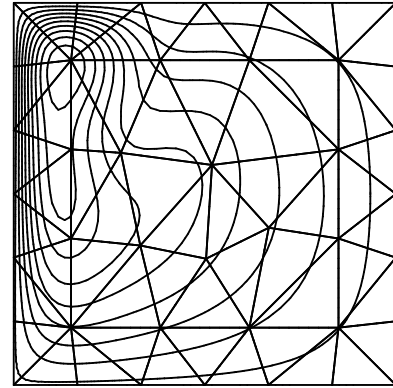


Figure 3.19: Elevation field for the SE model after 6 years from spin-up for the single gyre Munk problem corresponding to Figure 3.18.

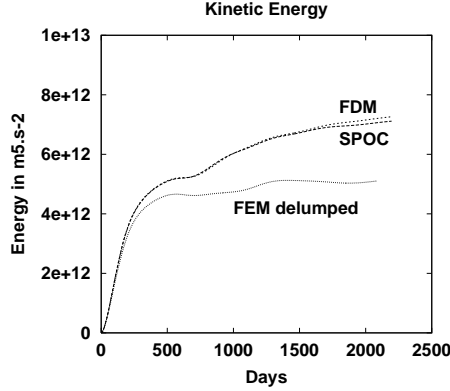


Figure 3.20: As for Fig. 3.18 but with $\nu = 700 \text{ m}^2\text{s}^{-1}$.

ror is then defined as the difference between the value of the kinetic energy obtained by one model after a 6 year run and that of the reference solution. The normalized error is computed by dividing the error by the value of the kinetic energy found in the reference solution. Figures 3.22 and 3.23 show the convergence of the error with resolution and CPU cost respectively. The fact that the finite difference results give close to second order accuracy suggests the reference solution is an accurate approximation of the true solution. These two figures confirm in general the behavior inferred from the linear test case. The convergence with resolution and CPU time is faster with higher order methods. However, the fact that there is a cross-over point indicates that below a certain resolution ($\Delta x > 10 \text{ km}$), the FD model is more accurate for the same cost. At the cross-over point the error in kinetic energy is less than 1%. Therefore, the SE model is more cost-effective than the FD model in a range of resolution for which the overall error is already below 1%.

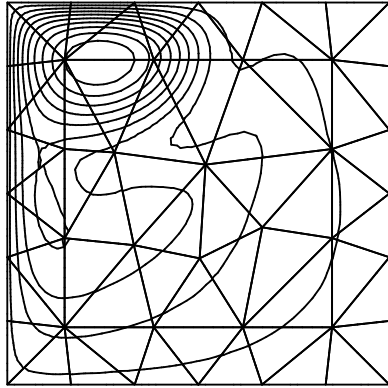


Figure 3.21: As for Fig. 3.19 but with $\nu = 700 \text{ m}^2\text{s}^{-1}$.

It is also of interest to investigate the cost-effectiveness of the adaptive refinement strategy developed in Section 2.4.3 for the SE model. Since this allows for variable resolution in space and time, it may prove more effective than having a fixed and rather uniform mesh in time. We use the refinement parameters λ_i and n_{check} given in Table 2.2 and we test the SE model for the Munk problem with $\nu = 700 \text{ m}^2\text{s}^{-1}$ for three values for λ_1 (0.3, 0.2 and 0.1), which controls the maximum discontinuity allowable between two elements. We obtain the circulation patterns of Figure 3.24 (middle panels) and meshes (top panels) at the end of the 6 year simulation. The time evolution of the number of elements for $\lambda_1 = 0.1$ (the smallest value used) shows that part of the refinement goes into following the Kelvin waves at the beginning of the simulation, which require more resolution along the boundaries (Fig. 3.24, bottom panels). When the Kelvin adjustment process weakens, a derefinement process occurs along the eastern and southern boundaries leaving higher resolution regions along the strong western return flow. As λ_1 decreases, the refined triangles get smaller and smaller, and the total number of elements at the end of the simulation increases slightly. The isolines of the elevation field are smoother than those of Figure 3.21, for

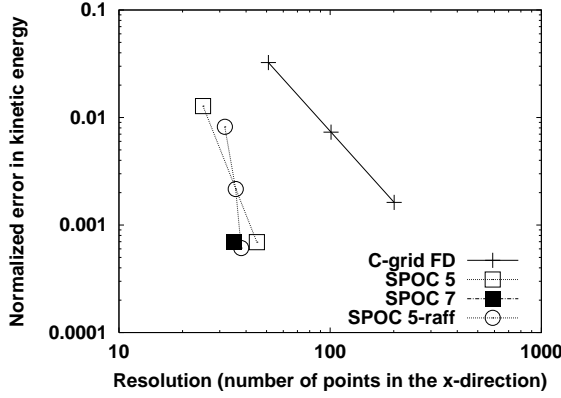


Figure 3.22: Convergence with resolution for the nonlinear Munk problem of the normalized kinetic energy error for the solution from the C-grid FD and the SE models. SPOC 5,7 corresponds to the SE model at $n_c = 5, 7$. SPOC5-raff corresponds to the adaptive SE model at $n_c = 5$.

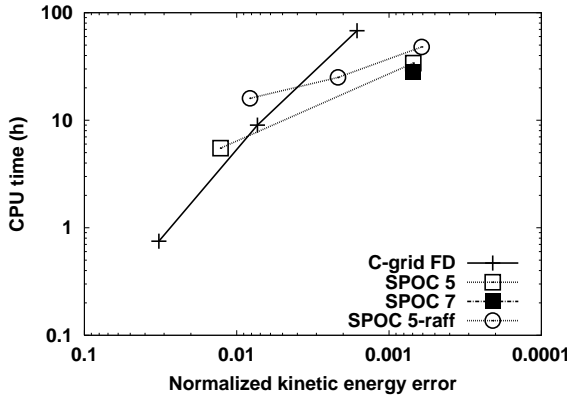


Figure 3.23: As for Fig. 3.22 but for the convergence of the normalized error with CPU cost.

Model	convergence order for the error in kinetic energy
C-grid FD	2.18
SPOC 5	4.96

Table 3.3: Convergence order for the different models for the nonlinear Munk problem in a square domain.

which a fixed and rather uniform 56-triangle mesh was used for the SE model. Therefore, the 56-triangle mesh is too coarse to model this particular Munk problem with $\nu = 700 \text{ m}^2\text{s}^{-1}$. We also note that the isolines are slightly smoother as λ_1 decreases. The convergence rate of the error in kinetic energy with resolution is better than the SE model at $n_c = 5$. However, the accuracy-to-cost convergence is not as good with the cross-over point of the FD model being at a higher accuracy level. This may be due to the fact that the refinement needed to resolve the Kelvin waves along the boundaries at the beginning of the simulation results in smaller time steps. This failure points also to a need for local time-stepping, although it is not quite clear how to implement such a procedure without loss of accuracy. Of interest is to note that the error in the kinetic energy decreases faster than λ_1 . For instance, we gain about one order in the kinetic energy error by decreasing λ_1 by a factor three. If the SE model were truly of truncation order n_c close to the element edges, the kinetic energy error should have decreased by the same factor as λ_1 . This tends to prove that the errors in the SE model are larger at the boundary between elements where the discontinuities occur. However, these errors do not seem to adversely affect the overall accuracy, possibly because these larger errors are localized to the edges of the elements.

3.5 Conclusions

We have tested in this chapter different FD, FE and SE methods. We first rule out the possibility of using a high order A-grid FD

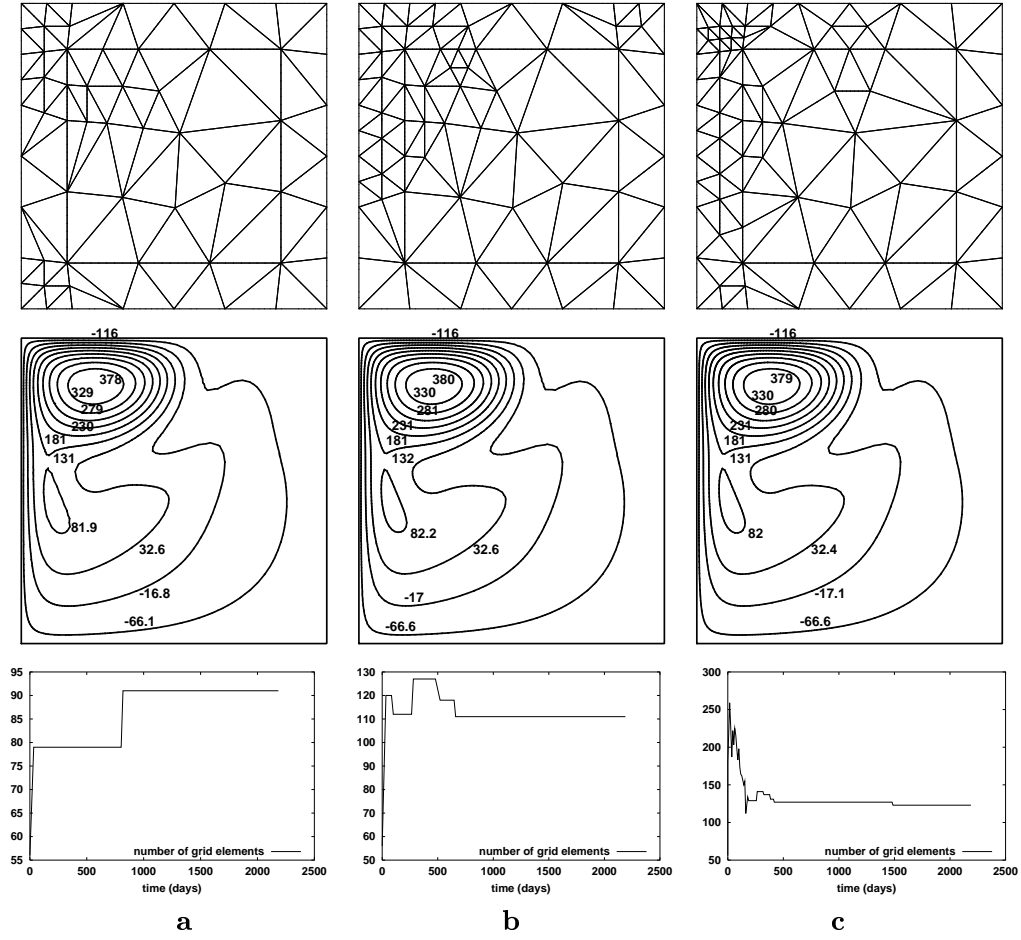


Figure 3.24: Solutions after a 6 year spin-up for the Munk problem using the adaptive SE model with $n_c = 5$. Shown are the final mesh, elevation field, and history of mesh refinement. (a) for $\lambda_1 = 0.03$, $\lambda_3 = 0.15$; (b) for $\lambda_1 = 0.02$, $\lambda_3 = 0.1$; (c) for $\lambda_1 = 0.01$, $\lambda_3 = 0.05$.

model because, in the presence of irregular geometries and for an inviscid flow, the effective truncation order is less than second order accurate. This was demonstrated in a circular domain and is due to the presence of steps occurring along the boundary when discretizing complex domains on Cartesian grids. The order of the model may have been preserved in curvilinear geometry, but we did not consider curvilinear grids as they are limited to smooth domains. The same applies to the second order C-grid model, although the loss of accuracy is less severe.

We also considered FE methods, some of which are quite simple (equal-order formulation). They all use linear basis functions for velocity and therefore we expect these methods to be no more than second order accurate. In fact, for linear applications in rectangular domains, the effective truncation order of FE models is fairly close to two. There is an increase in the errors due to the use of unstructured grids. This increase is sufficient for FD methods to outperform FE methods in terms of cost. On the other hand, in a circular domains the order of the FD methods is closer to one than two. Thus to obtain the same accuracy, the cost of using FD methods in irregular domains becomes quickly prohibitive with increasing resolution compared to FE methods. However, for nonlinear applications, all equal-order FE methods tend to be more dissipative, mostly because of the stabilizing formulations that guarantee the stability of the model. Hence, applications of these methods for non-linear oceanic flows seems problematic. There are other FE methods which are stable by construction, complying with the so-called LBB condition, and are non-dissipative (see Section 2.3 for a review on FE model stability issues). Unfortunately, the cost associated with these models is fairly large (they generally use higher than linear basis functions for the velocity and leads to fuller matrices). Moreover, as these models use lower order basis functions for the elevation (or pressure), the actual accuracy for this variable may be smaller compared to other numerical methods. Since modern altimetry offers near global coverage of the elevation of the oceans, a good FE ocean modelling strategy may be to not sacrifice the accuracy for this variable. We used the LLS model which fulfills the LBB stability condition as an illustration. We showed that the velocity errors for a linear

test case are less for this model than those of the equal-order FE models and that the elevation errors are greater. However, the increased accuracy in velocity is exactly traded off by an increased cost. Unfortunately, the nonlinear (original version) LLS model uses a semi-implicit semi-Lagrangian time formulation, which leads to dissipation when applied to the nonlinear Munk problem. Hence, all FE models considered are too dissipative for nonlinear applications. We also investigate some of the influence of the “lumping” of the mass matrix in FE models. Some authors have stressed a loss in accuracy due to lumped mass matrices (Gresho *et al.*, 1978). We found that the use of mass lumping has a detrimental influence on the double-gyre experiments with the LW model. The structure of the solution tends to be more realistic when no lumping of the mass matrix is performed.

We next considered a method based on discontinuous spectral elements. The SE method introduced in Chapter 2 shows a better accuracy than FE and FD models for $n_c > 3$. The convergence orders are not optimal though and vary between $n_c - 1$ and n_c instead of $n_c + 1$. The SE model with $n_c > 3$ is more cost-effective than FE or FD methods. This was demonstrated in a rectangular geometry most favorable to the FD model for a linear application. For the nonlinear Munk problem in a square basin, the SE model is, however, more effective than the C-grid FD model only at very high resolutions. The simple adaptive strategy we developed in Section 2.4.3 for the SE model, and tested in the previous section, gives encouraging results. It is not nearly as cost-effective to use compared to a fixed mesh, but it may be useful to resolve the fine details of the oceanic circulations whose locations are not a priori known. Hence this SE model appear cost-effective to simulate nonlinear oceanic flows in irregular domains. The only limitation though is that the model tends to give poor results in presence of singular geometrical features like steps (see Section 2.4.4) and therefore requires continuously curved boundaries.

The C-grid FD model using the vorticity-divergence stress tensor and the enstrophy conserving advective scheme might be a good candidate for general ocean modelling. The loss of accuracy of second-order FD meth-

ods in presence of step-like geometry is less than one order. This loss is less compared to that suffered by the 4th order FD model. A second order FD model might thus still be competitive compared to intricate LBB-complying FE methods. However there are other limitations. From Chapter 1 we know that FD methods have problems representing the fast Kelvin modes if the resolution is too low compared to the radius of deformation. Therefore, a FD model should have many points resolving the radius of deformation, which significantly increases the cost. However, in the context of the Munk problem, it is not clear how retarded Kelvin waves affect the steady state of the ocean. We propose to further investigate these issues in the context of the single gyre Munk problem in Chapter 4.

Chapter 4

Finite Difference Methods in Rotated Basins

In this chapter, we further investigate the influence of steps on finite difference models and, in particular, we consider the accuracy of model vorticity budgets for wind-driven circulations under the free-slip dynamic boundary condition. Free-slip circulations are typically more energetic than no-slip circulations, e.g. Pedlosky (1996). He considered the vorticity budget for a quasi-geostrophic (QG) model. Simple scaling arguments reveal that vorticity is more easily fluxed out of the basin when no-slip conditions are employed. When there is a net vorticity forcing under free-slip conditions, therefore, stronger gyres are needed to achieve the necessary viscous flux of vorticity across the basin boundary. The vorticity budget is also an interesting diagnostic tool because all the terms are in the form of domain integrals that can be transformed into boundary integrals. This suggests that values of these integrals may be very sensitive to coastline representation and that careful consideration of the vorticity budget may give further insight into the effect of steps on the overall strength of the gyres. The difficulty is in deriving a vorticity budget consistent with the model's numerical formulation.

We propose to test different formulations for the advective and diffusive terms for the shallow water C-grid model detailed in Section 4.2. Additionally, we use vorticity budgets to investigate problems we found with the B-grid model in Section 4.3. Finally, we draw some similarities with results from a quasi-geostrophic (QG) FD model in Section 4.4. Indeed, it may seem reasonable that vorticity budgets are more accurate in QG models since the vorticity equation is

solved instead of the primitive equations. Section 4.1, 4.2 and 4.4 are excerpts from a paper we intend to submit to *Tellus* (the authors are Frédéric Dupont, David N. Straub and Charles A. Lin).

4.1 Introduction

To date, there have been few studies focusing on the issue of coastline representation in finite difference models. Schwab and Beletsky (1998) studied the influence of steps on inviscid Kelvin waves. Adcroft and Marshall (1998, hereafter referred as AM) addressed the problem in the context of the single gyre nonlinear Munk problem using a C-grid shallow water (SW) model. They showed (as did Cox, 1979) that the horizontal circulation under no-slip boundary condition is not very sensitive to the presence of steps along the coastline. This can be explained by the fact that the core of the boundary current under no-slip is located a few grid points inside the interior of the basin.

For free-slip, however, they compared results from non-rotated and rotated square basin experiments and showed the circulation to be highly sensitive to the presence of steps along the walls. In rotated basin experiments, the basin was rotated relative to the grid axes (see Fig. 2.1), but the wind forcing and north-south axis were kept constant relative to the basin, so that the only differences between the experiments are due to the discretization. The presence of steps along

the boundary tends to reduce the strength of the circulation to the extent that results obtained using free-slip boundary conditions with step-like boundaries more closely resembles those with no-slip boundary conditions than free-slip solutions without steps. Moreover, they showed that, at least for small rotation angles, sensitivity to steps under free-slip conditions could be greatly reduced by using a vorticity-divergence formulation of the viscous stress tensor (Madec *et al.*, 1991), hereafter referred as the δ - ζ formulation.

We conclude this section with two remarks. The first concerns the representation of the coastline in FD models. Some methods exist to treat exactly a coast not oriented along the discretization axes (e.g., Forrer and Jeltsch, 1998). These methods have their own limitations such as time-step limitation problems and the treatment of viscous stresses at the boundary. However, the emphasis of our study is not on developing or investigating new FD models. The second issue relates to the kind of idealized experiments we have performed. We have deliberately introduced artificial steps in the model boundary in these experiments. The precise applicability of our results to a real ocean basin with irregular coastline remains to be determined.

4.2 Vorticity Budgets in a C-grid SW Model

In this section, we compare the analytic vorticity budget with the equivalent discretized vorticity budget for a C-grid shallow water (SW) model and explain why the two budgets do not match. We then give results for the discretized vorticity budget and discuss the implications in terms of modelling of wind driven gyres in presence of step-like coastlines.

4.2.1 The General Form of the Discretized Vorticity Budget

We consider the shallow water equations

$$\partial_t \mathbf{u} + \mathbf{u} \cdot \nabla \mathbf{u} + f \mathbf{k} \times \mathbf{u} + \nabla(g h) = \frac{\tau}{h} + \nu \nabla^2 \mathbf{u} \quad (4.1)$$

$$\partial_t h + \nabla \cdot (\mathbf{u} h) = 0 \quad (4.2)$$

where the variables are given in Table 2.1. It is sometimes convenient to recast the nonlinear terms in (4.3) in the following form:

$$\partial_t \mathbf{u} + q \mathbf{k} \times (\mathbf{u} h) + \nabla B = \frac{\tau}{h} + \nu \nabla^2 \mathbf{u}, \quad (4.3)$$

where q and B are also given in Table 2.1. The kinematic boundary condition is no normal flow and the dynamic boundary condition is taken to be free-slip. The vorticity equation is found by taking the curl of (4.3),

$$\partial_t \zeta + \nabla \cdot (q h \mathbf{u}) = \mathbf{k} \cdot \nabla \times \left(\nu \nabla^2 \mathbf{u} + \frac{\tau}{h} \right). \quad (4.4)$$

Upon integration of this equation over a closed basin, the divergence of the potential vorticity mass flux cancels out and we get

$$\partial_t \left(\int_{\Omega} \zeta dx dy \right) = \nu \oint_{\partial \Omega} \frac{\partial \zeta}{\partial n} dl + \oint_{\partial \Omega} \frac{\tau \cdot \mathbf{dl}}{h}. \quad (4.5)$$

Eqns. (4.1-4.2) or (4.2-4.3) can be discretized in different ways. To simplify the discussion, we leave the time derivative being continuous, and restrict ourselves to the C-grid. A useful general form of the SW equation is the following:

$$\partial_t u + C_u + D_x^- \Phi = \frac{\tau_x}{h} + F_x \quad (4.6)$$

$$\partial_t v + C_v + D_y^- \Phi = \frac{\tau_y}{h} + F_y \quad (4.7)$$

$$\partial_t h + D_x^+ U + D_y^+ V = 0 \quad (4.8)$$

where $\mathbf{C} = (C_u, C_v)$ represents the advection-Coriolis terms, Φ represents a potential function, $\mathbf{F} = (F_x, F_y)$ are the viscous terms and other notation is described in Section 2.2.2. The exact forms of \mathbf{C} , Φ and \mathbf{F} depend on choices made with respect to the discretization. For example, Φ might represent the Bernoulli function or simply the

pressure, depending on whether a formulation based on (4.1) or on (4.3) is employed. We first make a general point about numerical vorticity budgets and later discuss the peculiarities specific to choices for \mathbf{C} , Φ and \mathbf{F} . From (4.6) and (4.7) we write the discretized vorticity equation

$$\begin{aligned} \partial_t \zeta = & -D_x^- C_v + D_y^- C_u \\ & + D_x^- F_y - D_y^- F_x + D_x^- \left(\frac{\tau_y}{\bar{h}} \right) - D_y^- \left(\frac{\tau_x}{\bar{h}} \right). \end{aligned} \quad (4.9)$$

This equation is defined at interior ζ -nodes (excluding the boundary nodes), because it requires defining momentum equations at all neighboring velocity nodes (white squares in Fig.4.1). Now we want to sum over all interior ζ -indices in order to get the model vorticity budget. For simplicity, we write vectors in place of x - and y - components, even though the components are not discretized at the same location (see Chapter2):

$$\partial_t \sum_{ij \in \Omega_\zeta} \zeta \Delta x \Delta y = \sum_{ij \in \delta \Omega_\zeta} (\mathbf{C} + \mathbf{F} + \frac{\boldsymbol{\tau}}{\bar{h}}) \cdot \boldsymbol{\Delta l}, \quad (4.10)$$

where $\delta \Omega_\zeta$ is the ensemble of indices representing the velocities nodes of the envelope of the interior vorticity node domain, Ω_ζ (black nodes in Fig.4.1). We rewrite (4.10) in a more convenient form by defining

$$\mathcal{F}_{adv} = \sum_{ij \in \delta \Omega_\zeta} \mathbf{C} \cdot \boldsymbol{\Delta l}, \quad (4.11)$$

$$\mathcal{F}_{vis} = \sum_{ij \in \delta \Omega_\zeta} \mathbf{F} \cdot \boldsymbol{\Delta l}, \quad (4.12)$$

$$\mathcal{F}_i = \sum_{ij \in \delta \Omega_\zeta} \left(\frac{\boldsymbol{\tau}}{\bar{h}} \right) \cdot \boldsymbol{\Delta l}. \quad (4.13)$$

Thus (4.10) becomes

$$\partial_t \sum_{ij \in \Omega_\zeta} \zeta \Delta x \Delta y = \mathcal{F}_i + \mathcal{F}_o = \mathcal{F}_i + \mathcal{F}_{adv} + \mathcal{F}_{vis}. \quad (4.14)$$

\mathcal{F}_i (flux in) is the wind input of vorticity and \mathcal{F}_o (flux out) is the sum of the viscous diffusion flux, \mathcal{F}_{vis} , and of the advective flux, \mathcal{F}_{adv} . The important point here is to note that \mathcal{F}_{adv} ideally should be zero since it represents an advective flux through the basin

lateral boundary. It is not zero in the numerical model because the domain boundary for the model vorticity budget is located half a grid point inside the domain (see Fig. 4.1). However, as the resolution increases, the region delimiting the vorticity budget domain approaches the model boundary and, \mathcal{F}_{adv} should converge to zero. How quickly this occurs will depend on the numerical formulation.

It is always possible to approximate the vorticity budget at the model boundary by using off-centered derivatives and interpolating some of the variables to the boundary. The model numerics, however, make no use of variable values found by such an interpolation and therefore, a vorticity budget calculated in this way must be considered distinct from the model vorticity budget. Such a budget might misrepresent the contribution of the different terms of the discretized equations of the model, especially if the error introduced by the coastline discretization is of lower order than are the truncation errors of the model. For this reason, we prefer to use the model vorticity budget. We note also that the truncation errors in the model vorticity budget are larger than the truncation errors in solving the shallow water equations, since vorticity is a higher order variable.

Figure 4.2 compares the rotated and non-rotated basin cases. The integrand ($\mathbf{C} \cdot \boldsymbol{\Delta l}$ —i.e. the local \mathcal{F}_{adv}) is plotted as a function of distance around the basin perimeter and the position of the steps is evident from the abrupt jumps in the integrand value. When summed along the perimeter, \mathcal{F}_{adv} is non-zero and is larger for the rotated basin experiment compared to the non-rotated basin experiment. Starting from this observation, we are interested in quantifying the importance of the steps over the global vorticity budget. First, as increased resolution leads to more steps, and due to the singular behavior of $\mathbf{C} \cdot \boldsymbol{\Delta l}$ close to steps, it is no longer obvious that \mathcal{F}_{adv} converges to zero with increasing resolution. From this point of view, \mathcal{F}_{adv} is probably very sensitive to the formulation of the advective terms in (4.10), and extension in (4.1,4.3). Second, we want to investigate whether the overall circulation is sensitive to the presence of an extra term in the global vorticity budget, as \mathcal{F}_{adv} can be a source or a sink term, depending on its sign.

4.2.2 Numerical Formulations

We are interested in applying different formulations for the advection-Coriolis terms since we noted that \mathcal{F}_{adv} was generally non-zero for the single gyre Munk problem, with the integrand being particularly large at steps. The two advective numerical schemes that we consider are the conventional formulation (based on Eq. 4.1) and the potential enstrophy conserving formulation (based on Eq. 4.3).

In addition to testing for sensitivity to the choice of advective schemes, we also consider different formulations of the stress tensor. That the overall circulation is primarily sensitive to the formulation of the stress tensor is the main result of AM, who found that the $\delta\text{-}\zeta$ formulation gave better results than the conventional formulation. We refer to Gent (1993) and Shchepetkin and O'Brien (1996) for a more complete discussion on appropriate viscous stress tensor formulations for the shallow water equations and we limit ourselves to the two stress tensor formulations used by AM. Below, we review these two formulations. Thus, we are interested in testing four combinations of two advective and two diffusive formulations. Table 4.1 summarizes these four different combinations.

With respect to the advection-Coriolis terms, we compare the conventional formulation to the potential enstrophy conserving formulation of Sadourny (1975). For the conventional formulation, \mathbf{C} and Φ are given by

$$\begin{cases} C_u = uD_x^o u + \overline{v}^x \overline{y} D_y^o u - f \overline{v}^x \overline{y} \\ C_v = uD_x^o v + \overline{v}^x \overline{y} D_y^o v + f \overline{v}^x \overline{y} \\ \Phi = gh \end{cases} \quad (4.15)$$

and for the potential enstrophy conserving formulation, \mathbf{C} and Φ are given by

$$\begin{cases} C_u = -\overline{q}^y \overline{V}^x \overline{y} \\ C_v = \overline{q}^x \overline{U}^x \overline{y} \\ \Phi = gh + \frac{1}{2}(\overline{u}^2 \overline{x} + \overline{v}^2 \overline{y}) \end{cases} \quad (4.16)$$

Both formulations ensure a second order accuracy to the discretized SW equations. For the conventional formulation, changes are made to incorporate the boundary conditions at second order of accuracy, by using

off-centered differencings close to the boundary. No boundary condition for the vorticity is required. However, since the enstrophy conserving scheme explicitly uses the vorticity, this formulation requires that vorticity be specified at boundary points. We choose to set the relative vorticity to zero along the model boundary, which is consistent with the free-slip boundary condition along straight walls. Also, contrary to the conventional formulation, no off-centered differencing is needed at the boundary for the computation of \mathbf{C} .

The two numerical formulations that we consider for the viscous terms are the divergence-vorticity tensor formulation of Madec *et al.* (1991) and the conventional five-point Laplacian. For the latter,

$$\begin{cases} \nabla^2 u_{ij} = \frac{u_{i-1,j} - 2u_{ij} + u_{i+1,j}}{\Delta x^2} \\ \quad + \frac{u_{i,j-1} - 2u_{ij} + u_{i,j+1}}{\Delta y^2} \\ \nabla^2 v_{ij} = \frac{v_{i-1,j} - 2v_{ij} + v_{i+1,j}}{\Delta x^2} \\ \quad + \frac{v_{i,j-1} - 2v_{ij} + v_{i,j+1}}{\Delta y^2} \end{cases} \quad (4.17)$$

As with the conventional advection formulation, changes are made here to incorporate the boundary conditions at second order accuracy, by using off-centered differencings. Another technical remark concerns the treatment of velocity points close to tips of land. For those points (the u and v points of Fig. 4.3), the tip of the land is half a grid cell away. Let us focus on the u -point. The problem is to evaluate the Laplacian of u at this point. A five-point Laplacian requires knowledge of $\partial u / \partial y$ in the center of the northern and southern sides of the cell surrounding the u -point, and $\partial u / \partial x$ on the eastern and western sides. The problem lies with $\partial u / \partial y$ on the northern side. The usual treatment would have

$$\left. \frac{\partial u}{\partial y} \right|_{north} = \frac{u_{i,j+1} - u_{ij}}{\Delta y} \quad (4.18)$$

which simplifies to

$$\left. \frac{\partial u}{\partial y} \right|_{north} = -\frac{u_{ij}}{\Delta y}, \quad (4.19)$$

because of the impermeability condition which sets $u_{i,j+1}$ to zero. Alternatively, one

might take impermeability to imply that the tip is a stagnation point, in which case an off-centered differencing leads to

$$\left. \frac{\partial u}{\partial y} \right|_{north} = -\frac{2 u_{ij}}{\Delta y} . \quad (4.20)$$

A third logical possibility would be to apply the free slip condition at the tip to conclude that

$$\left. \frac{\partial u}{\partial y} \right|_{north} = 0 . \quad (4.21)$$

We choose the latter (4.21), in order to let the “fluid” slip as much as possible along the walls since the first two conditions (4.19, 4.20) tend to slow down the boundary currents. A more accurate formulation of the boundary condition close to the steps can be derived using a finite volume formulation, which treats the northern viscous flux as a mean between (4.19) and (4.21). However, this would slow down the boundary current due to the use of (4.19). In addition, more accurate treatment of the steps have limited value as the steps are artificial.

The divergence-vorticity (δ - ζ) form of the stress tensor leads to the following form for the Laplacians

$$\begin{cases} \nabla^2 u_{ij} = D_x^- \delta - D_y^+ \zeta \\ \nabla^2 v_{ij} = D_y^- \delta + D_x^+ \zeta \end{cases} \quad (4.22)$$

where δ is the divergence expressed at the h -location (center of the cell). This formulation is more general in the sense that there is no adjustment of the formulation at the boundary. Another remark concerns the case of straight walls. In that particular case, there is no difference between the δ - ζ stress tensor formulation and the traditional formulation. The difference is in the treatment of steps.

To illustrate this, we consider a comparison between the two stress tensor formulations for a forward step along a north-flowing western boundary current. Choose (i, j) so that, in Figure 4.3, the ζ -point right at the tip of the land corner would have $(i, j+1)$ indices (see Fig. A.1 for indices arrangement). Thus, the viscous terms under the δ - ζ formu-

lation are

$$\begin{cases} \nabla^2 u_{ij} &= \text{conventional part} + \frac{v_{i,j+1}}{\Delta x \Delta y} \\ \nabla^2 v_{i,j+1} &= \text{conventional part} + \frac{u_{ij}}{\Delta x \Delta y} \end{cases} , \quad (4.23)$$

where the additional terms are positive. These additional terms represent a forward-acceleration. As AM noted, a serious inconvenience of the conventional formulation is that, in presence of steps, there is “extra diffusion” of momentum due to additional velocity points set to zero at the boundary (the impermeability condition), as compared to the straight wall case. This extra diffusion is responsible for slowing down the boundary currents. Therefore, the accelerating terms of the δ - ζ formulation partly compensate the decelerating terms of the conventional formulation.

A final remark is that the divergence part of the viscous forces cancels out in the vorticity equation. Therefore, in the discretized vorticity equation, the δ - ζ formulation leads to a viscous term that takes the form of the five-point Laplacian of the vorticity. This is not true of the conventional formulation.

4.2.3 Results

By studying \mathcal{F}_{adv} , we want to address several issues related to the accuracy of the different combinations of the advection and diffusion formulations and their influence on the strength of the overall circulation. Firstly, a major requirement is that, whatever the geometry of the basin, \mathcal{F}_{adv} should converge to zero as the resolution goes to infinity. This test allows us to rank the performances of the model for the different combinations of advective and diffusive schemes. Of particular interest will be the importance of the advective formulation. A second concern is to assess whether the size of the artificial source or sink of vorticity due to \mathcal{F}_{adv} influences the overall strength of the gyres. A third concern relates to the general accuracy of model vorticity budgets.

To address these issues, we make use of the conceptual experiment proposed by AM, in which a single gyre Munk circulation is

Model	Advection form	Stress tensor form
A	enstrophy preserving advection	conventional stress tensor formulation
B	enstrophy preserving advection	δ - ζ stress tensor formulation
C	conventional advection	conventional stress tensor formulation
D	conventional advection	δ - ζ stress tensor formulation

Table 4.1: The four combinations of advection formulations and stress tensor formulations.

computed in rotated and non-rotated square basins. In both cases, all parameters and forcing are unchanged except for the discretized coastline. The four combinations (A, B, C, D) of numerical formulations we propose to test are detailed in Table 4.1. One remark concerns the non-rotated basin results. There, since the conventional and δ - ζ stress tensor formulations are identical, the results for the B combination are identical to the results for A. The same applies for the C and D cases.

We reproduce the results of AM in Figure 4.4. This figure shows the elevation fields for the A and B cases and for no rotation and a small rotation angle of 3.4° . Clearly, the A case shows circulation patterns collapsing as the number of steps along the walls increases whereas, for the B case, the circulation is quite similar to the original non-rotated circulation. The results for C are not shown but are very similar to the results for A. The results for D show a small increase in the strength of the gyre compared to A, but the original overall circulation of A-B with no rotation is not recovered (not shown).

Figure 4.5a shows the kinetic energy as a function of resolution for the various combinations and for a rotation angle of 3.4° . Only the B combination converges to non-rotated solutions. The A and C results are almost identical, but appear to converge to a kinetic energy that is reduced by over a factor of 2 compared to the non-rotated cases. For the D combination, kinetic energy decreases and then tends to slightly increase with increasing resolution and is generally much lower than for A-B with no rotation or B with rotation.

As mentioned, the first consistency test related to the vorticity budget is to verify that \mathcal{F}_{adv} converges to zero with increasing resolution. For all rotation angles considered and for the B combination, this statement appears to be true. For the other combinations (A, C, D), such is not the case, at least for certain angles. For instance, \mathcal{F}_{adv} tends to increase or stay constant for the A, C and D combinations at 3.4° (Fig. 4.5b). For the D case, \mathcal{F}_{adv} increases dramatically with increasing resolution —so much that \mathcal{F}_{adv} becomes larger than the wind input. Associated with this is a reverse (negative) viscous flux. This behavior may have consequences on the stability of the model. Although no obvious numerical instabilities occurred for a rotation angle of 3.4° , numerical instabilities cause the model to crash for other angles, for example at -30° . It seems plausible that this behaviour is associated with the large (and opposing) advective and diffusive fluxes of vorticity near the model perimeter. In any event, it seems reasonable to conclude that the D combination is inappropriate. This implies that the δ - ζ viscous formulation performs well only when used in conjunction with the enstrophy conserving advection. This finding complements that of AM. For the A and C combinations (Fig. 4.5b), \mathcal{F}_{adv} does not converge toward zero with increasing resolution. Hence, these two combinations seem inappropriate, even if the resulting solutions are always stable.

We now address the issue of possible correlation between \mathcal{F}_{adv} and the kinetic energy. Given that inertial runaway (the inability of simple models of the ocean to converge to a reasonable statistical mean solution as the eddy viscosity is decreased to the real value of the viscosity found in water) appears to be related to “difficulties” in balancing the

global vorticity budget (Pedlosky, 1996), it seems reasonable to ask whether the sign of \mathcal{F}_{adv} is correlated with an indicator of the overall strength of the gyre, such as total kinetic energy. For example, when \mathcal{F}_{adv} is negative, it adds to the wind input of vorticity and one might expect a stronger gyre to result. Some evidence that this may be the case is found by comparing B and D, which share the same formulation of the viscous terms. Figure 4.5b shows that \mathcal{F}_{adv} is positive and larger for D than is the case for combination B. Thus the total wind plus advective input of vorticity to the basin is stronger in case B. As might have been anticipated, B shows a more energetic circulation (Fig. 4.5a). It is also interesting to see whether there is any correlation between kinetic energy and the sign/strength of \mathcal{F}_{adv} for a given formulation of the numerics. We restrict this discussion to the use of the B combination. From figures 4.6 and 4.7, which show the kinetic energy and advective/wind vorticity input ratio for a range of resolution and rotation angles, there does not appear to be any striking correlation. In particular, if we focus on the region of negative values of \mathcal{F}_{adv} (i.e., for a case where \mathcal{F}_{adv} has the same sign as the wind input), the kinetic energy for this region is not larger than the kinetic energy at the same resolution but for an opposite angle (in fact, the kinetic is slightly lower). Presumably the added advective flux in this region is locally balanced by the viscous terms, so that processes analogous to those thought to be responsible for inertial runaway do not lead to an increase in the overall strength of the gyre.

To conclude this section, we investigate the general accuracy of model vorticity budgets with respect to \mathcal{F}_{adv} using the B combination, only, since this combination is the only one showing a robust convergence to zero with increasing resolution. As \mathcal{F}_{adv} should ideally not be present in the vorticity budget, the viscous flux, \mathcal{F}_{vis} , can be either underestimated or overestimated (which modifies the local balance at the wall and therefore the strength of the gyre) and \mathcal{F}_{adv} can be viewed as an error. From Figure 4.8 and for the range of resolution we used, \mathcal{F}_{adv} varies between 5% and 50% of the wind input. The order of the convergence for \mathcal{F}_{adv} with increasing resolution is fairly close to unity or slightly lower for all positive angles. For negative angles, we did not compute the

convergence order because \mathcal{F}_{adv} goes through a minimum (Figure 4.7) and had not asymptoted to an uniform convergence order at the highest resolutions we considered. A noteworthy point is that the effect of increasing the rotation angle (introducing more steps) seems to decrease the convergence order (1/2 at 20°). Paradoxically, however, the convergence order increases again to reach unity for 45°, the rotation angle at which the number of steps is maximum. In fact, at this angle \mathcal{F}_{adv} even shows a negative offset compared to the 0° angle.

Except for effects related to step-like boundaries, that the convergence order is unity follows directly from the order of discretization of the vorticity. Since the vorticity is one order higher a variable than is velocity, and since the velocity is computed at second order accuracy, it follows that the vorticity is at best accurate to first order. Therefore, \mathcal{F}_{adv} can be considered an explicit first order (at best) error in the vorticity budget. For the B combination, we observe that the convergence order for \mathcal{F}_{adv} varies between 1/2 and unity, depending on the rotation angle. In the 1/2 order case, errors (or discrepancies) vary between 25% (high resolution) and 50% (coarse resolution) and, in the first order case, they vary between 6% and 22%. The errors are much larger for the other combinations and can reach 100%. This implies that the accuracy of computing vorticity budgets from primitive equations models is fairly low, especially in absence of attention to the numerics. These errors may also vary a lot considerably with the discretized domain geometry.

4.3 Vorticity Budgets in SW B-grid Models

This section stems from our interest in generalizing our experience from C-grid vorticity budgets to the B-grid (see Section 2.2.2). Under free-slip boundary conditions, the main difficulties arise from the fact that a prognostic equation for the tangential velocity along the wall has to be solved. This equation requires values of the pressure gradient along the wall, although the nearest elevation points are half a grid cell away in the

interior. The zero-order solution is to use the same elevation value as at the nearest interior point, but this solution yields unreasonable shears of the tangential velocity close to the wall. In fact, the current along the wall tends to be zero or opposite to the overall gyre circulation. The problem stems from a poor representation of the geostrophic balance along the wall. For the current to be maximal at the wall, the pressure at the wall has to be larger than the pressure at the interior points. However, since the free-slip boundary condition yields a zero normal gradient for the tangential velocity, this means that the second derivative normal to the wall of the pressure should be approximately zero. Therefore, the pressure varies nearly linearly in the normal direction to the wall.

We therefore tested a simple linear extrapolation, using two interior pressure points. This approximation gives better results in the sense that there is no longer opposite currents along the wall. However the overall solution does not converge to the solution obtained with the C-grid model. After six years of simulation, the kinetic energy is three times as much as for the C-grid model (see Table 4.2). The circulation is too strong. From a vorticity budget perspective, the model cannot flux out the wind input of vorticity. The reason may come from the presence of a pressure term in the vorticity budget which acts as a torque¹. This term should normally be zero. It arises from the non-cancellation of the pressure gradient terms close to each corner of the basin. This term is negative and therefore acts the same way as the wind input (see Table 4.2). It might be that the small discrepancy caused by the presence of this pressure term in the vorticity budget is enough that the model cannot converge to a reasonable solution. Nonetheless, we noted that the magnitude of this term decreases with resolution and might explain why the kinetic energy tends to decrease with increasing resolution. Due to the difficulty of tuning this free-slip B-grid model, we quickly gave up the idea of generalizing the experiments performed in the previous sections to the B-grid.

We noted however that some authors tackle the problem of the B-grid under

¹The advective and Coriolis contribution to the vorticity is zero for the B-grid. See Appendix B.

Δx	20 km	10 km	5 km
K. Energy in 10^{10} m^5s^{-2}	—	2617	2473
FI in m^2s^{-2}	—	-0.2647	-0.2606
FO in m^2s^{-2}	—	0.2639	0.2604
Pressure term in m^2s^{-2}	—	-2.388 $\times 10^{-3}$	-1.238 $\times 10^{-3}$

Table 4.2: Summary of the vorticity budget and kinetic energy diagnostics for the B-grid after a spin-up of 6 years. Instantaneous values after a 6 year spin-up. The model vorticity budget on a B-grid includes a pressure term due to the non-cancellation of the pressure gradient at the corners of the domain.

free-slip boundary conditions. Hsieh *et al.* (1983), for instance, suggest the idea of shifting the whole grid, so that elevation points are on the boundary instead of velocity points. The trouble then is that we lose the main advantage of the traditional B-grid which is that the region for the vorticity budget domain is exactly the model domain. Using the traditional implementation of the B-grid, there is no advective flux of vorticity. More recently, Beckers (1999) proposes to keep the traditional B-grid and to iterate at each time-step in order to get elevation values at land points close to the boundary that yield a zero normal velocity. This solution is of course more expensive. Unfortunately, we did not try to implement one of these solutions since our attention was already focused on more complex numerical methods. It is sufficient to note that implementation of free-slip boundary conditions are not trivial on B-grids. This adds to problems encountered with a similar implementation in a A-grid (see Section 3.4). Thus the free-slip boundary condition does not seem to be such an easy condition to implement in general in any model.

4.4 The Quasi-Geostrophic Model

4.4.1 Discretization

We also investigated the influence of coast-line discretization in quasi-geostrophic (QG) models, although our main interest in this thesis is focused on the shallow water (SW) models. QG models solve the vorticity equation directly. It seems therefore a reasonable assumption that these models should yield more accurate vorticity budgets than do SW and primitive equation models. The vorticity equation used is

$$\partial_t \zeta + J(\psi, \zeta) + \beta \partial_x \psi = \nu \nabla^2 \zeta + \mathbf{k} \cdot \nabla \times (\boldsymbol{\tau}/h) , \quad (4.24)$$

where ψ is the streamfunction. Equation 4.24 corresponds to a barotropic and geostrophic ocean with a rigid lid approximation. The wind forcing is altered to include the influence of the water depth in order to better mimic the shallow water equations. The discretization of (4.24) is done using second order center differencings. The streamfunction formulation ($\zeta = \nabla^2 \psi$) leads to a linear pentagonal system of equations to solve at each time step. We used the simple leapfrog time integration and the viscous term is discretized by the conventional five-point Laplacian. We are interested in testing different formulations of the Jacobian in (4.24), as the formulation of this term may have consequences for the vorticity budget for the same reasons mentioned previously for the C-grid model.

As for the SW C-grid model, the vorticity budget for the QG model is defined only on an interior sub-domain, half a grid point inside the model basin. This follows from the fact that the vorticity equation is only solved at interior points (see Figure 4.1). The discretized vorticity budget is

$$\begin{aligned} \sum_{ij \in \Omega_\zeta} \partial_t \zeta \Delta x \Delta y = & \sum_{ij \in \Omega_\zeta} [-J - \beta D_x^o \psi + \nu \nabla^2 \zeta \\ & + D_x^o(\boldsymbol{\tau}_y/h) - D_y^o(\boldsymbol{\tau}_x/h)] \Delta x \Delta y , \end{aligned} \quad (4.25)$$

where notation is found in Section 2.2.2 and

Ω_ζ is the ensemble of indices for points whose location lies in the interior domain. By defining

$$\mathcal{F}'_{adv} = - \sum_{ij \in \Omega_\zeta} J \Delta x \Delta y \quad (4.26)$$

$$\mathcal{F}_{vis} = \sum_{ij \in \Omega_\zeta} \nu \nabla^2 \zeta \Delta x \Delta y \quad (4.27)$$

$$\mathcal{F}_c = \sum_{ij \in \Omega_\zeta} -\beta D_x^o \psi \Delta x \Delta y \quad (4.28)$$

$$\mathcal{F}_i = \sum_{ij \in \Omega_\zeta} [D_x^o(\boldsymbol{\tau}_y/h) - D_y^o(\boldsymbol{\tau}_x/h)] \Delta x \Delta y , \quad (4.29)$$

we recast the vorticity budget in the following form

$$\sum_{ij \in \delta \Omega_\zeta} \partial_t \zeta \Delta x \Delta y = \mathcal{F}'_{adv} + \mathcal{F}_c + \mathcal{F}_{vis} + \mathcal{F}_i . \quad (4.30)$$

One main characteristic of QG vorticity budgets is the explicit contribution of the beta term, \mathcal{F}_c . This contribution is hidden in \mathcal{F}_{adv} for the SW models. Therefore, we define \mathcal{F}_{adv} here to be $\mathcal{F}_{adv} = \mathcal{F}'_{adv} + \mathcal{F}_c$, where \mathcal{F}'_{adv} represents the integration of the Jacobian term over Ω_ζ . We focus our study on the behavior of both \mathcal{F}'_{adv} and \mathcal{F}_c . As for the C-grid model, a minimum requirement is that \mathcal{F}_{adv} goes to zero at infinite resolution. This also applies to \mathcal{F}'_{adv} and \mathcal{F}_c separately. We propose to test three different numerical formulations of the Jacobian, J_1 , J_3 and J_7 , as termed by Arakawa and Lamb (1977) (hereafter, AL77) and investigate their respective influence on the vorticity budget. Other discretization techniques exist that nullify \mathcal{F}_c , such as that developed by Salmon and Talley (1989), but we fear that those techniques miss the point that the vorticity budget can not clearly be defined in the sub-region along the boundaries. Such a technique may reduce the actual size of the model domain to the point that the critical sub-region disappears.

Representation of the Jacobian in (4.25) has been extensively considered by Arakawa (1966) and AL77. From the latter, we borrow the notation J_i , where J is the discretized Jacobian and i takes values between 1 to 7, depending on the discretized formulation. The simplest representation is the J_1

Jacobian, where

$$J_1 = D_x^o \zeta D_y^o \psi - D_y^o \zeta D_x^o \psi . \quad (4.31)$$

J_1 conserves relative vorticity in doubly periodic domains, straight channels and rectangular domains when the free-slip boundary condition is applied. In fact, \mathcal{F}'_{adv} is zero for zero rotation angle because ψ and ζ are both zero at the boundary. However, due to its poor conservation properties (energy and enstrophy), other forms of the Jacobian have been suggested.

AL77 proposed the J_3 form of the Jacobian which conserves energy in doubly periodic domains

$$J_3 = D_x^o (\zeta D_y^o \psi) - D_y^o (\zeta D_x^o \psi) . \quad (4.32)$$

The J_3 Jacobian conserves relative vorticity in doubly periodic domains, but not in presence of boundaries. The boundary terms that arise are relatively easy to pinpoint. They correspond to the value $\zeta D_y^o \psi$ or $\zeta D_x^o \psi$ at locations one grid point away from the boundaries.

It is interesting to note that the J_3 formulation is similar in structure to the advective terms in the SW vorticity equation when the B combination, discussed above, is employed. For example, if we take $u^* = -D_y^o \psi$ and $v^* = D_x^o \psi$, then J_3 can be recast as $J_3 = D_x^o (\zeta u^*) + D_y^o (\zeta v^*)$. The advective term for the B combination in the vorticity equation takes the form of $D_x^o (\bar{q}^y \bar{V}^{xy}) + D_y^o (\bar{q}^x \bar{U}^{xy})$. Hence the two formulations use a divergence form of the advection. Moreover, the viscous term in the SW vorticity equation derived using the δ - ζ stress tensor formulation is similar to the viscous term in the QG equation. Specifically, both take the form of a five-point Laplacian of vorticity. Hence, we expect that the results of the J_3 -QG model should be similar to those of the SW model using the B combination. Unfortunately, there is no straight forward analog between the conventional advection for C-grid and any of the Jacobian operators suggested by AL77. Therefore, we did not note any other possible connections between specific aspects of the QG and the SW numerical formulations.

The last Jacobian formulation we propose

to test is the J_7 and may be given as

$$J_7 \psi = \frac{1}{12\Delta x \Delta y} [\begin{aligned} & \zeta_{i+1,j} (\psi_{i,j-1} + \psi_{i+1,j-1} - \psi_{i,j+1} - \psi_{i+1,j+1}) \\ & - \zeta_{i-1,j} (\psi_{i-1,j-1} + \psi_{i,j-1} - \psi_{i-1,j+1} - \psi_{i,j+1}) \\ & + \zeta_{i,j+1} (\psi_{i+1,j} + \psi_{i+1,j+1} - \psi_{i-1,j} - \psi_{i-1,j+1}) \\ & - \zeta_{i,j-1} (\psi_{i+1,j-1} + \psi_{i+1,j} - \psi_{i-1,j-1} - \psi_{i-1,j}) \\ & + \zeta_{i+1,j+1} (\psi_{i+1,j} - \psi_{i,j+1}) \\ & - \zeta_{i-1,j-1} (\psi_{i,j-1} - \psi_{i-1,j}) \\ & + \zeta_{i-1,j+1} (\psi_{i,j+1} - \psi_{i-1,j}) \\ & - \zeta_{i+1,j-1} (\psi_{i+1,j} - \psi_{i,j-1}) \end{aligned}] \quad (4.33)$$

This more intricate formulation (Arakawa, 1966) is known to conserve both the energy and the enstrophy in doubly-periodic domains. The J_7 Jacobian also conserves relative vorticity in doubly periodic domain, but not in closed domains where complicated boundary terms in \mathcal{F}'_{adv} arise. This formulation is very popular and is adopted in most QG models.

4.4.2 Results

Using J_1 , the solutions are very different for positive and negative values of the rotation angle of the basin. Positive angles are characterized by larger kinetic energy and stronger oscillations of a Rossby basin mode (curve b of Figure 4.9), which appears to be unstable at low resolution. However, with increasing resolution (curves d-f of Figure 4.9), the kinetic energy for both positive and negative angles seems to converge to the value of kinetic energy for the non-rotated basin cases (curves a,d). Nonetheless, we prefer to discard this formulation of the Jacobian for the rest of the discussion, due to its low level of accuracy at moderate resolutions.

On the other hand, solutions using J_3 and J_7 appear stable and converge reasonably well with increasing resolution to the same value of kinetic energy, for both rotated and non-rotated basins (Fig. 4.10). Therefore, this results contrasts with those of the SW model for which the convergence was only

obtained for the B combination. The QG model appears to be less sensitive to grid rotations and advective formulations.

In terms of vorticity budget, we are interested in the behavior of the advective contribution, \mathcal{F}_{adv} , with increasing resolution for the J_3 and the J_7 Jacobians. Specifically, we are interested in how the convergence order for \mathcal{F}_{adv} differs in the QG model compared to the SW model. As mentioned, \mathcal{F}_{adv} is made of two independent contributions, \mathcal{F}'_{adv} and \mathcal{F}_c . \mathcal{F}'_{adv} depends directly on the Jacobian formulation but \mathcal{F}_c does not. Figure 4.11 shows the convergence of \mathcal{F}'_{adv} in rotated and non-rotated basins for the two considered Jacobians. \mathcal{F}'_{adv} is close to second order in non-rotated basins for both Jacobians. At 30° rotation, however, the convergence order is closer to unity for J_3 but second order for J_7 .

We now analyze the convergence order for \mathcal{F}_c , the second contribution to \mathcal{F}_{adv} . Figure 4.12 shows the convergence for \mathcal{F}_c in rotated and non-rotated basins under J_3 and J_7 . The results appear independent of the Jacobian formulation, as expected. The convergence order is however unity, in contrast with results for \mathcal{F}'_{adv} . This result comes readily from the traditional treatment of the β term. The proof is given in a square domain:

$$\begin{aligned} \beta \sum_{ij \in \delta\Omega_\zeta} D_x^o \psi \Delta x \Delta y = \\ \beta \sum_j \sum_{i=2}^{i=n_x-1} \frac{\psi_{i+1} - \psi_{i-1}}{2\Delta x} \Delta x \Delta y = \quad (4.34) \\ \beta \sum_j \frac{\psi_{n_x-1} - \psi_2}{2} \Delta y, \end{aligned}$$

since $\psi_1 = \psi_{n_x} = 0$, by definition of no-permeability. The west-east asymmetry due to the beta effect imposes that $\psi_{n_x-1} = a\psi_2$ with $0 < a < 1$ and all other parameters kept constant. The factor, a , represents the ratio of the velocity along west and east coastline. Because ψ_{n_x-1} and ψ_2 converge linearly to zero with increasing resolution, the beta contribution cannot have a better convergence rate than one. In absolute value, \mathcal{F}_c is also larger than \mathcal{F}'_{adv} . Therefore, \mathcal{F}_{adv} suffers primarily from the low convergence rate of the beta contribution, \mathcal{F}_c . One can ask whether we can get a better convergence order by

including the planetary vorticity, βy in the Jacobian instead of treating it separately ($J(\psi, \zeta + \beta y)$ instead of $J(\psi, \zeta) + \beta \partial_x \psi$). We conducted this experiment with the best advective formulation, the J_7 . However, convergence order of \mathcal{F}_{adv} is again unity and errors are very similar to the previous case (not shown).

One last point we would like to make is related to similarities mentioned above, between the J_3 -QG and the B combination of the SW model. Figure 4.14 shows \mathcal{F}'_{adv} , \mathcal{F}_c and \mathcal{F}_{adv} with increasing resolution for J_3 and under -30° rotation angle. \mathcal{F}'_{adv} is negative, goes through an minimum and, then increases toward zero, whereas \mathcal{F}_c is positive and decreasing to zero. Hence, \mathcal{F}_{adv} appears to go through a pool of negative values, just as the B results showed. This contrasts with results using J_7 for which \mathcal{F}'_{adv} takes positive values for both negative and positive rotation angle (not shown).

To conclude, except for the J_1 Jacobian, the QG model is less sensitive to the basin rotation, in contrast with results for the SW model. Convergence orders for the advective flux of vorticity, \mathcal{F}_{adv} , on the other hand, are order 1 or less—comparable to what was found for the SW simulations. In the QG case, this low order of convergence is related to the beta contribution, \mathcal{F}_c . Using J_7 , $|\mathcal{F}_{adv}|$ varies between 5% (high resolution) and 20% (coarse resolution) of the wind input depending on the rotation angle. These results are somewhat better than those obtained in the SW simulations.

4.5 Discussion and Conclusion

Due to their fractal nature, realistic coastlines have features down to the model resolution. While the ultimate goal would be to correctly account for such features in models, a less stringent test is that models should be able to deal with simple geometries, in a manner that is not sensitive to artificial steps introduced by the discretization. Such was the study of AM, based on free-slip single gyre Munk experiments. As we noted

that there was an inconsistency in the discretized vorticity budget for the C-grid shallow water model, we decided to revisit the AM results in terms of global vorticity budgets with varying resolution. Our goal was to investigate the influence of the formulation of the advective and viscous terms on the model vorticity budget and the overall strength of the gyre.

AM showed that the conventional viscous stress tensor formulation was inappropriate in the rotated basin case, for steps occurring along the coast. Moreover, they made use of an alternative stress tensor formulation (called herein δ - ζ tensor) and showed improved results. We analyzed further the difference between conventional and δ - ζ tensor formulation along with two different formulations of the advection in the momentum equations in term of global vorticity budgets with varying resolution. One observation is that the results with the δ - ζ stress tensor depend strongly on the formulation of the advection, as the conventional advection formulation leads to instability (the D combination). Therefore, the formulation of the advection seems equally important in explaining the AM results. In terms of vorticity budgets, all combinations seem to be ill-behaved except for the enstrophy conserving advection and the δ - ζ tensor (the B combination). For this combination, the convergence order for \mathcal{F}_{adv} is about unity, following the truncation order of the vorticity when derived from second order velocity.

For the QG model, the overall circulation is less sensitive to the rotation of basin for all Jacobians we tried. In order of increasing accuracy, J_1 gives the lowest level of accuracy (showing even signs of instability at low resolution), followed by J_3 and then J_7 . The best convergence order for \mathcal{F}'_{adv} was obtained by using the J_7 Jacobian and was about 2, for all rotation angles. The beta contribution, \mathcal{F}_c , is independent of the formulation of the Jacobian. Its convergence order is very close to unity and its magnitude is usually larger than that of \mathcal{F}'_{adv} . Therefore, most of the discrepancy between the real and the model vorticity budgets is concentrated in the beta contribution at sufficiently high resolution. Hence, in order to make accurate vorticity budgets, it follows that the beta contribution should be more accurately computed. One possibility is to increase the order of the fi-

nite differencing operator for the beta term, $\beta \partial_y \psi$. Finally, the hypothesis that the J_3 -QG model would give similar results compared to the enstrophy conserving advection and the δ - ζ tensor C-grid model was verified.

From the general point of view of computing vorticity budgets from finite difference models, both QG and C-grid models show the same relatively slow convergence order (about unity) of the discrepancy with increasing resolution between the real and the model vorticity budgets. For the range of resolution considered, and depending on the model type (SW or QG), numerical formulations and the rotation angle (or more generally, basin geometry), this error can be estimated to vary between 5% to 50%.

As for the general accuracy of FD models in presence of steps for wind-driven circulations under free-slip, the rotated square basin experiments show that the B combination for the C-grid model and the J_3 or J_7 for QG model give satisfactory results. We were not able to get satisfactory results out of a conventional B-grid model, though. This spatial staggering of velocity and elevation does not seem to suit very well the free-slip boundary condition, even in presence of straight walls. The next chapter considers the more general case of a smoothly varying coastline for the Munk problem.

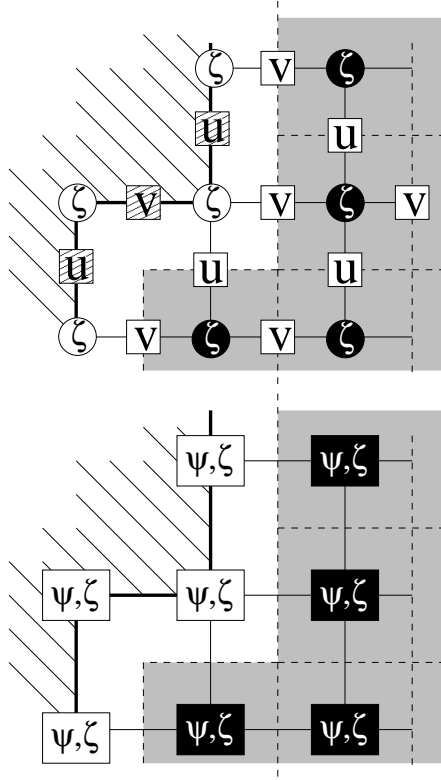


Figure 4.1: Locations of variables near a step for the SW C-grid model (left panel) and for the quasi-geostrophic (QG) model (right panel). For the SW model, dashed squares are the boundary normal velocity nodes, white disks are the vorticity nodes where the relative vorticity is specified to be zero and black disks are the vorticity nodes for which a discretized vorticity equation can be written. In grey is the region delimiting the vorticity budget domain. This region does not extend to the model boundary. Instead, there is an half cell band around the boundary (left in white) where we cannot derive any budget. A similar problem exists for the QG approximation.

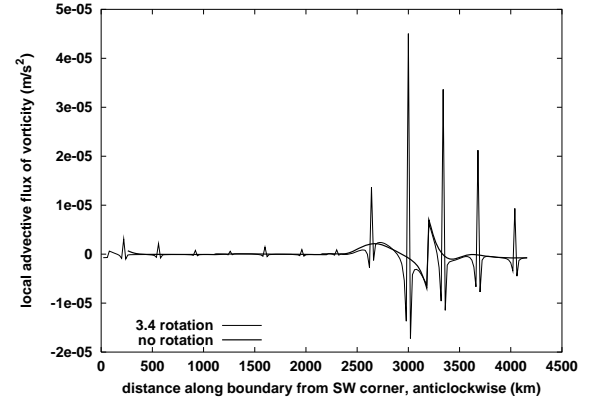


Figure 4.2: Local advective flux along the boundary ($\mathbf{C} \cdot \Delta \mathbf{l} / \|\Delta \mathbf{l}\|$) at 20 km resolution in a square basin for the entrophy conserving formulation of the advection using the B combination of Table 4.1. The heavy-lined curve is for no rotation of the basin, the light-lined curve is for a small angle rotation of the basin (3.4°) with respect to the grid. Due to the rotation angle, 4 steps occur along each side of the square and cause abrupt changes in the local advective flux.

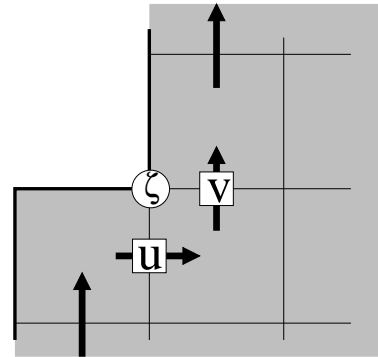


Figure 4.3: Northward flow past a forward step. The shaded area is the model domain. We consider only the two momentum nodes for which the $\delta\text{-}\zeta$ formulation differs from the conventional formulation. The ζ -point at the tip of the continent has $(i, j + 1)$ indices. Arrows indicate direction of the flow.

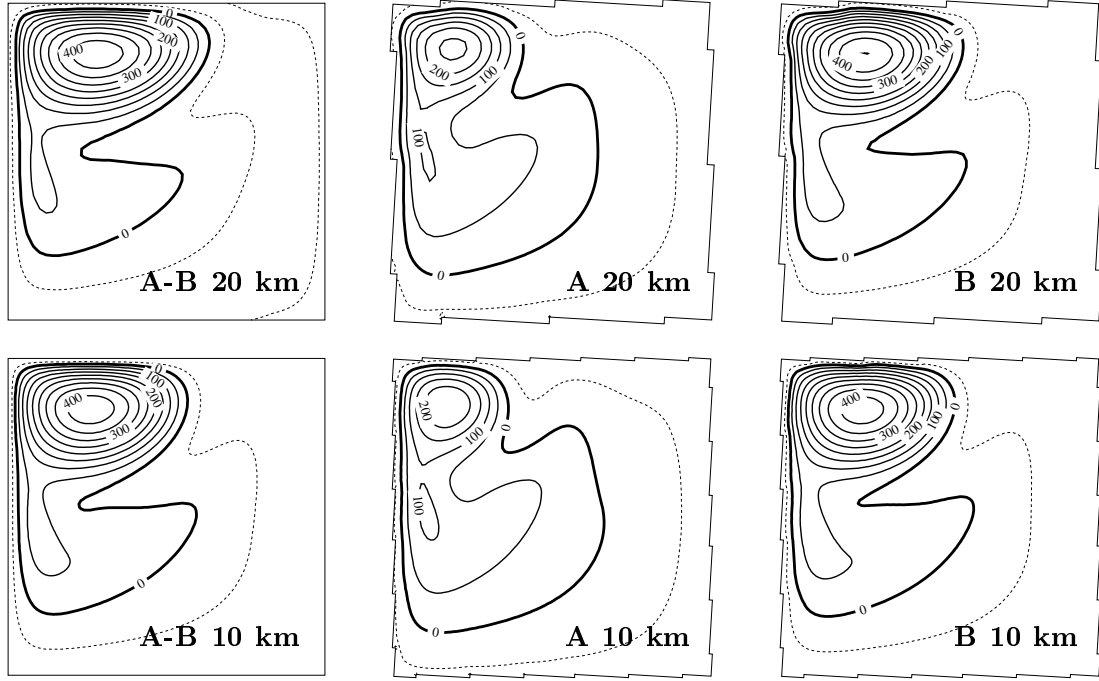


Figure 4.4: Elevation fields in meters after a 6 year spin-up for 20 km and 10 km resolution. Shown are results from the A and B combination (Table 4.1) with or without a 3.44° rotation angle of the basin. Note that the B case tends to resemble the A-B case with no rotation, but not the A case.

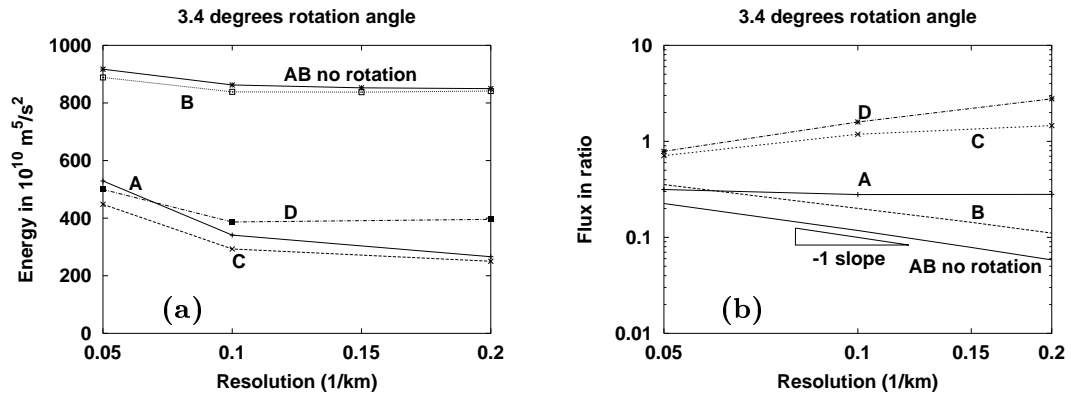


Figure 4.5: (a) Kinetic energy after spin-up and (b) ratio of \mathcal{F}_{adv} to \mathcal{F}_i for the four combinations. Results are shown for a 3.4° rotation angle of the basin. The A-B (no rotation) curve is also plotted for comparison.

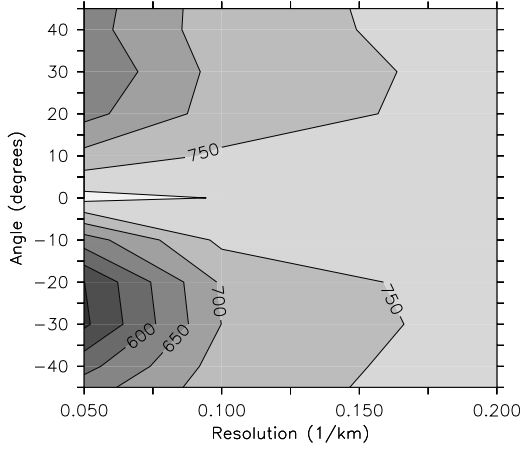


Figure 4.6: Kinetic energy after spin-up for the B combination in $10^{10} \text{ m}^5/\text{s}^2$.

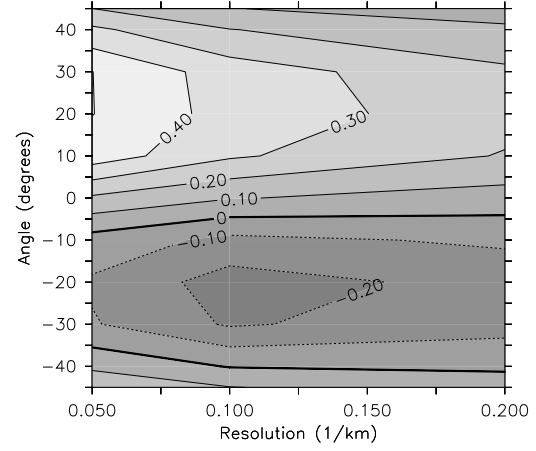


Figure 4.7: Ratio of \mathcal{F}_{adv} to \mathcal{F}_i for the B combination.

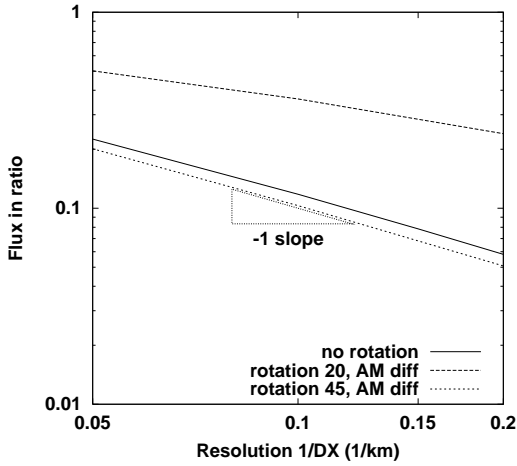


Figure 4.8: Convergence of \mathcal{F}_{adv} with resolution for 0° , 20° , 45° rotation angle for the B combination.

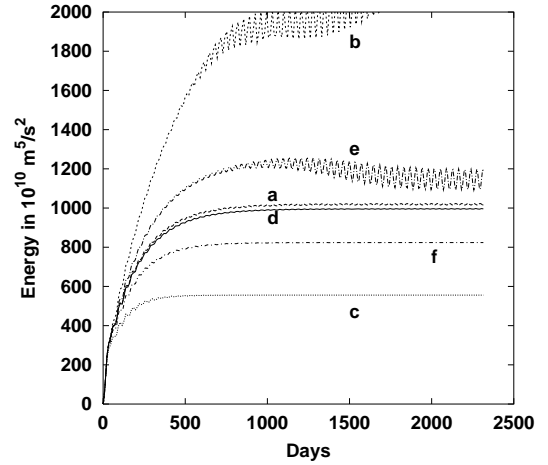


Figure 4.9: Kinetic energy during spin-up for six runs using the J_1 Jacobian: (a), 0° angle at 20 km resolution; (b), 30° angle at 20 km; (c), -30° angle at 20 km; (d), 0° angle at 10 km; (e), 30° angle at 10 km; (f), -30° angle at 10 km;

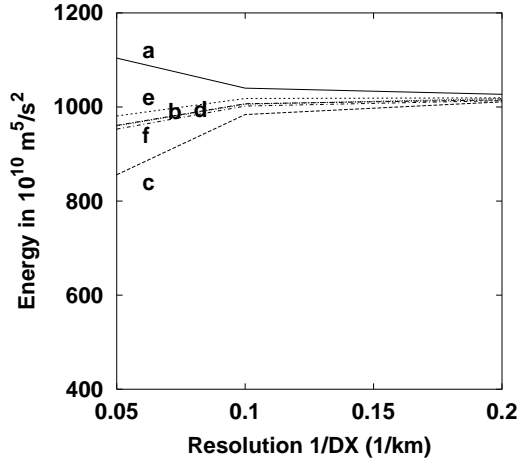


Figure 4.10: Kinetic energy after spin-up for (a) J_3 at 0° rotation, (b) J_7 at 0° , (c) J_3 at 30° , (d) J_7 at 30° , (e) J_3 at -30° , (f) J_7 at -30° .

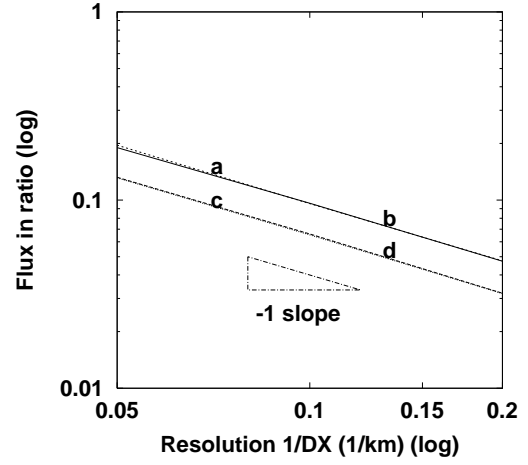


Figure 4.12: Ratio of \mathcal{F}_c to the wind input. (a-d) as described in Fig. 4.10.

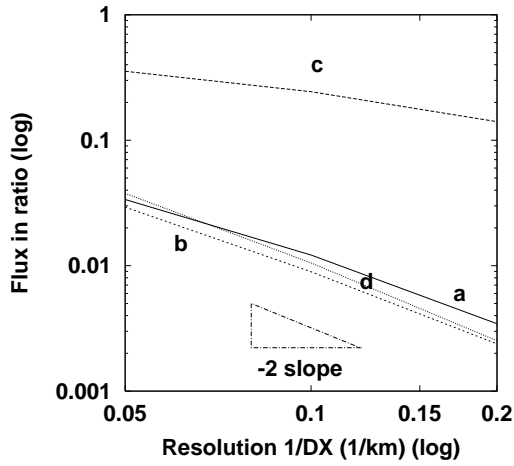


Figure 4.11: Ratio of \mathcal{F}'_{adv} to the wind input for (a) J_3 at 0° rotation, (b) J_7 at 0° , (c) J_3 at 30° , (d) J_7 at 30° .

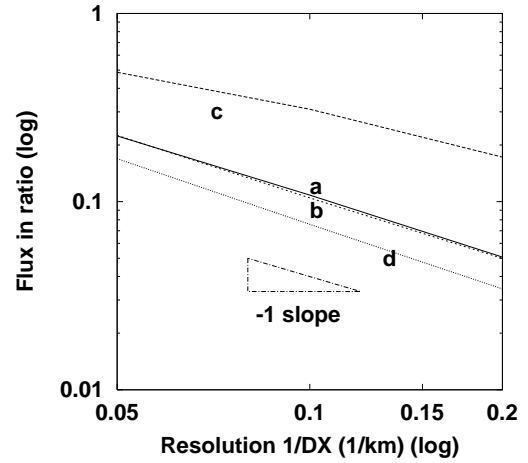


Figure 4.13: Ratio of $\mathcal{F}_{adv} = \mathcal{F}'_{adv} + \mathcal{F}_c$ to the wind input. (a-d) as described in Fig. 4.10.

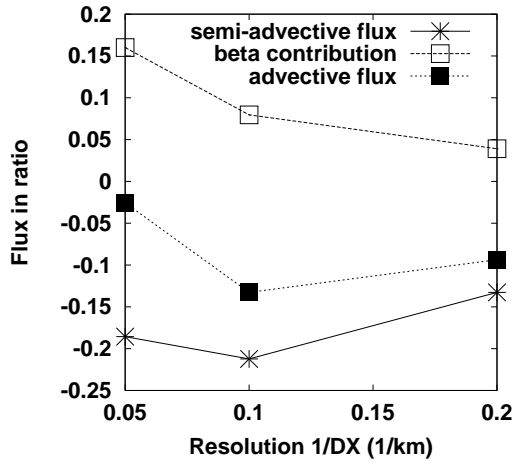


Figure 4.14: Semi-advective flux, \mathcal{F}'_{adv} , and beta contribution, \mathcal{F}_c , to the vorticity budget for the J_3 Jacobian at -30° rotation angle. $\mathcal{F}_{adv} = \mathcal{F}'_{adv} + \mathcal{F}_c$ is negative at this rotation angle, similarly to results obtained for the B combination.

Chapter 5

Single Gyre Circulation in Irregular Domains

In this chapter, we explore the issue of the inertial runaway (to be defined below) for the single gyre Munk problem with free-slip boundary conditions from two perspectives: scaling arguments and numerical simulations using the spectral element model. In the previous chapters, we investigated the accuracy of different numerical methods and found that the spectral element (SE) model offers high accuracy in irregular domains and nonlinear flows, whereas the other methods present various limitations. This chapter is both an application of the SE method and a contribution to the understanding of the runaway problem.

5.1 Review of the Single Gyre Problem with Free-Slip Boundary Conditions

As stressed by Pedlosky (1996), the single gyre (as opposed to the double gyre) Munk circulation faces the unique challenge that, in terms of vorticity budget, all the wind input has to be fluxed out of the domain by means of the viscous flux in order to yield a steady or statistical mean solution. At equilibrium, the vorticity budget becomes:

$$\oint \frac{\tau}{h} \cdot d\mathbf{l} + \nu \oint \frac{\partial \zeta}{\partial n} dl = 0 . \quad (5.1)$$

To be precise, we refer to the single subtropical (anti-cyclonic) gyre problem in the north-

ern hemisphere for the single gyre problem. In that particular case, the wind input to the vorticity budget, the first term in (5.1), is negative. Although the single gyre problem is extreme in that the vorticity input is one-signed, most people consider the double gyre problem (i.e., when the forcing integrates to zero) to be a special case. There is typically a net vorticity input of one sign or another into the ocean, and therefore, in the generic case, the system needs to dissipate some vorticity. The single gyre problem is certainly extreme, but it is argued after that some of its characteristics make this problem even more interesting and challenging. Moreover, for the single gyre forcing, there is a strong correspondence between the difficulty of balancing the vorticity budget and the strength of the overall circulation, since the second term in (5.1) links the magnitude of the eddy-viscosity, ν , to the importance of the normal derivative of the vorticity. This derivative is related to the strength of the circulation. As ν is reduced, the integral of the derivative must be augmented in proportion to yield an equivalent balance. The difficulty of balancing the vorticity budget is also dependent on the dynamical boundary condition. The vorticity balance is more difficult to achieve when free-slip boundary conditions are employed, as opposed to no-slip. Using free-slip conditions (see Chapter 1), the vorticity at the boundary is zero along straight walls and, under no-slip, it can reach large positive values, whereas the vorticity is mainly negative in the interior due to the negative wind input. Therefore the normal derivative of the vorticity, $\partial \zeta / \partial n$, is much higher in the no-slip case than in the free-slip case, fluxing more easily the vorticity through the boundaries.

This enables gyres under no-slip to achieve weaker circulations compared to gyres under free-slip.

The importance of the nonlinear terms with respect to the viscous forces is commonly scaled by the Reynolds number, Re . For Munk circulations, it is more convenient to relate the Reynolds number to the dynamics of the boundary layer (see Pedlosky). Re is therefore defined as

$$Re = \left(\frac{\delta_I}{\delta_M} \right)^3 \quad (5.2)$$

where δ_M and δ_I are respectively the Munk and inertial numbers. They are defined as

$$\delta_M = \left(\frac{\nu}{\beta L^3} \right)^{1/3} ; \delta_I = \left(\frac{V_{Sv}}{\beta L^2} \right)^{1/2} , \quad (5.3)$$

where V_{Sv} is the Sverdrup velocity and L is the width of the basin. In scaling arguments, V_{Sv} is usually taken as the maximum value observed in the interior away from the boundary layers. We prefer to use the mean value of the V_{Sv} which can be obtained by integrating the Sverdrup relation over the whole domain except for the boundary layers/footnote This choice is motivated by the quantitative estimations of coming Section 5.4 which are based on vorticity budgets arguments and are better approximated by using the mean rather than the maximal Sverdrup velocity. There is also a *a posteriori* and cosmetic argument related to the fact that the transition between the Sverdrup interior solution to a Fofonoff-type interior solution (explained at the end of this paragraph) occurs at $Re \sim 1$ if a mean Sverdrup velocity is chosen but will occur at $Re \sim 4$ if the maximum Sverdrup velocity is chosen.:

$$V_{Sv} = \frac{1}{\beta L^2} \oint \frac{\tau}{h} \cdot d\mathbf{l} . \quad (5.4)$$

For the wind forcing under consideration, $\beta = 1.6 \times 10^{-11} \text{ m}^{-1}\text{s}^{-1}$ and assuming that $h \sim H$ along the walls, the mean V_{Sv} is approximately $1.25 \times 10^{-2} \text{ m/s}$. This choice will lead to smaller values of Re when compared to other authors' results. Another important remark concerns the physical meaning of these two numbers. δ_M and δ_I , multiplied by the width of the basin, L , yield respectively the thickness of the Munk and inertial layers. These are the lengths at which

the vorticity varies in order to yield a balance between the viscous terms and the beta term, and a balance between the advection and the beta term, respectively. The Munk layer exists only for weak nonlinear terms. When these nonlinear terms are large enough ($Re \sim 1$ and beyond), the inertial boundary layer prevails along the western boundary. In such a case, the Munk layer is replaced by a viscous sublayer whose thickness is given by $L\delta'_M$ where

$$\delta'_M = \frac{\delta_I}{\sqrt{Re}} . \quad (5.5)$$

δ'_M comes from the evaluation of the balance between the advection and the viscous terms. These nonlinearities, and the presence of the inertial layer, introduce more difficulties in achieving a vorticity balance. For instance, in the absence of eddies, the inertial layer inhibits the transport of vorticity from the interior to the walls because, there, the streamlines and absolute vorticity contours are nearly parallel. Therefore, the negative input of vorticity in the interior of the ocean cannot be easily fluxed out. This favors an even more inertial and energetic interior flow and, when the Reynolds number is beyond a critical value, a Fofonoff-type gyre develops (as opposed to a Sverdrup interior) with unrealistically large speeds of the order of 50 m/s. This is the so-called inertial runaway problem. According to Pedlosky, this scenario also occurs in the presence of no-slip boundary conditions, the no-slip only retarding the occurrence of the jump to the highly energetic branch (where the Fofonoff-type gyre lies). Moreover, he states that the inertial runaway is not just a feature of steady solutions but is prone to appear in unsteady solutions, as well.

Indeed, Ierley and Sheremet (1995) observe this runaway scenario for the free-slip condition in steady and unsteady circulations in rectangular domains for single gyre forcing. Under free-slip, there is no difference between unsteady and steady solutions because the eddy activity is very weak in unsteady solutions. However, no-slip steady and unsteady solutions are usually different. Nonetheless, Sheremet *et al.* (1997) demonstrate that the same runaway problem occurs in rectangular domains when the no-slip condition is applied to the western and eastern walls (repeating the experimental setup of Bryan, 1963). They note that,

after the unsteady and steady solutions first depart, the strength of the circulation does not increase with increasing Reynolds number because the eddies efficiently remove the excess of vorticity produced in the boundary layer. However, past a critical Reynolds number, they note that the mean circulation strengthens again, the eddies being no longer efficient in removing the excess of vorticity. Veronis (1966) for the single gyre and Primeau (1998) for the double gyre demonstrate that the runaway scenario is also observed for bottom friction only models. Pedlosky (1996, p87) and Ierley and Sheremet are convinced that their runaway scenario is universal, based on their experience with stratified quasi-geostrophic (QG) unsteady simulations in idealized geometries. According to them, no convergence of the statistical steady state can be achieved with increasing Reynolds number, whatever the type of boundary conditions. Of course, the latter argument conflicts with our day-to-day experience. As far as we know, the Gulf Stream circulation has not blown up! Nonetheless, these authors bring strong numerical evidences in favor of their arguments. Therefore, where is the flaw ?

From the perspective of time-dependent simulations, one aspect of the results of Sheremet *et al.* (1997) remains questionable. This is related to the use of no-slip boundary conditions in unsteady solutions. The fact that no-slip circulations are prone to barotropic instabilities cannot be underestimated from the point of view of the inertial runaway. These instabilities may be sufficient to produce eddies which would transport the vorticity through the inertial layer to the viscous sub-layer, where it can be fluxed across the wall. However, no-slip circulations are very demanding in terms of computer resources and, therefore, the issue is still unresolved. One possibility is that we still need more resolution (to achieve larger Re) in unsteady no-slip circulations. A second possibility is related to the use of overly idealized geometries in the aforementioned results. Finally, a third possibility is that the models used in those results are too simple. From this last point of view, we may lack certain physical processes which are important for the downward cascade of energy. In favor of this argument, Scott and Straub (1998) noted that, under no-slip, the Rossby number (which scales the nonlinear terms to

the Coriolis forces) increases quickly with increasing Reynolds number. Since the QG approximation applies only for small Rossby number, R_o , large R_o means that the rather inexpensive QG models cannot be used for even such idealized experiments, but have to be replaced by, at a minimum, more costly shallow water models.

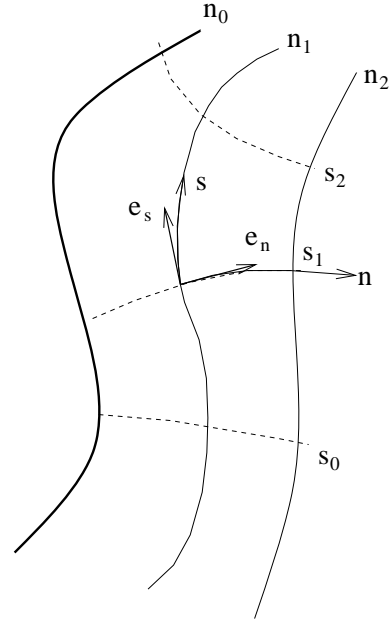


Figure 5.1: Notation corresponding to the curvilinear coordinates.

In favor of these three arguments, recent high resolution (1/4 to 1/64 degree) simulations of the Atlantic were conducted using the MICOM model (i.e., an isopycnal primitive equation model) and showed that the mean circulation converges to a more and more realistic state with increasing Reynolds number (Hulburt and Hogan, 2000). The eddy-viscosity was lowered from 100 to 3 m^2/s . The problem with this kind of experiment is that it is difficult to distinguish which physical processes or technical details are necessary to obtain the convergence with increasing Reynolds number. We believe that one important distinction comes from the geometry. Theoreticians typically focus on rectangular domains whereas primitive equations models are generally run in more realistic geometries. Irregular geometries may be sufficient by themselves to provide the necessary source of eddies in order to get weaker and more realistic circulations at high

Reynolds number. An irregular geometry—especially irregular along the western coastline where the currents are the strongest—may also provide stronger interactions between geostrophic and ageostrophic modes, and hence may facilitate a forward energy cascade. The latter process is absent from idealized early experiments which are based on the QG equation. Thus, the shallow water equations are a good starting point for our investigation. Furthermore, we believe that having irregular boundaries is more important than the choice on the type of dynamical boundary conditions. In the context of the double gyre forcing of the Munk problem, Scott and Straub (1998) show that the increase in kinetic energy of non-symmetrical steady solutions and time-dependent mean solutions tends to level off as the Reynolds number increases for the two boundary conditions. Therefore, the idealized double gyre experiment where the wind input to the vorticity budget cancels may exhibit less severe inertial runaway. Contradictory evidence against inertial runaway has yet to be found in single gyre circulations where the wind input of vorticity is single signed. Therefore, we will conduct experiments using the free-slip boundary condition since many evidences exist for a robust inertial runaway under free-slip in rectangular basins. In fact, under the free-slip boundary condition, irregular boundaries are the only way to produce positive vorticity which is essential to the production of eddies. The vorticity can be expressed using curvilinear coordinates following the wall as

$$\zeta = \frac{\partial v_s}{\partial n} - \frac{\partial v_n}{\partial s} + \frac{v_s}{R_s} - \frac{v_n}{R_n}, \quad (5.6)$$

where (s, n) are respectively the coordinate along and normal to the wall, v_s and v_n are the velocity components respectively along s and n and R_s and R_n are the respective radii of curvature of the axes along the wall and normal to the wall. (notation is shown in Figure 5.1). Right at the wall and under the free-slip boundary condition (as defined in Chapter 1), the equation reduces to

$$\zeta = \frac{v_s}{R_s}. \quad (5.7)$$

If the velocity at the wall is close to 1 m/s and the radius of curvature along the wall is of the order of the 10 km, ζ is of the order

of 10^{-4} s^{-1} , that is, of the order of f_0^{-1} . One way to evaluate the Rossby number is to measure the ratio of ζ/f_0 . Therefore, if the radius of curvature is of the order of 10 km, we can obtain Rossby numbers of the order of unity; that is, well beyond the range for which the QG approximation applies. This stresses again the need to use the primitive equations. 10 km is also somewhat below the radius of deformation for the first baroclinic mode given the value of the parameters we use ($L_R \sim 31 \text{ km}$). This means for instance that Kelvin waves may encounter difficulties in going around such geometrical features.

5.2 Model Selection and Experimental Design

In order to test these arguments, we consider the following experiment. The set-up consists of wind-driven circulations in five different geometries (Figure 5.2). The first is a circular geometry with the radius given by $L_c = 500 \text{ km}$. The second is a perturbation of the first geometry by the addition of a wavy pattern along the coastline in the form of a sine wave. We choose the wave length to be a 1/16 of the perimeter. The amplitude of the sine wave from a crest to a trough is 12.5 km. The third geometry is the same one except that the amplitude of the sine perturbation is 25 km. The amplitude for the fourth and the fifth is respectively 50 and 100 km. The radius of curvature was computed using the simple relation:

$$\frac{\partial \mathbf{e}_s}{\partial s} = -\frac{1}{R_s} \mathbf{e}_n \quad (5.8)$$

where \mathbf{e}_s and \mathbf{e}_n are the orthonormal unit vectors associated with the directions s and n . For a sine wave given by $y = h_0 \sin(kx)$ the minimum radius of curvature is given by

$$\frac{1}{R_s} = h_0 k^2 \quad (5.9)$$

¹Using Pedlosky's definition for free-slip instead of the current one, as defined in Chapter 1, the relative vorticity can reach larger values. If a fluid parcel passes east of an obstacle and flows anticlockwise around it in a steady state, we have $\partial u / \partial y < 0$. Using the mass conservation equation, this leads to $\partial v / \partial x > 0$. Therefore, according to (5.6), $\zeta > V / R_s$, i.e., the vorticity is larger.

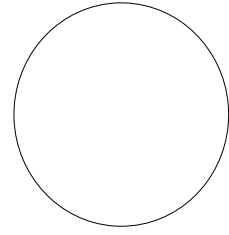
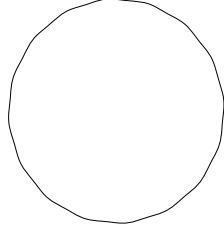
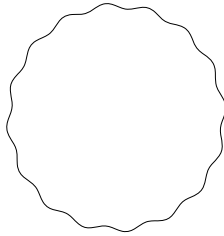
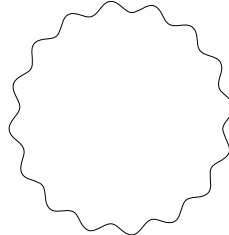
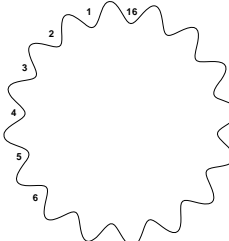
**I****II****III****IV****V**

Figure 5.2: The five geometries used for our application of the SE method. The circle is deformed by super-imposition of a coastal oscillation of the form of a sine wave. For Geometry V, we label the bumps for later reference starting from the first bump west of the north-south axis passing through the center of the basin and we then proceed anticlockwise. The same labeling applies for the other

In the context of the circular geometry, we can correct the radius by using the relation:

$$\frac{1}{R_s} = h_0 k^2 + \frac{1}{L_c} \quad (5.10)$$

Hence, the minimum radius of curvature for the second geometry is about 160 km and 80 km, 40 km and 20 km for the third, fourth and fifth geometries. We use three values of the eddy-viscosity ($\nu = 700, 300, 100 \text{ m}^2 \text{ s}^{-2}$). The wind-forcing is the same as applied in the previous chapter for single gyre Munk problem. The Reynolds boundary number ranges therefore from 0.5 to 3.5. For comparison, Scott and Straub (1998) reached impressive values of about 35 for double gyre steady circulations with a QG model. In contrast, our maximum achieved value of $R_e = 3.5$ is lower. However, in the context of unsteady solutions in irregular geometries using a shallow water reduced gravity model and due to our definition of V_{Sv} , this can be considered a high value. The inertial layer width is about 28 km whereas the viscous sublayer width varies from 40 km to 15 km. Therefore, we expect that the processes are mostly nonlinear. Since we are interested in the mean states of the circulation, when possible, we performed six year averages of the fields after a statistical steady state has been reached. This period is limited by computer resources. It is a bit short since six years represent only twice the time for a Rossby wave to cross the basin. However, we do not believe that these results would significantly differ for longer averaging period.

We first compare the results from the C-grid FD model using the promising $\delta\text{-}\zeta$ stress tensor formulation and the enstrophy conserving scheme (the B combination of Section 4.2.2) with those of the C-grid using the same advective scheme and the conventional stress tensor formulation (the A combination of Section 4.2.2). Figure 5.3 shows the elevation fields after a 3 year spin-up for $\nu = 100 \text{ m}^2 \text{ s}^{-1}$. The circulation of the B combination is much more inertial than the circulation of the A combination. Furthermore (but not shown), the vorticity fields are very noisy in both cases. The B combination run is stopped shortly after the third year of simulation because of the depletion of the water column along the boundaries ($h < 0$). Figure 5.4 shows the total energy for both

combinations and the SE model. We consider the SE results to be the “truth”. We note that the A combination is too dissipative and that the B combination is not dissipative enough. The A combination is for this geometry the combination closest to the SE results. That the B combination is not dissipative enough can be related to the fact that this particular configuration of the C-grid model specifies the vorticity to be zero at the wall and therefore, does not take into account the influence of the radius of curvature. Therefore, although the B combination was successful in the presence of steps in a rectangular geometry (where free-slip implies $\zeta = 0$), this combination is no longer successful in the general case of an irregular geometry where the vorticity can be non-zero at the walls.

A better way to implement the boundary condition in the FD model might be to take into account the curvature of the boundary, as we do in the SE model. This would require computing for each velocity node close to the boundary a series of coefficients associated to nearby velocity points in order to extrapolate the normal derivative of the tangential velocity along the wall (i.e., a generalization of the off-centered two point operator used in Section 2.2.2 for enforcing free-slip along straight walls.) The C-grid however does not easily allow for such an implementation. One limitation comes from the fact that the velocity components are not discretized at the same location. This implies interpolations back and forth from the global coordinates to the local curvilinear coordinates of the components of velocity. This sort of two-way interpolation is damaging to the overall accuracy. Leakage of mass from the computational domain is also a possibility that could affect the accuracy.

We therefore need a model which represents more accurately the effects of the walls. The SE model seems to be a good candidate. A second order FE model, which satisfies the LBB stability condition and which is based on the Eulerian time description, may be successful in this application as well. However, from Chapter 3, the SE model would offer a robust and faster convergence with increasing resolution at a more reasonable cost.

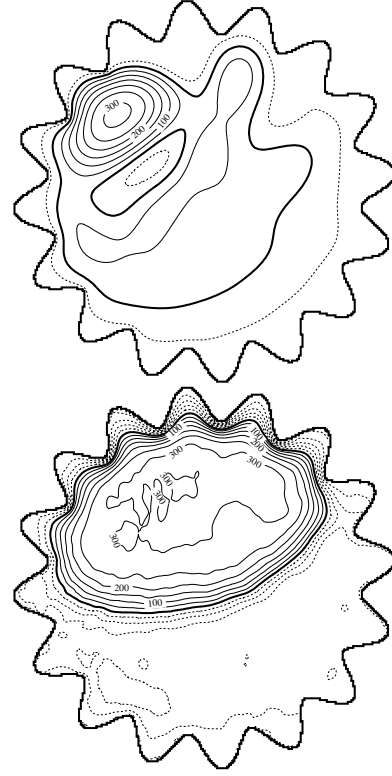


Figure 5.3: Elevation fields in the Geometry V for the C-grid model after 3 years of spin-up. On top, the A Combination, at bottom, the B combination.

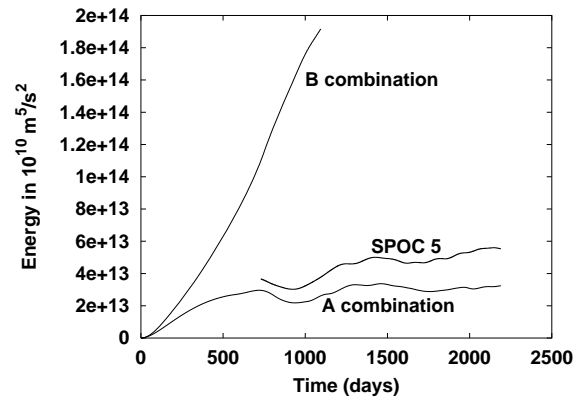


Figure 5.4: Total energy during spin-up for the A and B combinations of the FD C-grid model and for the SE model at $n_c = 5$ (SPOC 5) in Geometry V. $\nu = 100 \text{ m}^2\text{s}^{-1}$.

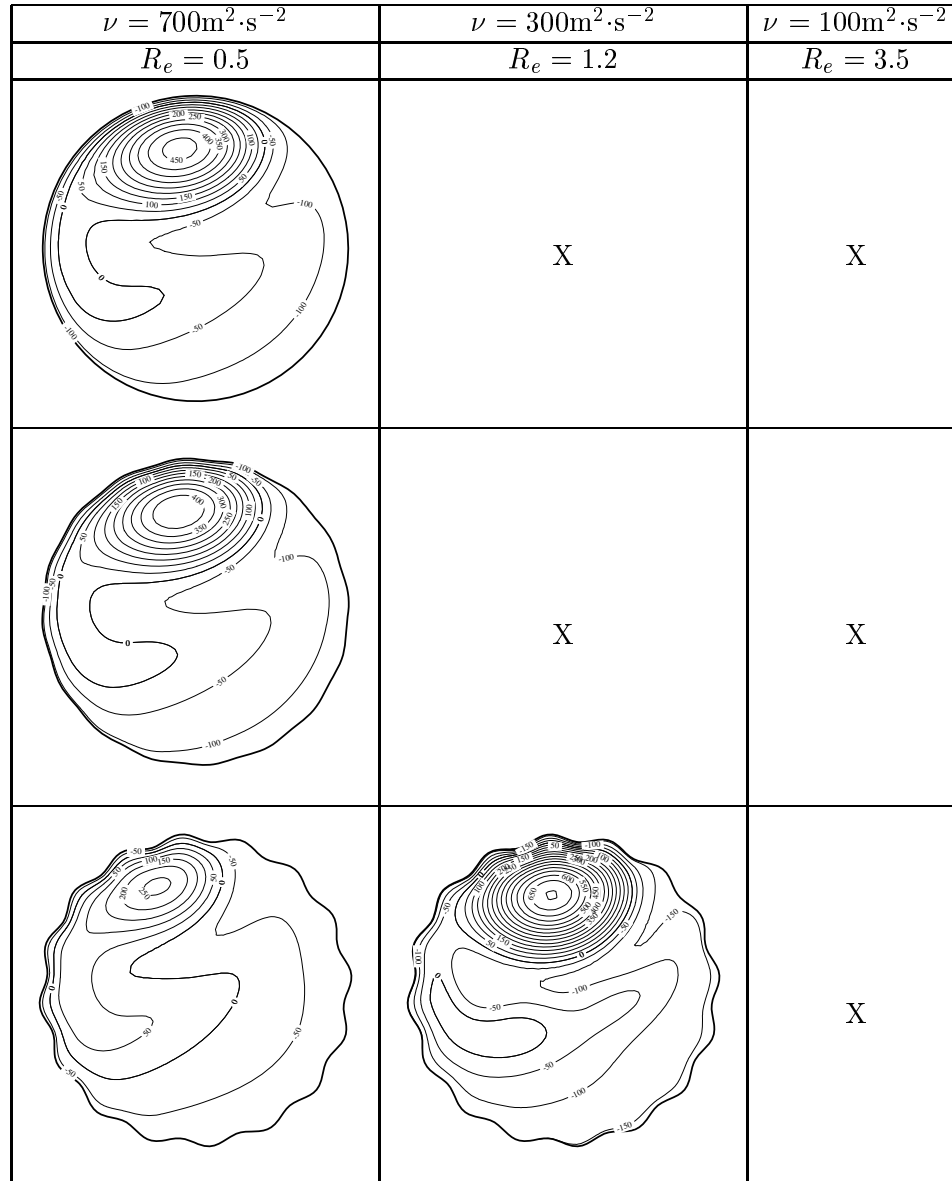


Figure 5.5: Mean elevation fields for the five geometries using the SE model. When no steady state could be reached because the solution jumps to the high energetic branch, an 'X' is drawn instead.

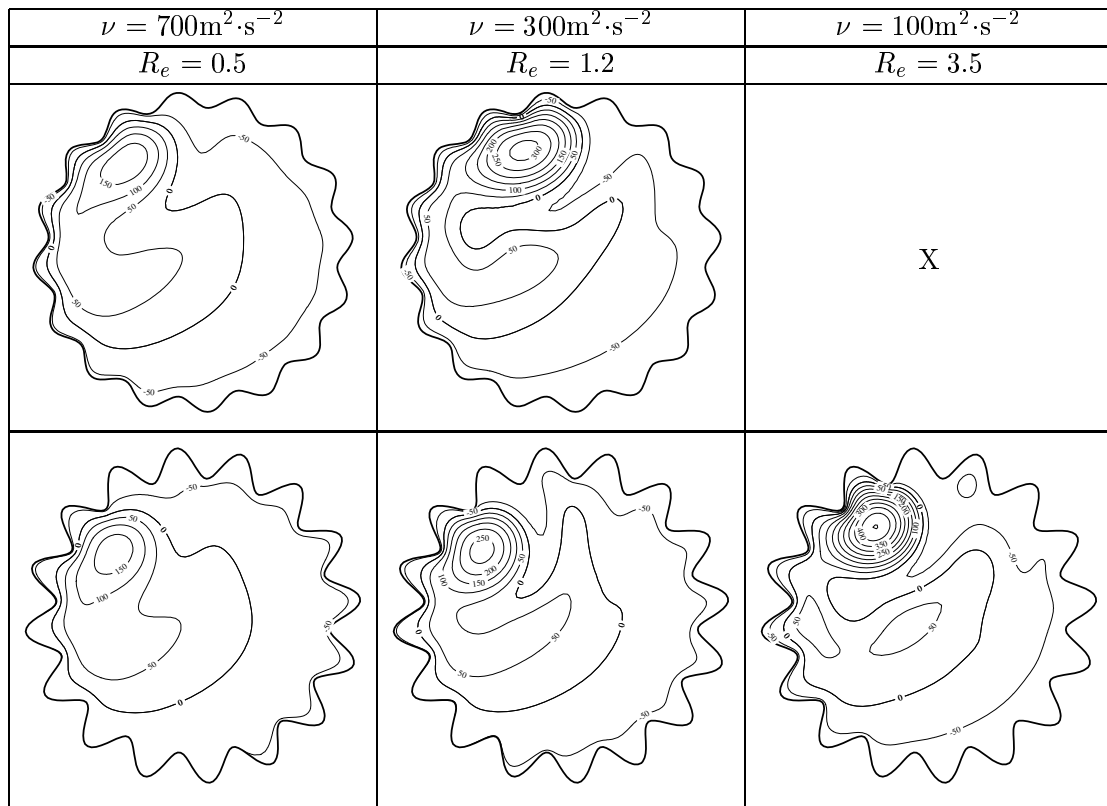


Figure 5.5 continued.

5.3 Results

5.3.1 General Results for all Geometries

In Figure 5.5, we show the different statistical mean circulations obtained in the five attempted geometries. An “X” marks when a statistical mean could not be reached. Such is the case when the solution jumps to the high energy branch. When this occurs, the sea level tilt implied through geostrophic balance by the unreasonably strong currents quickly leads to zero layer thickness, at which point the integration is halted. This happens for the intermediate and high R_e in the Geometry I and II and for high R_e in Geometries III and IV. We achieve a reasonable statistical mean for all considered R_e in Geometry V. As the Reynolds number is increased, the recirculation tends to move eastward and northward and strengthens. In Geometry V, the recirculation is nearly round, whereas, it is more elongated for the other geometries. The other interesting point to note in Geometry V is related to the position of the recirculation relative to the bumps. Between $R_e = 0.5$ and $R_e = 1.2$, the recirculation strengthens, but is somewhat trapped between Bumps 2-3. However, at $R_e = 3.5$, it jumps to the next indentation (Bumps 1-2; see labeling in Figure 5.2). The general result is therefore that the presence of bumps along the coastline inhibits and retards the jump to the high energy branch for the Munk problem with free-slip boundary condition. However, the radius of curvature of the coastline has to be fairly small (i.e., smaller than the radius of deformation) in order to achieve reasonable circulations under high Reynolds numbers.

What is of interest is the vorticity structure for all these geometries. Figure 5.6 shows the relative vorticity field for Geometry IV and V and for different Reynolds numbers. One general characteristic is that these fields are less smooth than those for the stream function or the elevation field. This relates to the fact that the vorticity corresponds to the second order derivatives of the stream function. The vorticity field is therefore noisier and more difficult to resolve. Nonetheless, the results from the SE

model are very encouraging when compared to those obtained from finite element models for which the vorticity fields are generally much noisier. One basic feature is that the vorticity approximates the form of a positive Dirac delta function close to the tip of the bumps. Therefore, dynamical processes close to the tip are rather complex, irregular and difficult to resolve using a high order formulation. However, the use of a discontinuous SE formulation seems to be of some help in resolving these irregularities by not propagating them to neighboring elements. The largest peaks are observed where the velocity is the largest. The magnitude of these peaks ranges between 10^{-5} and 10^{-4}s^{-1} . Where the magnitude of these peaks goes beyond 10^{-5} , a tail of positive vorticity forms downstream of the peaks. Hence, the excess of positive vorticity is advectively transported downstream. Of course, these peaks increase the local gradient of vorticity pointing outward. They are therefore directly related to the mechanism which balances the vorticity budget and limits the size of the recirculation. Furthermore, we note that a positive vorticity wall surrounds the recirculation zone. This wall is consistent with the presence of a region of low velocity outside the recirculation zone (i.e., a region of strong shear). We note also that, for Geometry V and $R_e = 3.5$, a thin filament of large negative vorticity is located near the western boundary. An important remark concerns the Rossby number, R_o in the presence of bumps. By measuring the ratio ζ/f_0 , we note that R_o is above 0.1 for Geometry III and reaches about unity for Geometry V. As predicted, R_o can be fairly large in the presence of bumps which invalidates the QG approximation.

We also show the power input (the rate of energy put in by the wind), \bar{P} , in Figure 5.7. \bar{P} describes how the circulation adjusts to the wind pattern in order to minimize its energy. In general, it shows that the increase in \bar{P} is much less than that in R_e . This means that the circulation adjusts in such a way that reducing ν by a factor of two does not lead to a doubling of \bar{P} . It would be interesting to verify if some simple scaling arguments reproduce this result. However, it is difficult to derive a scaling for \bar{P} since it cannot be estimated on boundary layer considerations alone but requires also the knowledge of the interior circulation. The figure shows that

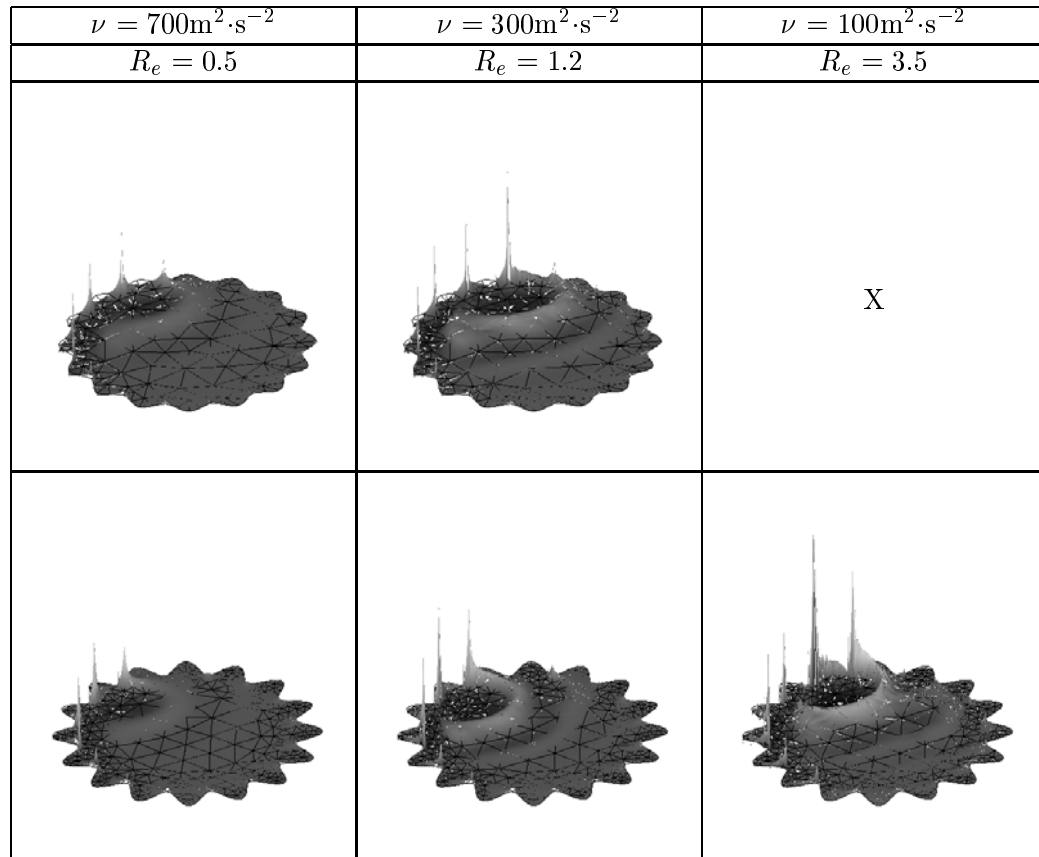


Figure 5.6: Mean vorticity field for the Geometries IV and V using the SE model. When no steady state could be reached because the solution jumps to the high energetic branch, an 'X' is drawn instead. The influence of the bumps is clearly seen by the abrupt jump in the vorticity field.

the rate of increase is larger for the regular geometry than for the irregular geometries. In fact, the rate of increase is rather similar for the two irregular geometries, although there is a general shift toward lower values of P as the bumps grow in size. In contrast with results in double gyre experiments (Scott and Straub, 1998) where P tends to decrease with increasing R_e , the single gyre circulations tend to have difficulties in minimizing P . This stems from the single-gyre circulation being too stable. Under the double-gyre wind forcing, the recirculation is usually highly unstable and counter-gyres develop above a certain R_e (the four gyres structure observed by Greatbatch and Nadiga, 2000; also visible in Scott and Straub, 1998).

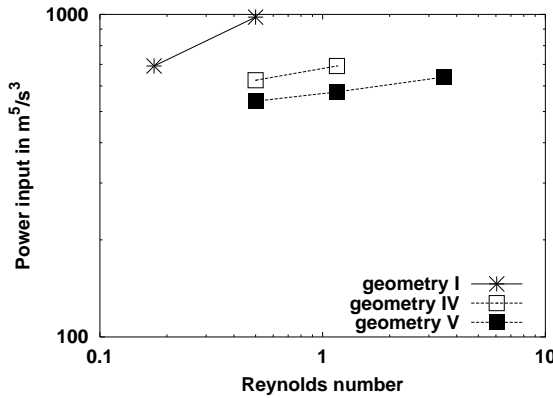


Figure 5.7: Power input by the wind using the mean fields with respect to the boundary Reynolds number.

5.3.2 Role of the Transients for Geometry V at High Reynolds Number

We now focus on the results of the high Reynolds number, $R_e = 3.5$, and Geometry V. In particular, we are interested in the role of the transients in achieving a steady state. One way to investigate the role of the transients is to plot maps of the standard deviation for the elevation. Figure 5.8 reveals that a belt of strong anomalies exists south of the recirculation. This belt extends northward to Bump 16 and 15, and westward close to Bump 5 where it reaches a maximum. The

western part of the recirculation is also a local maximum of the deviation. It is along this belt that we observe strong eddies going around the recirculation and moving westward. We can further refine this kind of analysis by generating the same kind of maps but for selected frequencies.

Figure 5.9 reveals the activity of the eddies of period over 200 days. This figure is very similar to Figure 5.8. It reveals that the main contribution to the standard deviation comes from the slow modes. The maximum is located in the eddy-belt as previously introduced, south-east of the recirculation with another but slightly weaker maximum close to the western boundaries. That the eddies tend to intensify in proximity of the recirculation and not at the boundary probably means that they strongly interact with the recirculation.

Figure 5.10 shows standard deviations for periods between 17 days and 200 days. By isolating these periods, we hope to emphasize the influence of small eddies. A strong signal is visible south-west of the recirculation near Bump 5. It may be due to larger eddies and Rossby waves interacting with the western boundary and bouncing back at shorter wavelengths. The other noticeable point is that the western part of the recirculation is mainly active in this band of frequencies. Consistent with these findings, we noted that weak eddies of scale above the radius of deformation are produced on the southern flank of eastern bumps. The trajectory of these eddies instead of being simply westward is actually more to the south-west in the absence of strong currents. The eddies seem to originate from large shifts of the elevation in interaction with the bumps. The strongest eddies originate from this mechanism but at higher latitudes. There, they interact with the recirculation and intensify.

Finally, Figure 5.11 shows the standard deviation for periods between 0.6 and 17 days. This figure mainly shows the inertial gravity and Kelvin waves. The maximum standard deviation for this figure is ten times smaller than the mean standard deviation of Fig. 5.8. Of interest is to note the spatial patterns of the Kelvin waves along the boundaries. The across-stream length scale tends to decrease near the bump tips, and

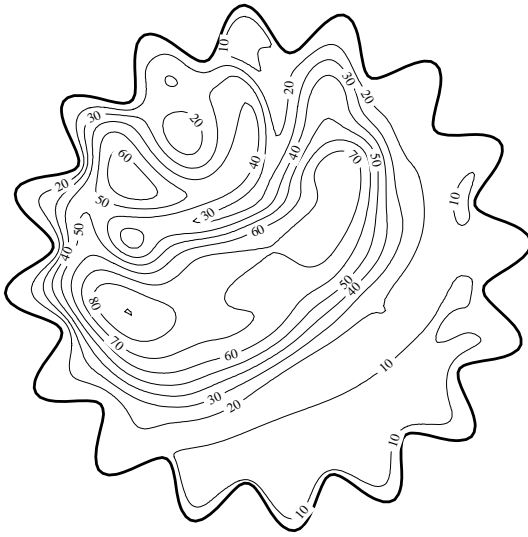


Figure 5.8: Mean standard deviation of the elevation.

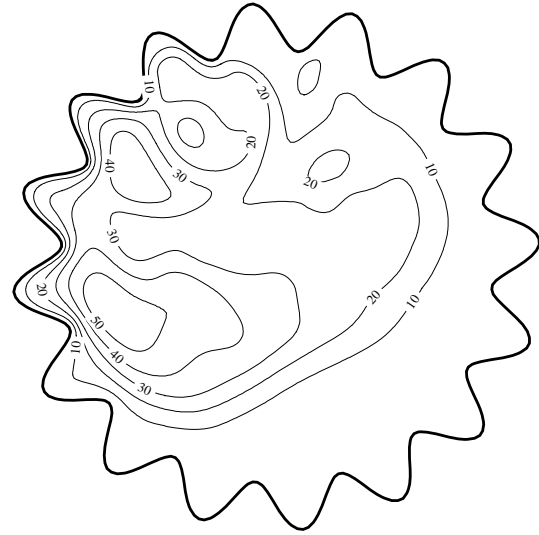


Figure 5.10: Mean standard deviation of the elevation for frequencies with period between 17 and 200 days.

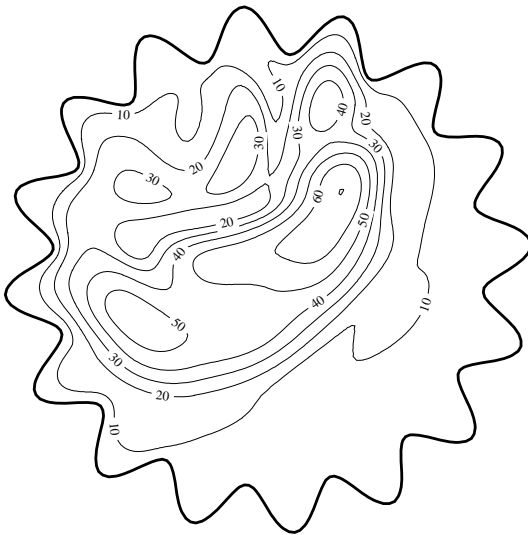


Figure 5.9: Mean standard deviation of the elevation for frequencies with period above 200 days.

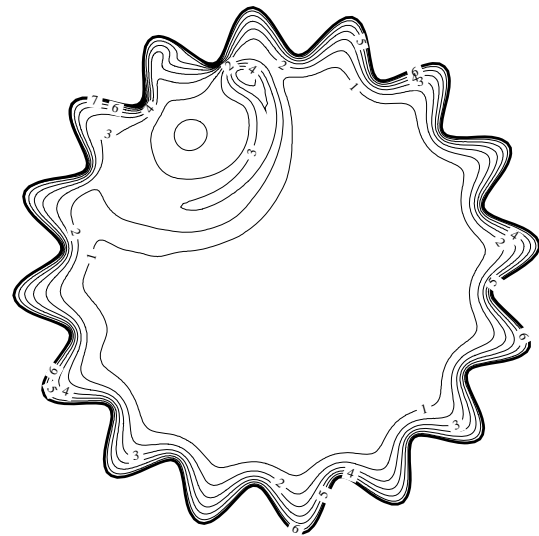


Figure 5.11: Mean standard deviation of the elevation for frequencies with period between .6 and 17 days.

decrease between bumps. This is evidence that the Kelvin waves are distorted by the presence of the bumps. The “packing” itself varies along the boundaries of the basin. The packing is loose in the eastern part of the basin and very severe in the western part, especially at Bump 1 and 2. The packing is then less and less severe as the Kelvin waves move anti-clockwise away from the recirculation. These variations in the packing of the Kelvin waves is related to the strength of the boundary currents. These currents are very strong near the recirculation, weaker away and absent in the eastern part of the basin. Figure 5.11 shows also two other interesting regions. One is the edge of the recirculation in the interior of the basin, where the inertial currents separate from the boundaries. There, the standard deviation peaks close to Bump 1 and sheds a tail along the edge of the recirculation. Presumably, because of the strong inertial currents, the Rossby number is large in this region and the inertial currents are slightly geostrophically unbalanced and produce inertial-gravity waves. A second region of interest is between Bump 1 and 2. There, the pattern due to the Kelvin waves is distorted because of the separation from the west flank of Bump 1. A reasonable explanation is that the Kelvin waves are disrupted by the encounter with the strong inertial currents of the recirculation and generate other gravity waves at Bump 1.

Transients may be essential in assuring lower energy levels by transferring the energy down-scale. This down-scale transfer can happen in two ways: either the eddies transfer the energy to inertial-gravity waves by interactions along the western walls, or in the recirculation zone through geostrophic imbalances. These small-scale inertial-gravity waves then dissipate the energy if their scale is close to the dissipative range. The recirculation location appears to be the most important from a plot of the divergence field (not shown). An intense dipole is present right at Bump 2, in front of the recirculation zone. The divergence may be related to a strong forcing of the Kelvin waves observed in Figure 5.11. The Kelvin waves are characterized by a mode two wave (two crests, two troughs around the basin) with period 8.3 days (Fig 5.12). The fact that these Kelvin waves correspond to a free mode of oscillation and are very regular both spatially and temporally suggests a resonant interac-

tion². Some irregularities are visible, though. These arise from interactions with the tip of the bumps along the western boundary. In order to emphasize the nonlinear energetic transfer to the Kelvin waves and possible viscous dissipative effects, we analyze the amplitude of the Kelvin waves as they propagate along the boundaries.

Since the amplitude of the Kelvin waves is dependent on the Coriolis parameter, f , we need to first separate the Coriolis effect from production or dissipative effects in order to make a clear diagnostic on these waves. To this aim, we can use the following rule (see also Gill, 1982, p. 379-380): For a Kelvin wave propagating along a southern boundary, we have

$$\begin{cases} \eta = h_0 e^{-y/L_{Ro}} F(x - ct) \\ u = \frac{gh_0}{c} e^{-y/L_{Ro}} F(x - ct) \\ v = 0, \end{cases} \quad (5.11)$$

where the southern boundary is located at $y = 0$ km, $c = \sqrt{gh}$ and L_{Ro} is the radius of deformation given by $L_{Ro} = c/f$. The linearized total energy of this Kelvin wave is, after simplification:

$$te(x, y, t) = gh^2/2 + Hu^2/2 = gh_0^2 F^2(x - ct) e^{-2y/L_{Ro}} \quad (5.12)$$

After integration over space, the energy becomes

$$TE = \int \int te(x, y, t) dx dy = gh_0^2 \frac{L_{Ro}}{2} \int F^2(x - ct) dx \quad (5.13)$$

Now, we assume that the same Kelvin wave moves along a meridional wall conserving TE , with no change in structure ($\int F^2 dx$ is now a constant independent of the orientation of the wall) but a change in amplitude and in the radius of deformation, L_{Ro} . As

²The regular temporal and spatial structure of the Kelvin waves still eludes us. It is possible that nonlinear interactions occur in a band of frequencies that covers the frequency of these free-mode Kelvin waves. At this frequency, the waves may be so resonant that they can pick up a very faint signal.

L_{Ro} changes with latitude, h_0 changes inversely as the square root of L_{Ro} for the total energy to be conserved. And as L_{Ro} is inversely proportional to f , h_0 is therefore proportional to the square root of f . Thus, we can correct the amplitude of the Kelvin waves for the beta effect by using the relation:

$$h'_0 = \frac{h_0}{\sqrt{f_0 + \beta y}}. \quad (5.14)$$

The elevations along the boundaries were first corrected with respect to change in the envelope (passage of an eddy or global shift of the circulation strength) using a 17 day smoother. From this time series, h_0 was computed using the difference of maximum and the minimum elevation observed at one location during a 17 day time window.

Figure 5.13 shows both h_0 and h'_0 along the boundaries as the averaged value over the last 6 years of simulation. Along the western boundary, as the Kelvin waves pass the tip of the bumps, they encounter counter currents. The strength of these currents is not strong enough to stop the Kelvin waves, but does slow them and induces the peaks of Figure 5.13 and the packing in Figure 5.11. It is also apparent that there is a continuous decline in the amplitude of the Kelvin waves as they leave the western region of production and move anti-clockwise. This decline is probably due to viscous effects which are large for the scale of the width of the Kelvin wave. There is apparent but weak modification of the waves as they passed the tip of the eastern bumps where we measured radius of curvature of 18 km which are consistent with Figure 5.11. Therefore, the Kelvin waves tend to follow the coastline even when the radius of curvature is below the radius of deformation. The Kelvin waves cannot reflect on the eastern wall as Rossby waves because their frequency is too high for Rossby waves to exist. There is, however, the possibility that Kelvin waves generate inertial-gravity waves along the eastern boundary, as they go around the bumps and diffract some energy. For the eddy viscosity used and taking a velocity of 3 cm/s along the eastern boundaries, features below 3 km lie in the dissipative range. Therefore, these Kelvin waves must be largely dissipative themselves, directly or by further cascade to inertial gravity waves. Thus, the Kelvin waves provide one mechanism for the dissipation of the energy at this

particular Reynolds number (not necessarily true at higher R_e).

Of interest is to note that the amplitude of the Kelvin waves is not constant during the simulation (Fig. 5.14). In fact, we note that the amplitude is anti-correlated to the total energy (Fig. 5.15), the amplitude being highest when the total energy is the lowest. One explanation may be that, as the amplitude of the Kelvin modes grows, more energy can be dissipated via these waves. If the amplitude of the Kelvin waves grows, the reason lies in stronger interactions with the recirculation. These interactions may be related to the strong instabilities of the recirculation. It is difficult to explain why there should be a 180° phase lag between the energy in the Kelvin waves and the total energy, which represents mostly the geostrophic modes. A 180° phase lag would appear if all the energy lost in the geostrophic modes went into the Kelvin waves with very weak dissipation. However, Figure 5.13 implies nearly a 70% drop in amplitude for a Kelvin wave going along the perimeter of the basin (in 20 days). This suggests a very strong dissipation, inconsistent with the long period variations of Figures 5.14 and 5.15 (about 500 to 1000 days).

The maps of the standard deviation of the elevation field reveals that the recirculation zone is very active. Transient geostrophic eddies tend to amplify in the proximity of the recirculation. Energy leaks from the recirculation to these eddies and to the Kelvin waves. In order to emphasize the instabilities in the circulation zone, Figure 5.16 shows a sequence of snapshots taken of the relative vorticity every 20 days between day 5705 and day 5985. This particular sequence was chosen because it shows rapid change of the recirculation zone itself. For instance, on days 5705, 5785 and 5885, the recirculation minimum has shifted to the west and is weaker, whereas the recirculation is the strongest for days 5745, 5825 and 5925 after the minimum has shifted back to the east, close to the position of the edge of strong positive vorticity. Consistent with the eastward shift and the intensification of the recirculation, a tail of positive vorticity is shed along its edge. Rapid changes in the recirculation patterns mean that particles are not trapped indefinitely inside but escape regularly. This mechanism may prevent the formation of a

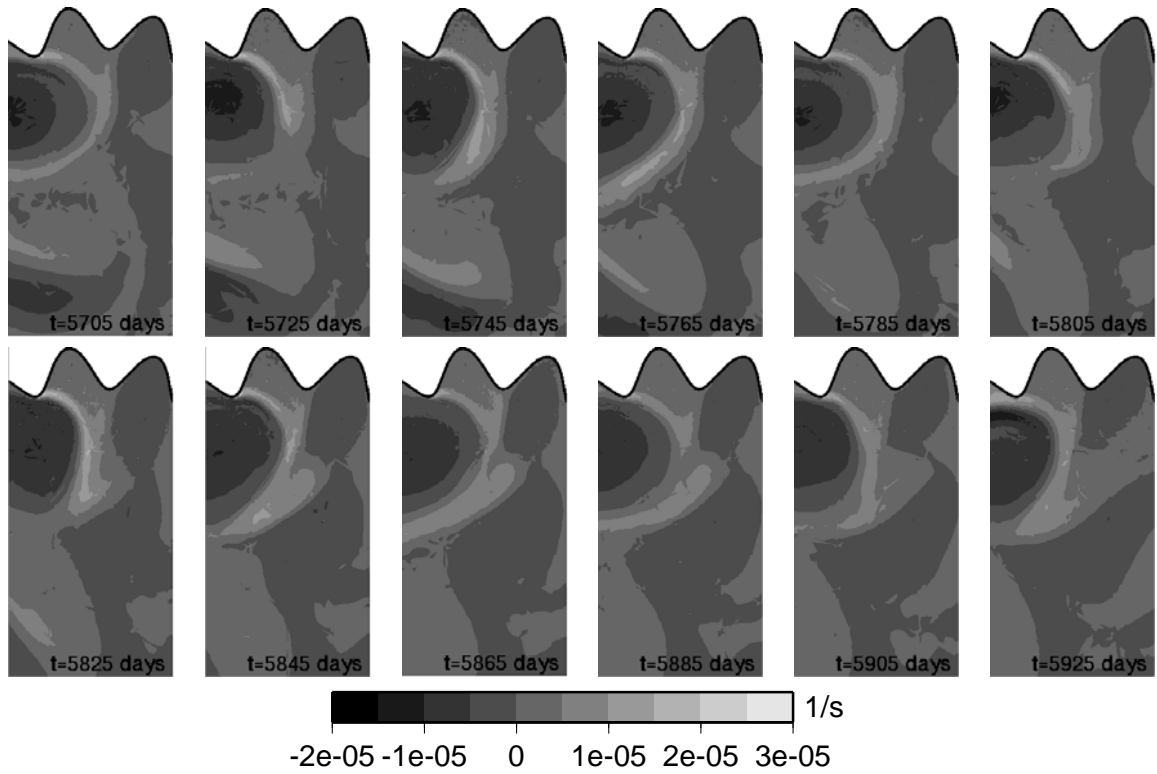


Figure 5.16: Instantaneous vorticity field in the vicinity of the recirculation. We focus of the period between 5705 and and 5925 days in a region limited in the south by $y = -250$ km, in the west by $x = -200$ km and in the east by $x = 200$ km. Bumps 1 and 16 are visible along the northern boundary.

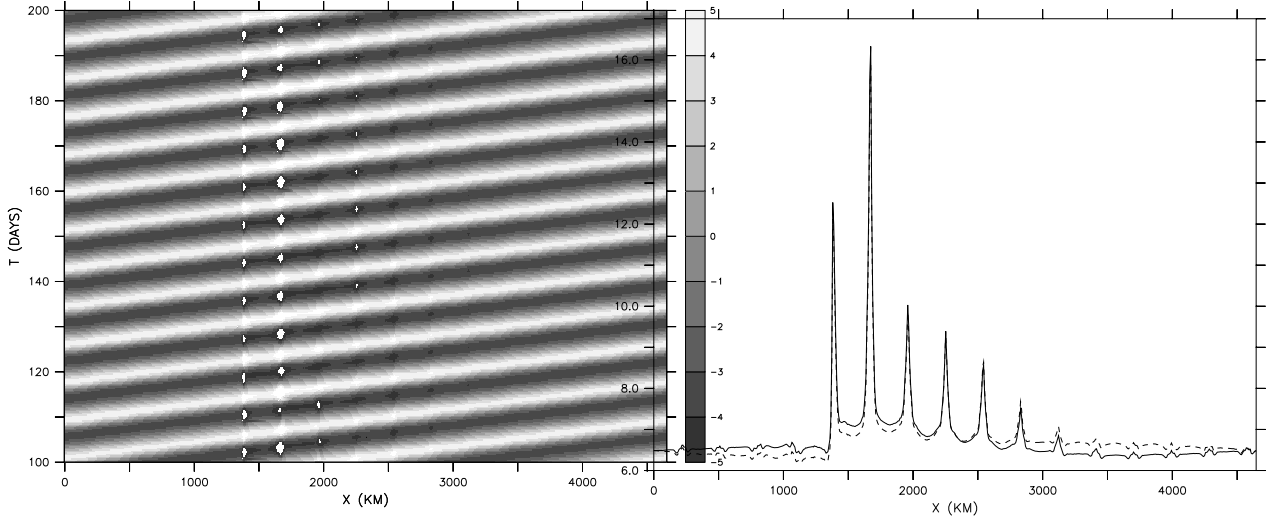


Figure 5.12: Hovmöller diagram of the filtered elevation with respect to time and location along the boundary. The elevation is given in meters. Note the strong regularity of the Kelvin waves. They are characterized by a mode 2 wave with period 8.3 days.

Figure 5.13: Amplitude of the Kelvin wave in meters along the boundary averaged over 6 years. The solid line represents the original amplitude, h_0 , and the dashed line represents the corrected amplitude, h'_0 , with respect to the Coriolis parameter.

Fofonoff gyre.

From a vorticity balance point of view, the transients transport the excess of vorticity produced in the interior to the walls. However, to be effective, such a transport needs to act across the streamlines. In a steady state, the vorticity balance across a streamline is

$$\oint \frac{\bar{\tau}}{h} \cdot d\mathbf{l} + \nu \oint \frac{\partial \bar{\zeta}}{\partial n} dl = \oint (\bar{\zeta} + f) \bar{\mathbf{u}} \cdot \mathbf{n} dl + \oint \bar{\zeta}' \bar{\mathbf{u}}' \cdot \mathbf{n} dl \quad (5.15)$$

The transport of the mean vorticity by the mean currents does not contribute to this balance ($\bar{\mathbf{u}} \cdot \mathbf{n} = 0$), therefore (5.15) simplifies to

$$\oint \frac{\bar{\tau}}{h} \cdot d\mathbf{l} + \nu \oint \frac{\partial \bar{\zeta}}{\partial n} dl = + \oint \bar{\zeta}' \bar{\mathbf{u}}' \cdot \mathbf{n} dl, \quad (5.16)$$

where vorticity transport by eddies and viscous flux balance the wind input.

In order to illustrate the eddy transport, Figure 5.17 shows three sub-figures. The

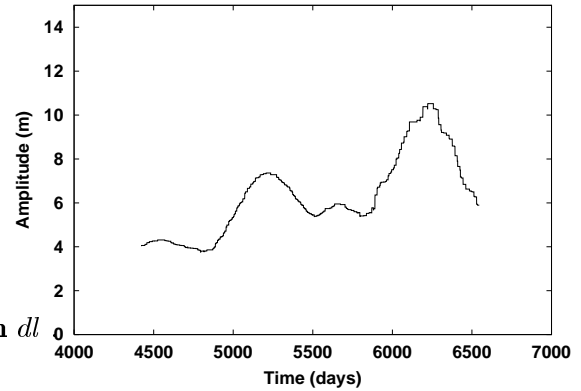


Figure 5.14: Time series of the amplitude of the oscillations at $(x=500 \text{ km}, y=0 \text{ km})$. The time series is for instance plotted in Figure 5.12 all along the boundary. From this series at the specified location, the maximum and minimum were taken in a 52-point running window (approximated 17 days). The difference of these two quantities divided by two yields the amplitude at a particular time.

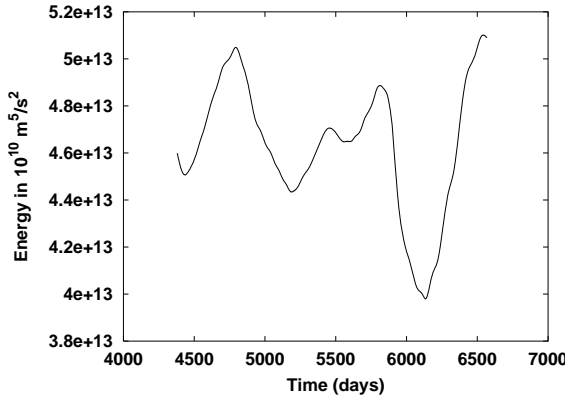


Figure 5.15: Total energy for the last 6 years of simulation. Note that the amplitude of the Kelvin wave of Figure 5.14 tend to be anti-correlated with the total energy.

first is the curl of the wind input over the domain ($\mathbf{k} \cdot \nabla \times \frac{\tau}{h}$), the second is the divergence of the eddy transport of vorticity ($\nabla \cdot \overline{\zeta' \mathbf{u}'}$) and the third is a vector-plot of the eddy transport normal to the mean streamlines as to emphasize the across-streamline component. The first two figures emphasize the local sources and sinks to the vorticity budget. The darker regions in the first sub-figure are stronger sinks of vorticity and the dark (light) regions in the second sub-figures are sources (sinks) of vorticity. In the first sub-figure, it is apparent that most of the domain is a sink of vorticity, consistent with the idea of a single-gyre forcing. However, due to the strong gradient present in the elevation field, the southern part of the recirculation is a very weak source of vorticity whereas the northern part and more specifically the regions surrounding Bump 1 and 2 are strong sinks of vorticity. The divergence of the eddy transport of vorticity (the second sub-figure) shows much finer scales and more noise. The basic features of this sub-figure are the presence of two arcs along the eastern and southern edges of the recirculations of opposite signs. The interior arc is a region of convergence of the eddy transport (source of vorticity) whereas the exterior arc is a region of divergence (sink). Regions close to Bump 3, 4 and 5 are mostly sources of vorticity whereas the regions between bumps tend to be weak sinks.

The maximum magnitude of the eddy transport is comparable to the value of the wind input. Three active regions are evident on the third sub-figure. The first is the recirculation zone, the second is directly southwest of this and the last region is southeast of the recirculation. The transport in the recirculation zone is outward-oriented along the western edge and inward along the southern and parts of the eastern edges. On this sub-figure, the two arcs of convergence (source of vorticity) and divergence (sink) are recognizable. The net forcing over the recirculation region appears to be weakly positive. This strong activity along the edge of the recirculation is another evidence that the transients are important in preventing the recirculation from growing and filling the entire domain, as it does when the solution jumps to the high energetic branch.

Southwest of the recirculation (the second region), the transport is mainly westward and southward oriented. Southeast of the recirculation (the third region), it is mainly eastward and southward oriented with an additional northward component closer to the eastern wall. The two other regions emphasize the eddy activity in the eddy belt, as defined above. Since westward propagating eddies with negative (positive) relative vorticity tend to migrate north (south), it follows that the eddy vorticity transport should be southward. This is consistent with the sub-figure which shows a main southward orientation. As the belt tends to surround the recirculation, the eddies propagate first to the southwest and then to the west. The eddy vorticity transport seems to adjust to this and tend to be oriented first to the southeast and then to the south, following a main leftward orientation with respect to the eddies.

From this analysis, it appears that the role of the mean vorticity transport (not shown) is not to be underestimated since the eddy transport seems to mainly remove the excess of vorticity from inner streamlines to outer streamlines. Close to the western boundary, the eddy transport shows no particular eastward orientation (which would be the signature of transport into the interior of positive vorticity produced at the wall). The mean vorticity transport is therefore still necessary to bring the excess of vorticity to the walls. This is done through several stream-

lines lying in the viscous sublayer, in particular around Bump-2, where the relative vorticity is at its maximum.

5.4 Scale Analysis and Discussion

In order to interpret the large scale and steady characteristics of the Munk circulation of the previous sections, we propose to develop some scaling arguments and compare these with the numerical results. One approach is to derive a criterion based on vorticity budgets (following Pedlosky) under the free-slip boundary condition for steady solutions which allows for curved boundaries. For straight walls, the relative vorticity is zero along the boundary. For a strong inertial layer in which we neglect viscous effects, we know that the absolute vorticity is conserved along a parcel trajectory (see Figure 5.18). Let us consider the conservation of absolute vorticity for simplicity. This one is $\zeta + f = f_0 - \beta L_y/2$ in the southern part of the domain (upstream of the inertial layer) where the relative vorticity is zero. Since absolute vorticity is conserved in the inertial layer, it is reasonable to imagine that the minimum absolute vorticity is such that $\zeta + f_0 + \beta L_y/2 = f_0 - \beta L_y/2$ in the northern part of the domain (downstream of the inertial layer). Therefore, the minimum relative vorticity is $\zeta = -\beta L_y$. Hence, in order to have an idea of the magnitude of the viscous flux of vorticity out of the domain, we only need to estimate the width of the viscous sublayer in the presence of the recirculation. One limitation, though, of this approximation is that the recirculation is formed of closed contours of both potential vorticity and the streamfunction. Hence, to the extent that particles remain trapped in the recirculation for long periods, wind forcing can lead to even lower values of ζ here. However, from experience, the minimum in the recirculation zone is usually superior to (less negative) or about the number we gave ($-\beta L_y$), as long as the recirculation zone is confined to the northwestern part of the gyre. As soon as this zone reaches the eastern walls (i.e., with increased Re), it forms a Fofonoff-type gyre that fills the whole basin, and for which the vorticity is much lower. Using the vorticity

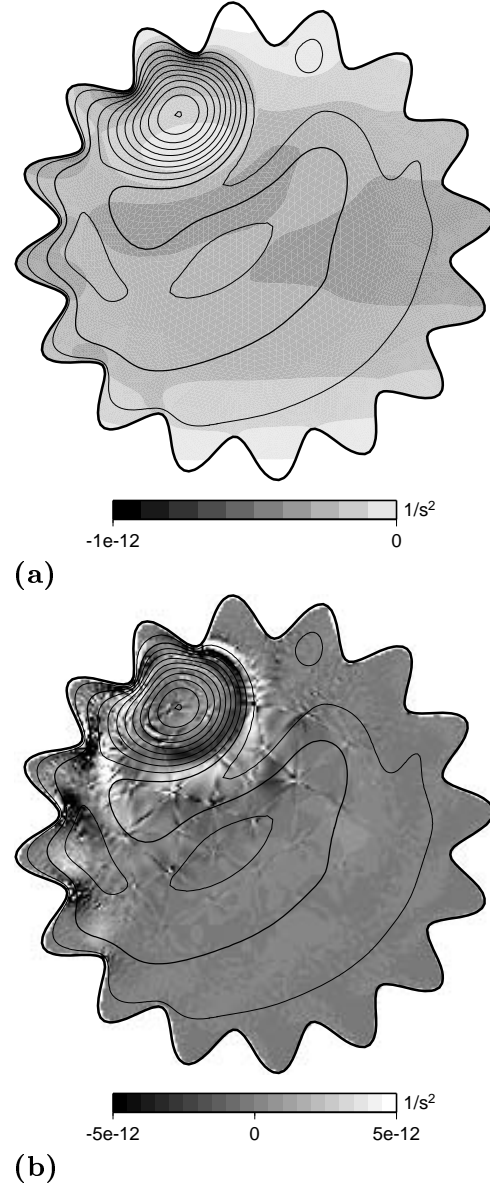
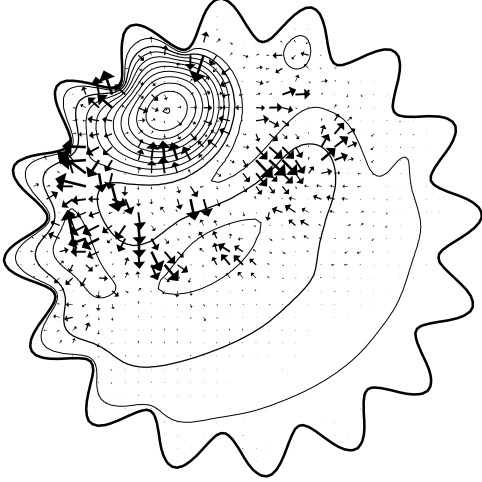


Figure 5.17: (a) Local wind input to the vorticity in Geometry V. (b) Local divergence of the eddy transport of vorticity in Geometry V computed using the last 6 years of simulation. (c) Vector plot of the eddy transport of vorticity normal to the streamlines in Geometry V computed using the last 6 years of simulation. The elevation field is plotted as an analog of the streamlines on each sub-figures.



(c)

Figure 5.17 continued

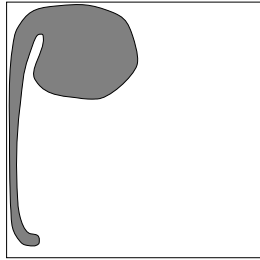


Figure 5.18: The region in grey represents where the absolute vorticity is approximately conserved. It encloses the inertial layer along the western boundary and the recirculation in the north-western corner.

budget given in (5.1) and the viscous sublayer thickness, $L\delta'_M$, as the scale at which the vorticity varies in the boundary layer, we derive the simple criterion for a circulation in straight walls in the presence of a strong recirculation ($R_e \sim 1$):

$$l_e \nu \frac{\beta L}{L\delta'_M} + \oint \frac{\tau}{h} \cdot d\mathbf{l} \sim 0 \quad (5.17)$$

where l_e is the length of the recirculation. The second term, the wind input, in the vorticity balance is easy to determine. It varies with h ; however, from experience, we can consider $h \sim H$. A first scaling for l_e can be obtained from (5.17) after substituting (5.5):

$$l_e \sim \sqrt{R_e} L. \quad (5.18)$$

For $R_e = 0.5$, we obtain $l_e = 710$ km, which is reasonably close to what is observed in Figure 5.5.

This scaling can be compared to Pedlosky's (1996, pages 85-86). Pedlosky evaluates the recirculation length scale using three equalities. The first one comes from the equality in the momentum equations between the advection terms and the diffusion terms in the viscous sublayer in the presence of the recirculation:

$$l_* = \sqrt{\frac{\nu}{\psi_e}} l_e \quad (5.19)$$

where l_* is the thickness of the sublayer and ψ_e is the transport in the recirculation. The second equality comes from the transport in the sublayer being equal to the Sverdrup transport and from the velocity in the sublayer being equivalent to the velocity at the edge of the recirculation:

$$\frac{V_{Sv} L}{l_*} = \frac{\psi_e}{l_e}. \quad (5.20)$$

The third equality comes from the vorticity input by the wind in the interior of the ocean being equal to the viscous flux of vorticity across the recirculation edge

$$\frac{\nu \psi_e}{l_*^2 l_e^2} = \beta V_{Sv} L^2. \quad (5.21)$$

These three combined equations allow one to derive one equation for l_e :

$$l_e^2 = \frac{V_{Sv}^3 L^2}{\beta^2 \nu^2} \quad (5.22)$$

which can be simplified using (5.2-5.5) to

$$l_e = \frac{\delta_I^3}{\delta_M^3} L = R_e L. \quad (5.23)$$

Pedlosky's scaling of l_e however implies an inconsistent definition of the viscous boundary layer thickness along the recirculation. The thickness for the viscous sublayer can be obtained from (5.19-5.23):

$$\delta'_M L = l_* = \frac{\nu l_e}{V_{Sv} L} = R_e L \frac{\nu}{V_{Sv} L} \quad (5.24)$$

Using again (5.2-5.5), this equation becomes

$$\delta'_M = R_e \frac{\delta_M^3}{\delta_I^2} = \delta_I. \quad (5.25)$$

Hence, the viscous sublayer thickness is no longer dependent on ν . This seems counter-intuitive: for high R_e , one expects $\delta'_M \ll \delta_I$. Therefore, we will continue to use our own estimate of δ'_M as given in (5.5) and we will give the equivalent result using δ'_M in the presence of a recirculation as given by Pedlosky. The true scaling might be in between these two values. Nonetheless, in both cases, the behavior of l_e with increasing Reynolds number is roughly the same. The recirculation length quickly increases with increasing Reynolds number and the Sverdrup interior can no longer be sustained for $R_e > 1$.

Now, in the presence of a curved coastline, (5.17) is modified to account for the positive vorticity produced at the wall. Since the recirculation has closed contours of streamlines, all the Sverdrup transport goes between the recirculation and the wall. We assume this region to be the viscous sublayer. Therefore, the volume transport through the sublayer is:

$$L \delta'_M v^* \sim L V_{Sv} \quad (5.26)$$

where v^* is the velocity in the viscous sublayer (this is actually identical to Eq. 5.20)). This yields

$$v^* \sim \delta_I \sqrt{R_e} \beta L^2 \quad (5.27)$$

for the scaling of v^* . Using (5.26), we estimated v^* to be of the order of 0.84 m/s for $R_e = 3.5$. We now need to estimate the vorticity produced at the wall. This is of the

order of v^*/R_s as given by (5.7). Let us assume that the production of positive vorticity is valid within half a wavelength of the curvy coastline and that no vorticity is produced in the other half. The second term in (5.1) becomes

$$\oint \frac{\partial \zeta}{\partial n} dl \sim \frac{l_e}{2} \frac{\beta L}{L \delta'_M} + \frac{l_e v^*/R_s + \beta L}{2} \frac{1}{L \delta'_M} \sim \frac{l_e}{\delta'_M} \left(\beta + \frac{1}{2} \frac{v^*}{L R_s} \right). \quad (5.28)$$

Therefore, in the presence of curved coastlines, the relation (5.17) becomes:

$$l_e \sim \frac{\beta V_{Sv} L^2}{\frac{\nu}{\delta'_M} \left(\beta + \frac{1}{2} \frac{v^*}{L R_s} \right)} \quad (5.29)$$

Using the same values as above, $\delta'_M = 0.040$ at $R_e = 0.5$ and $R_s = 10$ km, this relation yields a length of $l_e = 340$ km.

There are two regimes, depending on the magnitude of R_s , the radius of curvature of the coastline; one at low curvature corresponding to (5.18) and the second at high curvature that we want to investigate. Let us consider now the condition under which the recirculation is controlled by the curvature of the coastline. This condition corresponds to the second term being larger than the first term in the denominator of (5.29):

$$R_s L < \frac{1}{2} \frac{v^*}{\beta} \quad (5.30)$$

and after substituting (5.5,5.26), we obtain

$$\frac{R_s}{L} < \frac{1}{2} \sqrt{R_e} \delta_I. \quad (5.31)$$

Hence, the transition depends on the Reynolds number. As R_e increases, the radius of curvature can increase for the second regime to persist, implying less curvy coastlines. For the second regime, the length of the recirculation is governed by the vorticity produced at the wall and, substituting (5.5,5.26), is scaled as

$$l_e \sim \frac{R_s}{\delta_I} \quad (5.32)$$

Hence, the length of the recirculation in curved geometries is no longer dependent on the eddy-viscosity, ν . In other words, the Reynolds number dependence in l_e disappears. This result is valid as long as the curvature satisfies (5.31).

The weakest point in this argument is probably the estimate of the thickness of the viscous sublayer (δ'_M) and the velocity in the sublayer (v^*) in the presence of the recirculation. Using the estimation of Pedlosky, $\delta'_M = \delta_I$, we would have found

$$l_e \sim \frac{R_s}{\delta_I} \sqrt{R_e} . \quad (5.33)$$

By this estimation, l_e is still dependent on the Reynolds number, but the dependence would be somewhat weaker when compared to regular domains (Eq 5.18 or 5.23). Moreover, in the presence of curved coastline, it is not clear what δ'_M becomes. The viscous sublayer might be squeezed between the recirculation and the bumps and therefore, the normal derivative of the vorticity might be increased, which favors smaller recirculations. It is also possible that the viscous sublayer is not squeezed but that some streamlines of the recirculation may lie within it. In such a case, a proper definition of the viscous sublayer becomes difficult. The second point relates to the form that the vorticity takes around the bumps, which we assume to be constant over a half wavelength of the curvy coastline. As we noted in the numerical results, the vorticity actually behaves quite singularly at the tip of bumps. An additional problem relates to the length of the perimeter which increases with increasing number of bumps and with increasing amplitude of these bumps. This would again favor lower values for l_e . Lastly, these scaling arguments were based on the assumption that the action of the transient eddies are negligible, which may not be the case for sufficiently high R_e .

We now compare the predictions from our scaling argument about the recirculation length scale to Figure 5.5. We note that, at $R_e = 0.5$, the recirculation changes in character between Geometry II and III. Between these two geometries, the strength of the recirculation weakens and its length decreases. Moreover, for Geometry V, the length of the recirculation does not increase significantly with increasing R_e (300 km to 350 km). The

latter observation is consistent with (5.32). Therefore, the circulation seems to be controlled by the curvature of the geometry between Geometry II and III. At $R_e = 0.5$, the inequality (5.31) is however only satisfied for Geometry V. Moreover, for a fixed radius of curvature, (5.31) should be satisfied at a specific R_e and the circulation in that particular geometry should be controlled by the radius of curvature beyond that specific R_e . However, we observe the opposite. For example, as R_e increases, the length of the recirculations for Geometry IV increases slowly but then jumps to the energetically high branch. The criterion (5.31) may not be very representative when the solution tends to jump to the energetically high branch with increasing R_e . Nonetheless, the formula derived for l_e seems to yield a relatively good prediction when the curvature is large enough (Geometry V).

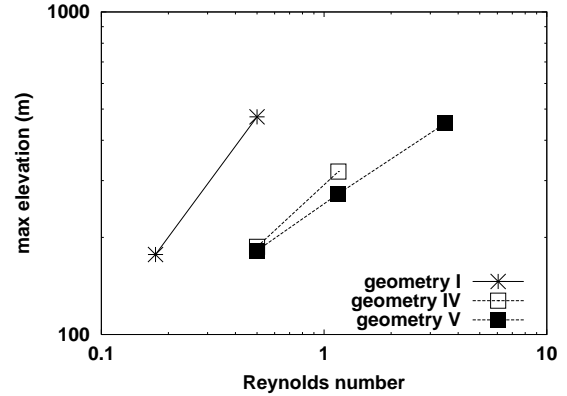


Figure 5.19: Maximum of the mean elevation for the three geometries. The maximum elevation is a good proxy for the strength of the recirculation.

Now focusing on results from Geometries I, IV and V, we derive a predictive law for the strength of the recirculation based on previous scalings. The Geometries IV and V are chosen because they show the most robust sign that their circulation is controlled by the curvature. The strength of the gyre is given by the maximum transport through the basin (dominated by the recirculation). Let us define the strength of the recirculation as the volume transport through it. The transport is defined as the mean velocity in the recirculation multiplied by its cross-section

length. Let us assume that the magnitudes of v^* and l_e are sufficient to characterize this transport. From (5.18) and (5.27), the maximum transport in regular basins is then given by

$$\psi_{max} \sim H v^* l_e \sim R_e \delta_I \beta L^3 H \quad (5.34)$$

and in irregular basins by, substituting (5.27) and (5.32)

$$\psi_{max} \sim \sqrt{R_e} \beta L^2 H R. \quad (5.35)$$

Therefore the strength should be sensitive to the presence of the bumps. A good proxy for the strength of the gyre is the maximum elevation observed in the basin (because of the geostrophic approximation prevailing in most of the domain). Figure 5.19 shows the maximum elevation with respect to R_e . It appears that the strength of the gyre is dependent on the form of the geometry. There is a clear shift in the strength of the gyre between Geometries I and IV. Moreover, the slope (the power relation between h_m and R_e or the slope coefficient in a log-log plot) is close to unity for the regular geometry (1.06), whereas it is about 0.5 for Geometry IV. At $R_e = 0.5$, the strength is identical for Geometry IV and V, but the slope is somewhat less for Geometry V. These results seem to follow (5.34) and (5.35), and the scaling for the sublayer thickness in the presence of the recirculation seems therefore to be closer to (5.5) than to that of Pedlosky.

Another important quantity related to the strength of the gyre is the kinetic energy (KE). We plot KE with respect to R_e . Since the strength of the recirculation is dependent on the Reynolds number via v^* , the kinetic energy must depend on the Reynolds number despite the presence of the indentations, but at much lower rate compared to the kinetic energy in regular geometries. By assuming that, at first order, KE is governed by the energy in the recirculation, we estimate that in the regular geometry the energy grows with both the length and the strength of the recirculation by using (5.18) and (5.27)

$$KE \sim H v^{*2} l_e^2 \sim R_e^2 \delta_I^2 \beta^2 L^6 H \quad (5.36)$$

whereas it grows only with the strength of the recirculation in the presence of indentations, substituting (5.27) and (5.32)

$$KE \sim H v^{*2} l_e^2 \sim R_e \beta^2 L^4 H R^2. \quad (5.37)$$

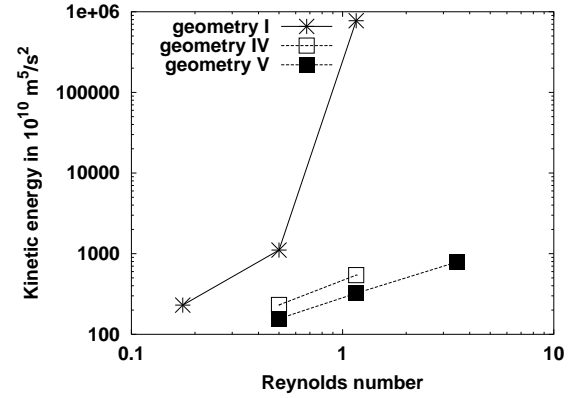


Figure 5.20: Kinetic energy of the mean fields with respect to the boundary Reynolds number. One point has been plotted on the high energy branch for the first geometry. This one was evaluated using a FD-QG model in a rectangular domain and is plotted only for giving the order of the jump.

Figure 5.20 shows the increase in the energy of the mean fields for Geometries I, IV and V. The presence of a wavy perturbation of the circular geometry retards the jump of the solution to the high energy branch and the increase with the Reynolds number is much slower in the presence of indentations along the coastline. Before the solution in the intermediate geometry jumps to the high branch, it is noteworthy that the slope for $\log KE$ with respect to $\log R_e$, for the two irregular geometries, is rather similar. The slope is 1.7 for Geometry I, and 0.85 for Geometry IV and 1.0 for V. All actual values for the slopes are rather close to their expected values, even though this might be coincidental.

5.5 Adaptivity

We use the adaptive refinement in order to check the levels of errors in our previous simulations. The fact is that large discontinuities develop in the vorticity field between elements close to Bump 1 and 2. These discontinuities are located close to the tip of the bumps and at the edge of the recircu-

lation. We also noted that some discontinuities are associated with the piecewise boundary parabolas near inflection points along the coastline where third degree polynomials would be more adequate. We therefore redesign a mesh with more points along the western bumps and slightly more in the interior. On the new mesh, the vorticity field is indeed improved but further refinement would be needed to obtain a reasonable vorticity field, especially in proximity of Bump 2 where a strong velocity shear exists. Moreover, strong negative vorticity seems to originate from Bump 3 and is shed in front of Bump 2 with dramatic consequences to the resolution of the vorticity field. This is possibly connected to two anticyclonic eddies trapped between Bump 3-4 and 2-3. Starting from this mesh, we use the adaptive strategy developed in Section 2.4.3. We have a certain level of liberty in the choice of the fields and the parameters controlling the selection of the elements to be refined. In Section 3.4, we used the primitive variables for controlling the level errors. From a geophysical fluid perspective, it would be interesting to control the errors using the vorticity, which is a one order higher field relative to the velocity. If the latter is correctly resolved, it should follow that the other fields are also well resolved. We found that this approach was reliable by testing the adaptive strategy in a simpler experiment. From this experiment, we noted that the velocity, elevation and vorticity fields are indeed well resolved, and that, for the same parameters λ_i , the vorticity controlling adaptivity induces one additional level of refinement. Unfortunately for Geometry V, we could not afford in terms of computational cost more than one adaptive cycle. Therefore any claim of convergence has to be discarded. After one cycle (Fig. 5.21), the refined elements are concentrated along the tip of Bump 2 and less near Bump 1. Of course, the refinement has a cost. The simulation on the refined mesh is about four times more expensive than that on the original mesh, due to time-step limitations.

We now compare the two experiments for the Geometry V and $\nu = 100 \text{ m}^2/\text{s}$. Figure 5.22 shows the total (kinetic + potential) energy for the two experiments. The refined and original results are rather similar for the first year, but they depart afterwards. However, we see the same approxi-

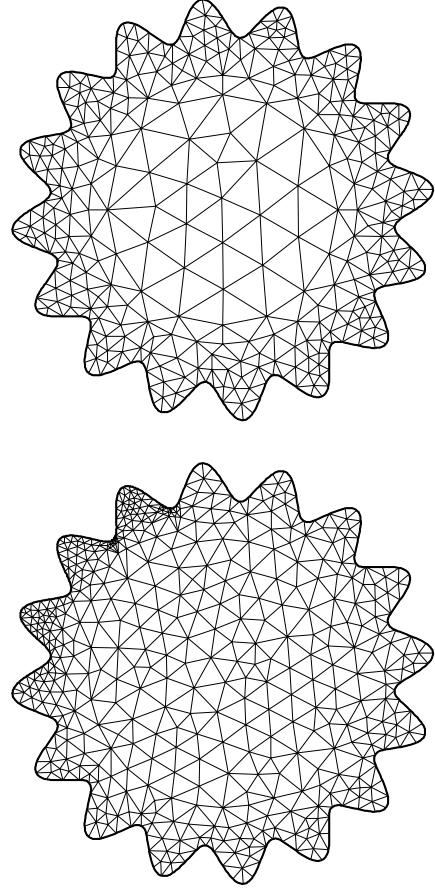


Figure 5.21: Mesh for the original and the refined runs.

mate low frequency (about 1000 day period) behavior, which is the signature of a Rossby basin mode. The higher frequencies (small eddies) may be responsible for the most of the discrepancy. What is more intriguing is that the Kelvin wave activity increases significantly for the refined experiment. Between day 4400 and 4800, the amplitude of the Kelvin wave on both meshes at the same location is rather similar, with the amplitude on the refined mesh being slightly larger. Then, after day 5000, the amplitude on the refined mesh quickly doubles relative to the amplitude on the original mesh and this factor then remains more or less constant. Presumably, the production of Kelvin waves is enhanced by the increased resolution in the region of Bump 2 where Kelvin waves are generated. As with the original mesh, the amplitude of the Kelvin waves on the refined mesh are anti-correlated with the total energy. However, the increased amplitude of Kelvin waves on the refined mesh did not lead to a decrease of the total energy between the original and refined meshes. This raises two possibilities. Either the Kelvin waves are only marginal in the dissipation of the energy or, more probably, this could be an artifact of the resolution. On the original mesh, it is possible that processes located near Bump 2 were too dissipative because of the too coarse resolution.

The overall structure of the mean elevation field is rather similar for the original and refined meshes (Fig. 5.24). Although not noticeable in Fig. 5.24, an important improvement lies in the structure of the elevation field close to the tip of Bump 1, 2 and 3, where the elevation shows a rather singular behavior on the original mesh. By contrast, the elevation field at the same locations is much smoother and the amplitude of the peaks in elevation much less on the refined mesh. The mean total energy for the refined mesh tends to be slightly larger than that on the original mesh, although, due to the relative short period of observation (6 years), this may not be significant. Much improvement can be noticed in the mean vorticity field. The strong peak at Bump 2 is better resolved (although the amplitude is not severely modified), as well as the zone of negative vorticity near the same bump. This undershoot seems to be real and not an artifact of the lack of resolution on the original mesh. Some improvement is also noticeable in the

interior of the basin, likely due to a slightly improved resolution on the new mesh in the interior. The edge of the recirculation would stand some refinement. However, since the largest discontinuities in the vorticity field are close to the tip of the bumps, the mesh is first refined there. To conclude, we gain, using the adaptive strategy, improvements over the complex processes happening close to the bumps and consequently some improvement of the nonlinear interactions and related energetics (the increased amplitude of the Kelvin modes). However, there are no significant changes in the overall mean circulation.

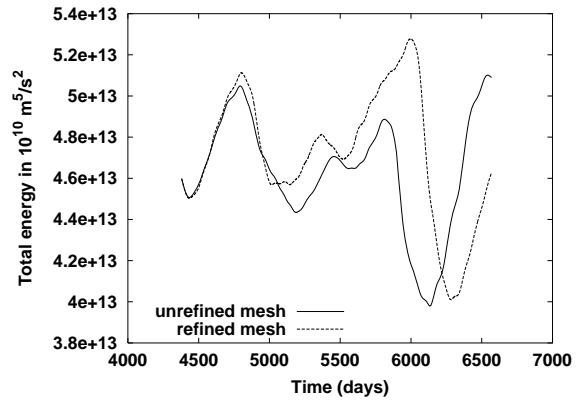


Figure 5.22: Total energy for the last 6 years of simulation for the original and refined meshes. The two curves are very similar for the first year and then depart slowly from each other.

5.6 Conclusions

We show applications of a discontinuous spectral element model to the problem of the inertial runaway under the free-slip condition in irregular geometries. We first show that more traditional numerical methods, such as the finite difference methods, fail to converge in irregular domains for the boundary condition under interest. Second, the main results of this application of a spectral element model show that, in the presence of irregular boundaries, the jump to the high energetic branch is considerably retarded, occurring at a higher boundary layer Reynolds

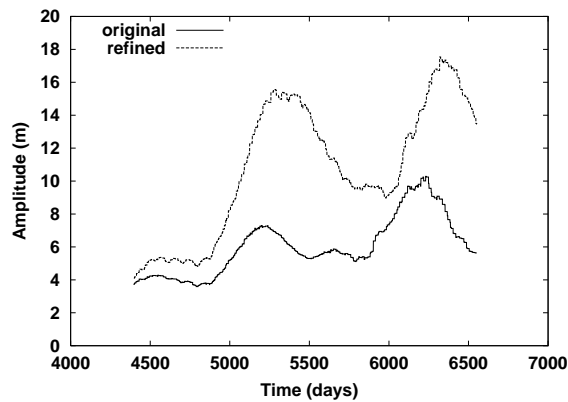


Figure 5.23: Amplitude of the fast oscillations at $(x=500 \text{ km}, y=0 \text{ km})$ along the boundary for the original and refined meshes.

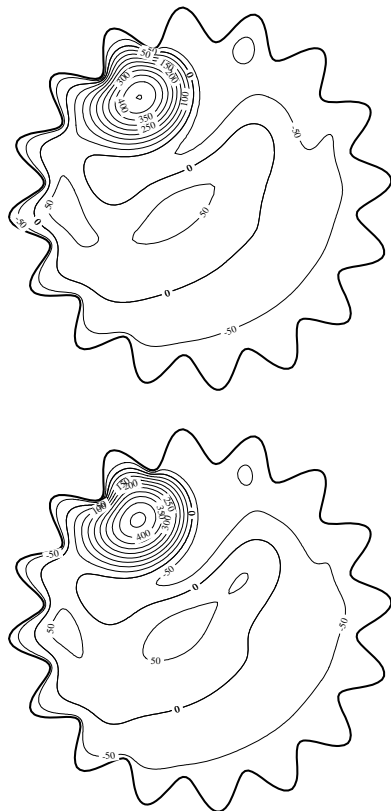


Figure 5.24: Mean elevation fields for the original mesh and the refined mesh.

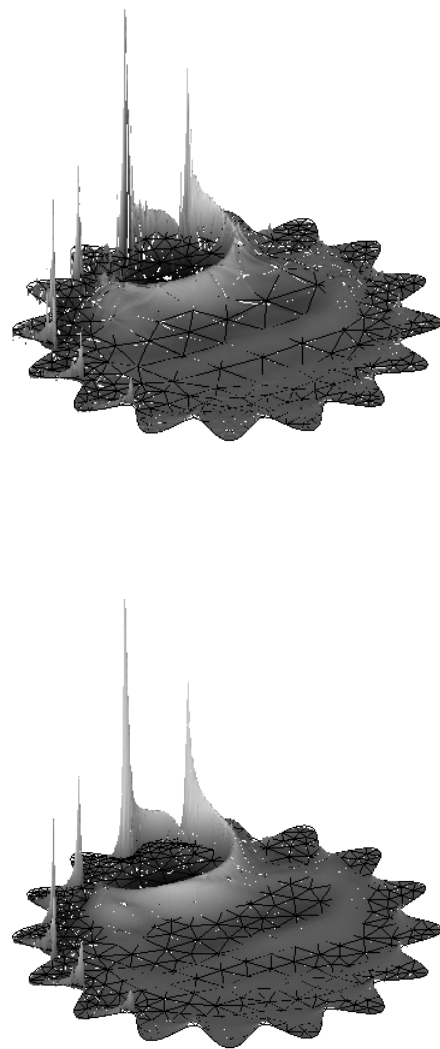


Figure 5.25: Mean vorticity fields for the original mesh and the refined mesh.

number. The presence of smooth bumps along the coastline introduces a source of positive vorticity and thus a source of production of eddies through barotropic instabilities. From the point of view of the vorticity budget, positive vorticities along the walls ease the process of balancing the wind input with stronger viscous fluxes of vorticity at the walls. Eddies are also important to the vorticity budget because they transport the vorticity through the inertial layer to the viscous sublayer where it can be dissipated. However, we noted that the eddies do not play a large role in the vorticity budget. We also noted the presence of strong Kelvin waves that may provide a mechanism for transferring energy to smaller scales and dissipate it. Of course, as the Reynolds number is increased (and ν decreased), these Kelvin waves are no more sufficient to dissipate the energy. Then, other nonlinear processes must come into place, such as triad interactions developed by Bartello (1995) between low and fast modes. Of interest is to note that the main Rossby mode of oscillation of the basin contrasts with that in rectangular geometries where it is usually observed that the main mode of oscillation is a basin scale Rossby wave of large amplitude (observable in both QG and SW models). The weak presence of such a mode in our simulation may mean that this mode is damped by the complex geometry of the basin.

The assessment of our scaling arguments brings up some interesting issues. First, our scaling arguments are surprisingly close to the numerical results despite obvious theoretical weaknesses. Because those arguments assumed laminar boundary layers, this implies that production of eddies was insufficient, not only to invalidate our scaling, but also to prevent inertial runaway. It is worth commenting that the double gyre circulation usually induces many more eddies. In order to get more eddies, the single gyre circulation would require more curved boundaries. For instance, it would be interesting to investigate what sort of equilibrium can be reached in basins where the boundaries are so irregular that free-slip flows have no choice but to separate from the boundaries at each bump. In such a case, it is however likely that the assumptions on which the SW equations are based would be no longer valid. For instance, the fact that the region around Bump 2 requires a resolution below 1 km

implies that the SW assumption is breaking down. Moreover, the small eddy production points out to lack of physical processes represented by the SW models. Baroclinic instability, for instance, which is a main contributor to turbulence in both the atmosphere and the ocean seems to be needed in order to definitively close the inertial runaway issue in single gyre experiment. In such a case, we would need to run expensive three-dimensional baroclinic models. Finally we demonstrate the use of an adaptive strategy in ocean modelling. We note however that the cost of such a method is higher than using fixed meshes in time (see Section 3.4). Nonetheless, it provides an automated procedure for resolving and localizing fronts and strong nonlinear currents which would otherwise require tedious manual remeshing. For instance, we noted that the results from the adapted mesh yield stronger Kelvin waves, apparently related to the increased resolution in the regions of Kelvin wave production.

Chapter 6

Conclusions

In this thesis, we were interested in assessing the performance of different numerical methods for modelling the ocean in complex geometries. Complex geometries are represented by step-like walls in the most conventional numerical method used in oceanography, namely the finite difference (FD) method. The presence of these steps may be detrimental to the representation of currents located along the boundaries, especially the western return currents if we consider the simple Munk gyre problem. From this perspective, finite element (FE) methods and spectral element (SE) methods with their accurate representation of the coastlines may provide more accurate solutions of the ocean circulation.

In Chapter 3, we compare these different numerical methods for a few test problems. In a rectangular geometry, the FD method is always more accurate at a given cost than FE methods using linear basis functions. However, for a simple analytical linear solution in a circular domain, we showed that conventional FD methods tend to have truncation orders between unity and two, instead of two. In that case FE methods provide more accurate solutions at the same cost than do FD methods. For nonlinear solutions and in a rectangular domain, all tested FE models showed a bias which tends to be robust with increasing resolution. In most finite element models, the problem is linked to numerical dissipative effects that were too small to be detected in the linear test-cases but that were large in the nonlinear test-case. These dissipative effects are related to the stability properties of each of the schemes and how each of them finds its way around the stability condition. Only one tested FE model satisfies to the so-called Ladyzhenskaya-Babuska-Brezzi

(LBB) condition for FE models. This model showed also some signs of over-dissipation but in that case, the problem was more related to the use of a semi-Lagrangian treatment of the time discretization of the equations. Unfortunately, we have not made use of a FE model satisfying to the LBB condition with an Eulerian treatment of the equations. However, we can speculate based on the results of Chapter 3 that such a model would not be as cost-effective as the tested SE model. Nonetheless, the use of a LBB-complying FE model may prove to be more appropriate than FD models when spatially variable mesh capabilities are required, such as for resolving straits and inlets.

The tested element model shows high order truncation errors for linear and nonlinear test-cases in rectangular and circular domains. In the latter case, we reached a limitation due to our use of piecewise parabolas for the description of curved geometries. To test cost-effectiveness, we compared the SE and FD models for the nonlinear Munk problem in a rectangular domain. This test reveals that the accuracy of the SE method has to be about 1% of the true solution to be more effective than the second order C-grid FD model. However, for nonlinear problems the SE method presents a decisive advantage that its accuracy remains more or less identical in rectangular and generally curved domains whereas that of the finite difference methods degrades.

Finally, we tested with success an adaptive mesh strategy in a time-stepping mode. We designed an automated procedure that estimates the local error and refines the mesh accordingly in regions of largest errors as the simulation runs. This was tested for the Munk gyre problem. We noted that, when

the required accuracy was high enough, most of the refinement goes into resolving the initial Kelvin waves which is excited by the onset of the wind and propagate along the boundary. After this initial transient process comes to rest, the mesh is automatically derefined along the boundary. In terms of cost, the adaptive procedure proves to be slightly less efficient than to run the model on a fixed mesh in time. However, this procedure might be useful in contexts for which the solution is not known a priori. In such cases, the location of sharp fronts is not known and may require a tedious manual remeshing in order to resolve these features. Sometimes, this process has to be done iteratively a large number of times and, in such a case, an adaptive strategy will prove far superior.

In Chapter 4, we focused on the influence of step-like walls in the finite difference methods, extending the study of Adcroft and Marshall. We used vorticity budgets as a diagnostic tool in order to assess the accuracy of the numerical solutions. We showed that the accuracy of FD methods degrades in presence of steps along the boundaries and that the truncation order is lowered. Depending on the specific numerics, we estimated that the truncation error varies between the zeroth and second order. In general, we found that vorticity budgets are not very accurate due to the presence of extra terms, such as the advection of vorticity, which do not appear in the analytical budget. Surprisingly, we noted that a quasi-geostrophic model does not lead to significantly more accurate vorticity budgets than those given by shallow water models, even though the former type of models explicitly solves for the vorticity equation. We also used a vorticity budget analysis on a shallow water B-grid model with free-slip boundary conditions which proved not to converge to a steady state with time, whereas the equivalent C-grid model does. In fact, this particular B-grid implementation proved to be inadequate.

In Chapter 5, we explored the theoretical possibility that free-slip circulations can develop their own eddies if the coastline is curved enough. This chapter can be considered as an application of the spectral element method and a contribution to the understanding of the ocean circulation from a

theoretical point of view. Since it is not clear what type of boundary conditions is the most realistic to use at typical or even high resolution in ocean modelling, there is no obvious reason to discard the free-slip boundary condition¹. So far, time dependent simulations of the nonlinear Munk problem in rectangular domains under free-slip boundary conditions show that the solution is very steady once it reaches its equilibrium. That is, no eddies develop. Moreover, under the same boundary condition, the solution becomes completely unrealistic passed a certain Reynolds number and still remains steady. Hence, the necessary eddies that transport the excess of vorticity to the walls are absent in these simulations. Therefore, these simulations in rectangular domains make a good case against the use of the free-slip boundary condition. This was certainly a strong incentive to use instead the no-slip boundary condition. However, the real oceans present irregular coastlines which may be the key-factor absent from these earlier experiments. We therefore investigated the influence of having curvy coastlines in the otherwise usual Munk problem for varying Reynolds number. The only model available to us that could perform such a task with a high degree of accuracy was the SE model. The finite difference models are too sensitive to the presence of steps along the coastline and the tested FE models are too dissipative for the Reynolds numbers we are interested in.

From scaling arguments and assuming a steady state with no transient eddies, we were able to derive that the bumps along the coastline cause the circulation to slow down compared to the no-bump case. This was due to the production of positive relative vorticity at the walls close to the tip of the bumps for a mid-latitude gyre in the northern hemisphere². Furthermore, as the Reynolds number increases, we predicted that the total kinetic energy should increase at much slower rate than that of the no-bump case. If

¹The no-slip and free-slip boundary conditions are the traditional boundary conditions used in ocean modelling but they are not the only ones possible. In fact, some other parametrizations have been proposed. See for instance Straub (1999).

²the sign of the relative vorticity produced at the wall would be negative in the southern hemisphere for a cyclonic gyre but our results would still apply.

these free-slip circulations were able to produce their own eddies, it would be possible that even lower total kinetic energy values could be reached. Therefore, the presence of bumps along the coastline might be sufficient so that the main circulation escapes the anti-intuitive fate of not converging to some statistical steady state as the eddy viscosity is decreased. This fate is known as the inertial runaway and represents our inability to explain how the nonlinear processes of simple flows are sufficient to balance a decrease of poorly known diffusive parameters, such as the eddy viscosity.

Unfortunately, only the first prediction was verified; that the rate of increase of the total kinetic energy with increasing Reynolds number was decreased, but not reversed, contrary to our second hypothesis. We also noted a dependence on the local curvature of the coastline. The higher the curvature, the lower the total kinetic energy. Except for the largest curvature, the solutions jump to an unrealistic state passed a critical Reynolds number. For the largest curvature and the largest Reynolds number, we observe some eddy activity but not enough to slow down the total kinetic energy increase compared to our scaling arguments. In fact, most of the vorticity balance seems to be achieved by the main circulation. Indeed, the vorticity is large and positive along a significant portion of the bumps which leads to a large flux of vorticity at the walls. Moreover, we observed that the vorticity tends to follow a rather singular behavior along the bumps even though the bumps are smoothly curved. This was verified by using an adaptive mesh algorithm which increases the resolution of the model where the errors are the largest. More eddies could have been generated by larger curvature. However, we feared that we reached the validity limit, in terms of length scales of the observed processes, of the simple equations we were using, namely the shallow water equations. Baroclinic models may be required to represent the small scales features occurring along the western boundary.

One other important limitation of this study that we need to mention is related to the “fractal nature” of the coastline. From that perspective, it is quite unreasonable to define “one” curvature of the coastline, as this one is modified with increasing sampling of the coastline. Rather, we limit ourselves

to the study of the influence of curved coastlines whose radius of curvature falls in the range of scales of interest (from the radius of deformation and the boundary layer widths to the basin scale). A more realistic approach would be to use a spectrum of wavelengths and amplitudes consistent with realistic coastlines. The overall result might not be very different from those presented in this thesis, though.

The SE model showed great advantages as a tool in order to address theoretical issues such as the inertial runaway problem. As it captures some features of the coastline, such as the curvature, we could address the issue of free-slip flows in presence of curved coastlines. However, its general variable resolution coupled to an adaptive mesh refinement enables this model to address the runaway problem and other theoretical aspects linked to nonlinear flows in presence of irregular coastlines for any kind of boundary condition. Nonetheless, the model still has to prove its effectiveness in the more general baroclinic framework. The vertical representation is certainly a very complex issue, and different strategies are possible. Schematically, the vertical representation can be z - or σ - or isopycnal levelled. Of the three, the σ seems to be the most natural to the SE method because it allows for a polynomial description in the vertical as well. However, it does not offer a good control on the particular depth range to resolve. It therefore may have difficulties in resolving sharp temperature or salinity gradients and may lead to Gibbs oscillations. The same problem exists in low-order numerical methods, such as finite difference models. However, it simply leads to accuracy problems rather than stability problems.

This study was obviously biased in focusing on one particular boundary condition, the free-slip boundary condition. Under this boundary condition, it is known that the FD methods do poorly in presence of steps. It may therefore seem obvious that SE methods do better. One may ask about the other well known boundary condition, the no-slip condition. For the no-slip boundary condition, we may assume that the FD methods in irregular domains do as well as they do for the nonlinear Munk problem in a rectangular domain (Section 3.4). In the latter case, we showed that the SE model does better only

for high enough resolutions at which the error is below 1%. At this range of resolution, the error is low enough that FD methods are still competitive. Unless one is interested in representing accurately the fast transients of the ocean such as Kelvin waves, for which the FD methods do poorly independently of the boundary condition, the FD methods have still a long future in front of them. This last statement is also biased by the assumption governing the primitive equations. If, for instance, faster and bigger computers allow for very high resolution non-hydrostatic simulations (which require the inversion of a 3D matrix problem), then the FE methods might be attractive again, since their main overhead, consisting of the inversion of a matrix problem even when the equations are solved explicitly in time, is no more.

The last point we would like to mention is related to the effect of “real” steps present along the coastline as opposed to “fake steps” that FD discretization tend to generate. As they are singular features, no numerical method is able to model them, although some analytical approaches were proposed (Cherniawsky and Leblond, 1986). Nevertheless, real steps can be approached as the limit of increasing to infinity the curvature of the bumps. From that point of view, we can derive some qualitative conclusions based on the results obtained in Chapter 5 with the SE model. It seems that steps always have a dissipative effect and that all the fields will be singular close to the step. Therefore, the corrected version of Adcroft and Marshall (the B combination of Chapter 4) is biased because it under-represents the effect of steps by assuming that they are non-existent to the point that circulations in rotated basins look similar to circulation in non-rotated basins. Hence, their method is very successful in rotated rectangular domains but fails in more generally irregular domains. The correct solution in presence of irregular domains depends on the irregularity of the domain. It lies between the corrected version of Adcroft and Marshall and the traditional implementation of the C-grid model which is more dissipative. Ultimately, the true solution reflects the fractal nature of the coastline.

Appendix A

An A-grid Energy Conserving Formulation

i	cell index
Vol_i	cell Volume
\mathbf{F}_b	normal oriented face length
ϕ_b	any variable interpolated at the center of face
$neigh$	face index for the i -cell

Table A.1: Notations for the finite volume method

It is possible to formulate an energy conserving scheme on a A-grid and generalize it to a finite volume formulation (i.e., irregular domains). We will use the notations of the latter (Table A.1). The time integration has to be done through an iteration process since the formulation is semi-implicit in time, including the non-linear terms.

$$Vol_i \frac{\mathbf{u}_i^{n+1} - \mathbf{u}_i^n}{\Delta t} + (f_i + \zeta_i^*) \mathbf{k} \times \mathbf{u}_i^* + \sum_{neigh} \mathbf{F}_b B_b^* = 0$$

$$Vol_i \frac{\eta_i^{n+1} - \eta_i^n}{\Delta t} + \sum_{neigh} \mathbf{F}_b \cdot (\mathbf{u}_i h)_b^* = 0 \quad (\text{A.1})$$

where $\phi^* = (\phi^{n+1} + \phi^n)/2$ for any ϕ . By multiplying A.1 by $\mathbf{u}_i^* h_i^*$, we get

$$Vol_i h_i^* \frac{\mathbf{u}_i^{n+1} - \mathbf{u}_i^n}{\Delta t} + \sum_{neigh} \mathbf{F}_b \cdot \mathbf{u}_i^* h_i^* B_b^* = 0 \quad (\text{A.2})$$

Let us define $K = \mathbf{u}^2$ and use $\mathbf{U} = h\mathbf{u}$, then A.2 reads

$$Vol_i h_i^* \frac{K_i^{n+1} - K_i^n}{\Delta t} + \sum_{neigh} \mathbf{F}_b \cdot \mathbf{U}_i^* B_b^* = 0 \quad (\text{A.3})$$

and let us multiply A.1 by K_i^* and use the equivalence $\partial h / \partial t = \partial \eta / \partial t$

$$Vol_i K_i^* \frac{h_i^{n+1} - h_i^n}{\Delta t} + \sum_{neigh} K_i^* \mathbf{F}_b \cdot \mathbf{U}_b^* = 0 \quad (\text{A.4})$$

We then sum together A.3 and A.4 in order to get an equation for the kinetic energy

$$Vol_i \frac{[h_i^{n+1} K_i^{n+1} - h_i^n K_i^n]}{\Delta t} + \sum_{neigh} \mathbf{F}_b \cdot (K_i^* \mathbf{U}_b^* + \mathbf{U}_i^* B_b^*) = 0 \quad (\text{A.5})$$

The equation for the potential energy is given by multiplying A.1 by $g\eta_i^*$

$$Vol_i \frac{g(\eta_i^{n+1})^2 - g(\eta_i^n)^2}{\Delta t} + \sum_{neigh} g\eta_i^* \mathbf{F}_b \cdot \mathbf{U}_b^* = 0 \quad (\text{A.6})$$

Let us define $e_k = g\eta^2 + hK$. We then get the total energy equation by summing A.5 and A.6

$$Vol_i \frac{(e_k)_i^{n+1} - (e_k)_i^n}{\Delta t} + \sum_{neigh} \mathbf{F}_b \cdot (B_i^* \mathbf{U}_b^* + \mathbf{U}_i^* B_b^*) = 0 \quad (\text{A.7})$$

Therefore, the total energy budget is

$$\begin{aligned}
& TKE^{n+1} - TKE^n \\
&= \sum_i Vol_i \left[(e_k)_i^{n+1} - (e_k)_i^n \right] \\
&= -\Delta t \sum_i \sum_{neigh} \mathbf{F}_b \cdot (B_i^* \mathbf{U}_b^* + \mathbf{U}_i^* B_b^*) .
\end{aligned} \tag{A.8}$$

Hence, the conservation properties of this scheme comes from the assumption about ϕ_b , the way we interpolate the data onto the faces of the cells. The usual assumption is to take for any ϕ , $\phi_b = 1/2(\phi_i + \phi_j)$ where j is the index of the neighboring cell. Because $\sum_{neigh} \mathbf{F}_b = 0$, the right hand side simplifies to

$$\begin{aligned}
& TKE^{n+1} - TKE^n \\
&= -\Delta t \sum_i \sum_{neigh} \mathbf{F}_b \cdot \frac{B_i^* \mathbf{U}_j^* + \mathbf{U}_i^* B_j^*}{2} .
\end{aligned} \tag{A.9}$$

The right hand side vanishes for open domains. For closed domains, some assumptions are required. If we imagine a fictitious cell on the other side of the wall, we must have

$$\mathbf{F}_b \cdot [B_i^* \mathbf{U}_j^* + \mathbf{U}_i^* B_j^*] = 0 . \tag{A.10}$$

This can be satisfied if $B_j^* = B_i^*$. We are then left with satisfying $\mathbf{F}_b \cdot (\mathbf{U}_i^* + \mathbf{U}_j^*) = 0$. This corresponds to enforcing that the velocity is tangential at the wall. This is a very reasonable assumption since it matches the inviscid boundary condition. Hence, the energy can be conserved for an A-grid scheme in absence of dissipation processes and forcing.

In practice, this scheme only retards the upcoming of spurious modes. In order to control the spurious modes, one idea would be to make the scheme also conserve the enstrophy. According to Abramopoulos (1988), this is achievable but a unreasonable price.

Appendix B

Model Vorticity Budget on a B-grid

Using Equations 2.21 and 2.22, the model vorticity equation is obtained at the center of the cell (also the η location):

$$\begin{aligned} \frac{\partial \zeta}{\partial t} + D_x^+ \overline{u \Delta_x v + v \Delta_y v}^y - D_y^+ \overline{u \Delta_x u + v \Delta_y u}^x \\ + D_x^+ g \overline{\partial_{y-} \eta}^{xy} - D_y^+ g \overline{\partial_{x-} \eta}^{yx} \\ + D_x^+ \overline{f u}^y + \partial_{y+} \overline{f v}^x \\ = D_x^+ g \overline{\frac{\tau_y}{h}}^y - D_y^+ g \overline{\frac{\tau_x}{h}}^x \\ + D_x^+ \overline{F_y}^y - D_y^+ \overline{F_x}^x . \end{aligned} \quad (\text{B.1})$$

Study of this equation shows that all terms cancel out in the interior. However, close to corners, they are not necessarily zero. The pressure term, hereafter I_P , for instance gives after summation over the domain and emphasizing the terms close to the northeast corner (assuming $\Delta x = \Delta y = \Delta$):

$$\begin{aligned} I_P &= \sum_i \sum_j \Delta x \Delta y \\ &\quad \left(D_x^+ g \overline{\partial_{y-} \eta}^{xy} - D_y^+ g \overline{\partial_{x-} \eta}^{yx} \right) \\ &= \frac{g}{2} (\eta_{i+1,j}^* - \eta_{i,j+1}^*) \\ &\quad + \dots + \text{other corner terms} \end{aligned} \quad (\text{B.2})$$

where η^* is the extrapolated value of the elevation along the wall and (i, j) are the indices taken at the velocity point directly southwest of the corner. When using a linear extrapolating law, $\eta_{i+1,j}^* = 3/2 \eta_{ij} - 1/2 \eta_{i-1,j}$, I_P

$$\begin{aligned} I_P &= \frac{g}{4} (\eta_{i,j-1} - \eta_{i-1,j}) \\ &\quad + \dots + \text{other corner terms} . \end{aligned} \quad (\text{B.3})$$

Hence, the pressure term in the vorticity equation does not cancel out. However, for the advective terms, hereafter I_{adv} , we have

$$\begin{aligned} I_{adv} &= \sum_i \sum_j \Delta x \Delta y \\ &\quad \left(D_x^+ \overline{u \Delta_x v + v \Delta_y v}^y \right. \\ &\quad \left. - D_y^+ \overline{u \Delta_x u + v \Delta_y u}^x \right) \end{aligned} \quad (\text{B.4})$$

which simplifies first to a circulation integral of the form

$$I_{adv} = \sum \mathbf{u} \nabla \mathbf{u} \cdot \Delta \mathbf{l} . \quad (\text{B.5})$$

One can prove that this summation cancels out. Hence, $I_{adv} = 0$. The same occurs for the Coriolis terms because the summation can be recast as a summation of flux normal to the wall at velocity points along the wall, which are zero due to the impermeability condition. Therefore, the model vorticity budget reduces in the case of the B-grid to

$$\sum_i \sum_j \frac{\partial \zeta}{\partial t} \Delta x \Delta y = \mathcal{F}_i + \mathcal{F}_{vis} - I_P . \quad (\text{B.6})$$

Hence I_P is present in the model budget whereas it should ideally be zero. Note that a zero order extrapolation ($\eta_{i+1,j}^* = \eta_{ij}$) results in the cancellation of I_P . However, this extrapolation leads to countercurrents along the boundaries for the Munk problem on a beta plane, as shown in Section 4.2.

Bibliography

- ABRAMOPOULOS, F., 1988:. Generalized energy and potential enstrophy conserving finite difference schemes for the shallow water equations. *Monthly Weather Review*, 116 :650–662.
- ADCROFT, A., HILL, C., AND MARSHALL, D., 1997:. Representation of topography by shaved cells in a height coordinate ocean model. *Monthly Weather Review*, 125 :2293–2315.
- ADCROFT, A. AND MARSHALL, D., 1998:. How slippery are piecewise constant coastlines in numerical ocean models. *Tellus*, 50 A :95–108.
- ADCROFT, A. J., HILL, C. N., AND MARSHALL, J. ., 1998:. A new treatment of the Coriolis terms in C-grid models at both high and low resolutions. *Monthly Weather Review*, 127 :1928–1936.
- ARAKAWA, A., 1966:. Computational design for long-term numerical integration of the equations of fluid motion: Two-dimensional incompressible flow. part 1. *J. Comput. Physics*, 1 :119–143.
- ARAKAWA, A. AND HSU, Y.-J. G., 1990:. Energy conserving and potential dissipating schemes for the shallow water equations. *Monthly Weather Review*, 118 :1960–1969.
- ARAKAWA, A. AND LAMB, V. R., 1977:. Computational design of the basic dynamical processes of the UCLA general circulation model. *Methods in Computational Physics*, 17 :174–267.
- ARNOLD, D., BREZZI, F., AND FORTIN, M., 1984:. A stable finite element for the stokes equation. *Calcolo*, 23 :337–344.
- BABUSKA, I., 1971:. Error bounds for finite elements methods. *Numer. Math.*, 16 :322–333.
- BARTELLO, P., 1995:. Geostrophic adjustment and inverse cascades in rotating stratified turbulence. *J. Atmos. Sci.*, 52 :4410–4428.
- BARTELLO, P. AND THOMAS, S. J., 1996:. The cost-effectiveness of semi-Lagrangian advection. *Monthly Weather Review*, 124 :2883–2897.
- BATTEEN, M. L. AND HAN, Y.-J., 1981:. On the computational noise of finite-difference schemes used in ocean models. *Tellus*, 33 :387–396.
- BECKERS, J.-M., 1999:. On some stability properties of the discretization of damped propagation of shallow water inertia-gravity waves on the Arakawa B-grid. *Ocean Modelling*, 1 :53–69.
- BELETSKY, D., O’CONNOR, W. P., DAVID J. SCHWAB, AND DIETRICH, D. E., 1997:. Numerical simulation of internal Kelvin waves and coastal upwelling fronts. *J. Phys. Oceanogr.*, 27 :1197–1215.
- BLAYO, E. AND DEBREU, L., 1999:. Adaptive mesh refinement for finite-difference ocean models: First experiments. *J. Phys. Oceanogr.*, 29 :1239–1250.
- BLECK, R., 1978:. Simulation of coastal upwelling frontogenesis with an isopycnal coordinate model. *J. Geophys. Res.*, 83 :6163–6172.
- BLECK, R. AND BOUDRA, D. B., 1981:. Initial testing of a numerical ocean circulation model using a hybrid quasi-isopycnal vertical coordinate. *J. Phys. Oceanogr.*, 11 :755–770.
- BLUMBERG, A. AND HERRING, H., 1987:. Circulation modelling using orthogonal curvilinear coordinates. In NIHOUL,

- J. AND JAMART, B., editors, *Three-Dimensional Models of Marine and Estuarine Dynamics*, volume 45, pages 55–88. Elsevier Oceanography Series.
- BLUMBERG, A. AND MELLOR, G., 1983:. Diagnostic and prognostic numerical circulation studies of the south atlantic bight. *J. Geophys. Res.*, 88 :4579–4592.
- BOULANGER, J.-P. AND FU, L.-L., 1996:. Evidence of boundary reflection of Kelvin and first-mode Rossby waves from the TOPEX/POSEIDON sea level data. *J. Geophys. Res.*, 101 :16361–16371.
- BREZZI, F., 1974:. On the existence, uniqueness and approximation of saddle point problems arising from Lagrangian multipliers. *RAIRO, Anal. Num.*, 8((R2)) :129–151.
- BRYAN, K., 1963:. A numerical investigation of a nonlinear model of a wind-driven ocean. *J. Atmos. Sci.*, 20 :594–606.
- BRYAN, K., 1969:. A numerical method for the study of the circulation of the world ocean. *J. Comput. Physics*, 4 :347–376.
- BRYAN, K. AND COX, M. D., 1967:. A numerical investigation of the oceanic general circulation. *Tellus*, 19 :54–80.
- CONNOR, J. AND WANG, J. D., 1974:. *Finite element modeling of hydrodynamic circulations*, pages 355–367. Numerical Methods Fluid Dynamics. Pentech Press.
- COX, M. D., 1979:. A numerical study of somali currents eddies. *J. Phys. Oceanogr.*, 29 :311–326.
- COX, M. D., 1984:. A primitive equation three-dimensional model of the ocean. Report, GFDL Ocean Group, NOAA, Princeton Univ., Princeton, NJ.
- DENG, J., 1992:. The problem of Gulf Stream separation: A barotropic approach. *J. Phys. Oceanogr.*, 22 :2182–2200.
- DIETRICH, D. E., KO, D.-S., AND YESKE, L., 1993:. On the application and evaluation of the relocatable DieCAST ocean circulation model in coastal and semi-enclosed seas. tech. report 93-1. Report, Center for Air Sea Technology, Mississippi State University, Building 1103, Stennis Space Center, MS 39529.
- DUMAS, E., PROVOST, C. L., AND PONCET, A., 1982:. Feasibility of finite element methods for oceanic general circulation modelling. In *Proc. 4th Int. Conf. on Finite Elements in Water Resources*. Hanover, Germany.
- DUNAVANT, D. A., 1985:. High degree efficient symmetrical Gaussian quadrature rules for the triangle. *Int. J. for Num. Methods in Eng.*, 21 :1129–1148.
- EKMAN, V. W., 1905:. *On the influence of the earth's rotation on ocean currents*, volume 11. Astr. o. Fysik (Stockholm). 53 pp.
- FIX, G. F., 1975:. Finite element models for ocean circulation models. *J. Appl. Math. Model.*, 29 :371–387.
- FOREMAN, M. G. G., THOMSON, R. E., AND SMITH, C. L., 2000:. Seasonal current simulations for the western continental margin of vancouver island. *J. Geophys. Res.*, 105 :19665–19698.
- FORRER, H. AND JELTSCH, R., 1998:. A higher-order boundary treatment for Cartesian-grid methods. *J. Comput. Physics*, 140 :259–277.
- FORTIN, M. AND FORTIN, A., 1985:. Newer and newer elements for incompressible flow. *Finite Elements in Fluids*, 6 :171–187.
- GENT, P. R., 1993:. The energetically consistent shallow water equations. *J. Atmos. Sci.*, 50 :1323–1325.
- GENT, P. R. AND MCWILLIAMS, J. C., 1990:. Isopycnal mixing in ocean circulation models. *J. Phys. Oceanogr.*, 20 :150–155.
- GERDES, R., 1993:. A primitive equation ocean general circulation model using a general vertical coordinate transformation. *J. Geophys. Res.*, 98 :14683–14701.
- GILL, A. E., 1982:. *Atmosphere-Ocean dynamics*, volume 30 of *International geophysics series*. Academic press.

- GREATBATCH, R. J. AND NADIGA, B., 2000:. Four-gyre circulation in a barotropic model with double-gyre wind forcing. *J. Phys. Oceanogr.*, 30 :1461–1471.
- GRESHO, P., LEE, R., AND SANI, R., 1978:. Advection-dominated flows with emphasis on the consequences of mass-lumping. *Finite Elements in Fluids*, 3 :335–350.
- HANNAH, C. G., SHORE, J., LODER, J. W., AND NAIMIE, C. E., 2000:. Seasonal circulation on the western and central scotian shelf. *J. Phys. Oceanogr.* In press.
- HIRST, A. AND MCDUGALL, T. J., 1996:. Deep-water properties and surface buoyancy flux as simulated by a z-coordinate model including eddy-induced advection. *J. Phys. Oceanogr.*, 26 :1320–1343.
- HOLLAND, W. R. AND LIN, L. B., 1975:. On the origin of mesoscale eddies and their contribution to the general circulation of the ocean. I. A preliminary numerical experiment. *J. Phys. Oceanogr.*, 5 :642–657.
- HÓLM, E. V., 1996:. Energy and enstrophy conservation properties of high-order non-oscillatory advection schemes. *Tellus*, 48A :122–137.
- HSIEH, W. W., DAVEY, M. K., AND WASJOWIZ, R. C., 1983:. The free Kelvin wave in finite-difference numerical models. *J. Phys. Oceanogr.*, 13 :1383–1397.
- HUA, B. AND THOMASSET, F., 1984:. A noise free finite element scheme for the two layer shallow equations. *Tellus*, 36A :157–165.
- HULBURT, H. E. AND HOGAN, P. J., 2000:. Impact of $1/8^\circ$ to $1/64^\circ$ resolution on Gulf Stream model-data comparisons in basin-scale subtropical atlantic ocean models. *Dynamics of atmospheres and oceans*, 32 :283–329.
- IDELSOHN, S., STORTI, M., AND NIGRO, N., 1995:. Stability analysis of mixed finite element formulations with special mention of equal-order interpolations. *Int. J. for Num. Methods in Fluids*, 20 :1003–1022.
- IERLEY, G. R. AND SHEREMET, V. A., 1995:. Multiple solutions and advection-dominated flows in the wind-driven circulation. Part I: Slip. *J. Mar. Res.*, 53 :703–738.
- ISKANDARANI, M. AND HAIDVOGEL, D. B., 1995:. A staggered spectral element model with application to the oceanic shallow water equations. *Int. J. for Num. Methods in Fluids*, 20 :393–414.
- LADYZHENSKAYA, O. A., 1969:. *The mathematical theory of viscous incompressible flow*. Gordon and Breach.
- LE PROVOST, C., GENCO, M. L., LYARD, F., VINCENT, P., AND CANCEIL, P., 1994:. Spectroscopy of the world ocean tides from a finite element hydrodynamic model. *J. Geophys. Res.*, 99 :24777–24798.
- LE PROVOST, C. AND VINCENT, P., 1986:. Some tests of precision for finite element model of ocean tides. *J. Comput. Physics*, 65 :273–291.
- LE ROUX, D. Y., LIN, C., AND STANFORTH, A., 1998:. Finite elements for shallow-water equation ocean models. *Monthly Weather Review*, 126 :1931–1951.
- LE ROUX, D. Y., LIN, C., AND STANFORTH, A., 2000:. A semi-implicit semi-Lagrangian finite elements shallow-water ocean model. *Monthly Weather Review*, 128 :1384–1401.
- LESIEUR, M., 1997:. *Turbulence in fluids*, volume 40 of *Fluid mechanics and its application*. Kluwer Academic Publishers, 3rd edition.
- LOMTEV, I. AND KARNIADAKIS, G., 1999:. A discontinuous Galerkin method for the Navier-Stokes equations. *Int. J. for Num. Methods in Fluids*, 29 :587–603.
- LYNCH, D. R. AND GRAY, W. G., 1979:. A wave equation model for finite element tidal computations. *Comput. Fluids*, 7 :201–228.
- LYNCH, D. R. AND WERNER, F. E., 1987:. 3-D hydrodynamics on finite elements. Part I: linearized harmonic model. *Int. J. for Num. Methods in Fluids*, 7 :871–909.

- LYNCH, D. AND WERNER, F., 1991:. 3-D hydrodynamics in finite elements. Part II: Non-linear time-stepping model. *Int. J. for Num. Methods in Fluids*, 12 :507–533.
- LYNESS, J. N. AND JESPERSEN, D., 1975:. Moderate degree symmetric quadrature rules for the triangle. *J. Inst. Math. Applies.*, 15 :19–32.
- MA, H., 1993:. A spectral element basin model for the shallow water equations. *J. Comput. Physics*, 109 :133–149.
- MADEC, G., CHARTIER, M., DELECLUSE, P., AND CREPON, M., 1991:. A three-dimensional study of deep-water formation in the northwestern mediterranean sea. *J. Phys. Oceanogr.*, 21 :1349–1371.
- MAVRIPLIS, C., 1994:. Adaptive mesh strategies for the spectral element method. *Comp. meth. in appl. mech. and eng.*, 116 :77–86.
- MUNK, W. H., 1950:. On the wind-driven ocean circulation. *J. Meteor.*, 7 :79–93.
- MYERS, P. G. AND WEAVER, A. J., 1995:. A diagnostic barotropic finite-element ocean circulation model. *J. Atmos. Ocean Tech.*, 12 :511–526.
- PATERA, A., 1984:. A spectral element method for fluid dynamics: laminar flow in channel expansion. *J. Comput. Physics*, 54 :468–488.
- PEDLOSKY, J., 1987:. *Geophysical FLuid Dynamics*. Springer-Verlag. 2nd edition.
- PEDLOSKY, J., 1996:. *Ocean Circulation theory*. Springer-Verlag.
- PERAIRE, J., ZIENKIEWICZ, O. C., AND MORGAN, K., 1986:. Shallow water problems: a general explicit formulation. *Int. J. for Num. Methods in Eng.*, 22 :547–574.
- PHILLIPS, N. A., 1957:. A coordinate system having some special advantages for numerical forecasting. *J. Meteor.*, 14 :184–185.
- PIERRE, R., 1988:. Simple C^0 approximations for the computation of incompressible flows. *Computer methods in applied mechanics and engineering*, 68 :205–227.
- POLZIN, K. L., TOOLE, J. M., LEDWELL, J. R., AND SCHMITT, R. W., 1997:. Spatial variability of turbulent mixing in the abyssal ocean. *Science*, 276 :93–95.
- PRIESTLEY, A., 1992:. The Taylor-Galerkin method for the shallow-water equations on the sphere. *Monthly Weather Review*, 120 :3003–3015.
- PRIMEAU, F. W., 1998:. Multiple equilibria of a double-gyre ocean model with super-slip boundary conditions. *J. Phys. Oceanogr.*, 28 :2130–2147.
- RAMP, S. R., MCCLEAN, J. L., COLLINS, C. A., AND SEMTNER, A. J., 1997:. Observations and modeling of the 1991–1992 El Niño signal off central California. *J. Geophys. Res.*, 102 :5553–5582.
- RITCHIE, H. AND TANGUAY, M., 1996:. A comparison of spatially averaged Eulerian and semi-Lagrangian treatments of mountains. *Monthly Weather Review*, 124 :167–181.
- ROBERT, A., 1981:. A stable numerical integration scheme for the primitive meteorological equations. *Amos. Ocean*, 19 :35–46.
- ROBERTS, M. J., MARSH, R., NEW, A. L., AND WOOD, R. A., 1996:. An intercomparison of a Bryan-Cox-type ocean model and an isopycnic ocean model. Part I: The subpolar gyre and high latitude processes. *J. Phys. Oceanogr.*, 26 :1495–1527.
- ROBERTS, M. J. AND WOOD, R. A., 1997:. Topographic sensitivity studies with a bryan-cox type ocean model. *J. Phys. Oceanogr.*, 27 :823–836.
- RONQUIST, E. M., 1980:. *Optimal spectral element methods for the unsteady three-dimensional incompressible Navier-Stokes equations*. Phd thesis, Massachusetts Institute of Technology.
- SADOURNY, R., 1975:. The dynamics of finite difference models of the shallow water equations. *J. Atmos. Sci.*, 32 :680–689.
- SALMON, R. AND TALLEY, L. D., 1989:. Generalization of Arakawa's Jacobian. *J. Comput. Physics*, 83 :247–259.

- SANDERSON, B., 1998:. Order and resolution for computational ocean dynamics. *J. Phys. Oceanogr.*, 28 :1271–1286.
- SCHOPF, P. S. AND SUAREZ, M. J., 1988:. Vacillations in a coupled ocean-atmosphere model. *J. Atmos. Sci.*, 45 :549–566.
- SCHWAB, D. J. AND BELETSKY, D., 1998:. Propagation of Kelvin waves along irregular coastlines in finite-difference models. *Advances in Water Resources*, 22 :239–235.
- SCOTT, R. B. AND STRAUB, D. N., 1998:. Small viscosity behaviour of a homogeneous, quasi-geostrophic, ocean circulation model. *J. Mar. Res.*, 56 :1225–1258.
- SHCHEPETKIN, A. F. AND O'BRIEN, J., 1996:. A physically consistent formulation of lateral friction in shallow-water equation ocean models. *Monthly Weather Review*, 124 :1285–1300.
- SHERMET, V. A., IERLEY, G. R., AND KAMENKOVICH, V. M., 1997:. Eigenanalysis of the two-dimensional wind-driven ocean circulation problem. *J. Mar. Res.*, 55 :57–92.
- SHERWIN, S. AND KARNIADAKIS, G., 1996:. Tetrahedral hp finite elements: Algorithms and flow simulations. *J. Comput. Physics*, 124 :14–45.
- SOARES, J., WAINER, I., AND WELLS, N., 1999:. Reflection of equatorial Kelvin waves at eastern ocean boundaries, part I: hypothetical boundaries. *Ann. Geophysicae*, 17 :812–826.
- SONG, Y. AND HAIDVOGEL, D. B., 1994:. A semi-implicit ocean circulation model using a generalized topography-following coordinate system. *J. Comput. Physics*, 115 :228–244.
- STAMMER, D., 1997:. Global characteristics of ocean variability estimated from regional Topex/Poseidon altimeter measurements. *J. Phys. Oceanogr.*, 27 :1743–1769.
- STANFORTH, A. AND CÔTÉ, J., 1991:. Semi-Lagrangian integration schemes for atmospheric models — a review. *Monthly Weather Review*, 119 :2206–2223.
- STOMMEL, H., 1948:. The westward intensification of wind-driven ocean currents. *Trans. Amer. Geophys. Union*, 29 :202–206.
- STRAUB, D. N., 1999:. Comments on quasigeostrophic boundary layers for barotropic ocean circulation models. In *12th Conference on Atmospheric and Oceanic Fluid Dynamics*. American Meteorological Society.
- SVERDRUP, H. U., 1947:. Wind-driven currents in a baroclinic ocean; with application to the equatorial currents of the eastern pacific. In *Proc. Natl. Acad. Sci.*, volume 33, pages 318–326.
- TREGUIER, A. M., 1992:. Kinetic energy analysis of an eddy resolving, primitive equation model of the north atlantic. *J. Geophys. Res.*, 97 :687–701.
- TROCHU, F., 1993:. A contouring program based on dual kriging interpolation. *Engineering with Computers*, 9 :160–177.
- VERONIS, G., 1966:. Wind-driven ocean circulation—part 2. numerical solution of the nonlinear problem. *Deep-sea Res.*, 13 :31–55.
- WADLEY, M. AND BIGG, G. R., 1999:. Implementation of variable time stepping in an ocean general circulation model. *Ocean Modelling*, 1 :71–80.
- WALTERS, R. A. AND CHENG, R. T., 1979:. A two-dimensional hydrodynamic model of a tidal estuary. *Adv. Water Resour.*, 2 :177–184.
- WINTON, M., 1997:. The damping effect of bottom topography on internal decadal-scale oscillations of the thermohaline circulation. *J. Phys. Oceanogr.*, 27 :203–208.
- WINTON, M., HALLBERG, R., AND GNANADESIKAN, A., 1998:. Simulation of density-driven frictional downslope flow in z-coordinate ocean models. *J. Phys. Oceanogr.*, 27 :2163–2174.
- ZHU, J. AND ZIENKIEWICZ, O., 1990:. Superconvergence recovery technique and a-posteriori error estimators. *Int. J. Numer. Meth. Eng.*, 30 :1321–1339.

ZIENKIEWICZ, O. C. AND TAYLOR, R. L.,
1991: *The finite element method*, volume 2. McGraw Hill. 4th edition.